

**NATURAL AND SYNTHETIC DOMAIN WALL INDUCED
SPIN TRIPLET CORRELATIONS IN
SUPERCONDUCTING MULTILAYERS AND
JOSEPHSON JUNCTIONS**

By
EKTA BHATIA
PHYS11201404003

National Institute of Science Education and Research, Bhubaneswar

A thesis submitted to the
Board of Studies in Physical Sciences
In partial fulfillment of requirements
for the Degree of
DOCTOR OF PHILOSOPHY
of
HOMI BHABHA NATIONAL INSTITUTE



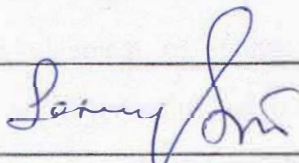
August, 2019

Homi Bhabha National Institute

Recommendations of the Viva Voce Committee

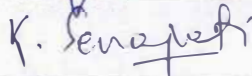
As members of the Viva Voce Committee, we certify that we have read the dissertation prepared by Ekta Bhatia entitled "Natural and synthetic domain wall induced spin triplet correlations in superconducting multilayers and Josephson junctions" and recommend that it may be accepted as fulfilling the thesis requirement for the award of Degree of Doctor of Philosophy.

Chairman - Dr. Sanjay Swain



Date: 11/03/2020

Guide / Convener - Dr. Kartik Senapati



Date: 11/03/2020

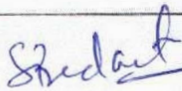
Co-guide -

Examiner - Prof. S. Ramakrishnan



Date: 11-03-2020

Member 1 - Dr. Subhankar Bedanta



Date: 11/03/2020

Member 2 - Dr. Pratap K Sahoo



Date: 11/03/2020

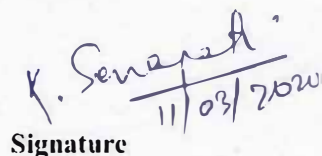
Date:

Final approval and acceptance of this thesis is contingent upon the candidate's submission of the final copies of the thesis to HBNI.

I/We hereby certify that I/we have read this thesis prepared under my/our direction and recommend that it may be accepted as fulfilling the thesis requirement.

Date: 11/03/2020

Place: Jatni



Signature

Guide

Natural and Synthetic domain wall induced spin triplet correlations in superconducting multilayers and Josephson junctions

Abstract: The past decades have witnessed an extraordinary progress in understanding the interplay between superconductivity and ferromagnetism in superconductor/ferromagnet hybrid devices. Starting in 2001 with the first realization of ferromagnetic Josephson π -junctions [1] and the almost simultaneous prediction of triplet correlations in ferromagnetic films [2], superconductivity and ferromagnetism are no longer considered as competing phenomena but rather as sources of emergent states and new effects when combined. Unlike the spin singlet Cooper pairs, the spin triplet Cooper pairs are much less affected by the exchange field of a ferromagnet and, therefore, can traverse a long distance inside a ferromagnet. Theoretically it has been shown that the basic protocol for spin-singlet to spin-triplet supercurrent conversion is the presence of magnetic non-collinearity at the superconductor-ferromagnet interface. Therefore, almost all experiments in this direction have utilized artificial magnetic non-collinearity formed by combination of several ferromagnetic layers next to the superconducting layer [3].

We have attempted to utilize the natural magnetic non-collinearity found in ferromagnets in the form of domain walls, for spin-singlet to spin-triplet conversion in a Nb-Ni-Nb planar junction geometry. This possibility was explored via unconventional features in domain wall magneto-resistance in large micron scale Nb-Ni-Nb structures and also in direct current measurements in nano-scale Nb-Ni-Nb junctions and nano-squids.

Control over the generation and tuning of triplet supercurrents is another challenge of superconducting-spintronics [3]. In this context, the combination of a soft and a hard ferromagnetic layer, functioning as an exchange-spring (XS), offers the possibility of tuning the singlet-triplet conversion process via a small external magnetic field (few mT). We detect supercurrents through Py with a thickness exceeding 10 nm, which is much larger than the singlet pair coherence length (1.4 nm), suggesting the propagation of triplet supercurrents in junctions with symmetric and asymmetric Co/Py exchange-spring interfaces. Furthermore, we demonstrate tunability of the supercurrents as a function of magnetic field orientation and therefore versus magnetic structure of Co/Py.

[1] V. V. Ryazanov *et. al.*, *Phys. Rev. Lett.* 86, 2427 (2001).

[2] F. S. Bergeret *et. al.*, *Phys. Rev. Lett.* 86, 4096 (2001); *Rev. Mod. Phys.* 77, 1321 (2005).

[3] J. Linder and J. W. A. Robinson, *Nature Physics* 11, 307 (2015).

Contents

SUMMARY	xiii
LIST OF FIGURES	xv
LIST OF ABBREVIATIONS	xxviii
1 Introduction	1
1.1 Background	1
1.2 Motivation	3
1.3 Superconductivity and superconducting devices	5
1.3.1 Allowed Cooper-pair symmetries	6
1.3.2 Josephson Junction	7
1.3.3 DC-SQUID	10
1.4 Ferromagnetism	12
1.4.1 Formation of magnetic domains	13
1.4.2 Domain walls	15
1.4.3 Micro-magnetic OOMMF simulations	16
1.5 Superconducting Proximity Effects	18
1.5.1 Superconductor(S)/Normal metal(N) Proximity Effects	18
1.5.2 Superconductor(S)/Ferromagnet(F) Proximity Effects	19
1.5.3 Long-range proximity effects	22
1.5.3.1 Bloch sphere representation of triplet generation mech- anism	23
1.5.3.2 Ways to induce LRTC in S / F hybrid Systems	25

1.6	Previous studies of long-range triplet supercurrents	28
1.7	Theme of the thesis	34
1.8	Organization of the thesis	35
2	Magnetization reversal in ferromagnetic film and ensuing effects on proximal superconducting films	38
2.1	Introduction	38
2.2	Experimental details	40
2.2.1	Sample Preparation	40
2.2.1.1	Thin film growth	40
2.2.1.2	Optical-lithography	41
2.2.1.3	Electron Beam lithography	42
2.2.2	Domain imaging using Kerr microscope	43
2.2.2.1	MOKE measurement geometries	44
2.2.2.2	Kerr-microscope set-up	45
2.2.2.3	Hysteresis cycles from magneto-optical images	46
2.2.3	Transport and magnetization measurements	47
2.3	Results and discussion	47
2.3.1	Shape anisotropy driven domain reversal in Néel and Bloch DW regimes of Ni	47
2.3.2	Effect of domain wall stray field on superconducting transition temperature in Ni/Nb bilayer	53
2.4	Conclusion	57
3	Unconventional domain wall magnetoresistance of Nb-Ni-Nb planar structures below superconducting transition temperature of Nb	58
3.1	Introduction	58
3.2	Experimental Details	60
3.2.1	Sample fabrication	60

3.2.2	Transport measurements	60
3.2.3	Justification of sample geometry	61
3.3	Results and Discussions	65
3.3.1	DWMR of Ni/Nb stripes above superconducting transition	65
3.3.2	DWMR of Ni/Nb stripes below superconducting transition	66
3.4	Conclusion	71
4	Intrinsic domain wall induced triplet supercurrents in Nb/Ni/Nb planar Josephson junction and DC-SQUID	72
4.1	Introduction	72
4.2	Experimental Details:	73
4.2.1	Film Growth.	73
4.2.2	Device Fabrication.	74
4.2.3	Micro-magnetic OOMMF simulations.	75
4.2.4	Transport measurements.	76
4.3	Results and Discussion	77
4.3.1	Nb/Ni/Nb planar Josephson junction characteristics	77
4.3.2	Domain wall junction based DC-SQUID characteristics	80
4.4	Conclusion	83
5	External field tunable superconducting transition temperature in Nb/Co/Py/Nb superconductor/exchange spring/superconductor films	84
5.1	Introduction	84
5.2	Experimental details	87
5.3	Results and Discussion	87
5.3.1	Charaterization of Co/Py spring system	87
5.3.2	Variation of T_c with magnetic configuration of Co/Py	89
5.3.3	Reversible tuning of T_c in spring range	94
5.4	Conclusion	96

6	Triplet supercurrents in Josephson junctions with symmetric and asymmetric exchange-spring barrier	97
6.1	Introduction	97
6.2	Experimental details:	99
6.2.1	Film Growth.	99
6.2.2	Device Fabrication.	99
6.2.3	Transport and magnetization measurements.	100
6.3	Results and Discussion	101
6.3.1	Magnetic characterization of Co/Py exchange-spring system . . .	101
6.3.2	Asymmetric exchange-spring junction characteristics	103
6.3.2.1	Magnetization configuration dependent critical current .	104
6.3.3	Double (symmetric) exchange-spring junction characteristics. . . .	107
6.4	Conclusion	112
7	Summary and Future Scope	114
7.1	Summary	114
7.1.1	Triplet correlations using natural domain walls	114
7.1.2	Triplet correlations using synthetic domain walls	116
7.2	Future Scope	119
	Bibliography	121

List of Figures

1.1	Four symmetry classifications of Cooper-pair, following the Pauli's exclusion principle. The overall pairing symmetry is decided by three independent components: spin, frequency and momentum.	7
1.2	Schematic illustration of a Josephson junction, where two superconductors are separated by a barrier, which may be an insulator or a normal metal or a ferromagnet. The wave functions of two superconductors overlap in the barrier region.	8
1.3	(a) Typical $I - V$ characteristic of a Josephson junction, where the arrow denotes the critical current I_c , at which the junction switches into voltage state. (b) Characteristic Fraunhofer modulations of a Josephson junction showing the modulations of normalized critical current with external magnetic flux Φ , normalized with flux quantum Φ_0	9
1.4	Schematic illustration of a DC-SQUID	10
1.5	Typical $I - V$ characteristic of a DC-SQUID at two different magnetic fields, the trace on the right represents the modulations of voltage versus external magnetic flux Φ , normalized with flux quantum Φ_0 . The period of modulations is equal to one flux quantum Φ_0	11
1.6	Schematic illustration of 4s and 3d bands of an itinerant ferromagnet close to Fermi level (adapted from Ref. [30]).	12
1.7	Schematic illustration showing the formation of multiple domains in order to reduce the magnetostatic energy in a ferromagnet.	14

1.8	(a) Schematic illustration of Precession (pink) and damping (blue) of magnetization vector M under an effective magnetic field H_{eff} , (b) Schematic of the 3D magnetic sample for micro-magnetic simulations, the sample is divided into 3D discrete cells. Based on the cell size, the sample is divided into different planes shown in the figure. Each cell can be assigned with a magnetization vector m represented by the arrow. The orientation of the arrow is decided by the direction and magnitude of external magnetic field.	16
1.9	Schematic illustration of proximity effect at the interface of superconductor and normal metal.	19
1.10	(a) Schematic illustration showing the momentum gained by the Cooper-pair, when entering a ferromagnet at the S/F interface. In a ferromagnet, the spin up and spin down bands are split by $2E_{ex}$ at the Fermi surface ε_F due to exchange-interaction. When a Cooper-pair enters a ferromagnet, it acquires a finite momentum ($k_{F\uparrow} \neq -k_{F\downarrow}$), (b) Schematic illustration showing singlet (red)-triplet (blue) mixing at the S/F interface. The singlet and triplet correlations with $S_z = 0$ decay exponentially over $\xi_F \sim 1-5$ nm in the ferromagnet [39,41]. The reflections from F layer cause spin-dependent phase shifts on the other side of the interface, forming a singlet-triplet mixture in S.	20
1.11	(a) Schematic illustration showing the mechanism of singlet-triplet Cooper-pair conversion at an S/F interface. The misaligned moments at the S/F interface and F' layer rotates the $S_z=0$ triplet component in spin space and converts them to $S_z=\pm 1$ triplet component [50,52,53], (b) Schematic showing the spin-mixing and spin-rotation process at the S/F and F/F' interfaces [52]	22

1.12 (a) Schematic illustration showing the S/F/F' trilayer, where the magnetization M and M' are misaligned relative to each other, (b) Bloch sphere representation of spin-rotation process at F/F' interface. The magnetization (M) of F layer is along the z direction while the direction of magnetization (M') of F' layer is at an angle (α, ϕ) in the Bloch sphere.	24
1.13 Schematic of the device geometry proposed for generating long-range triplet supercurrents by spin-injection [67].	27
1.14 Schematic of the device geometry used for generating long-range triplet supercurrents in Ref [9].	31
1.15 (a) Schematic of the device geometry used for generating long-range triplet supercurrents in Ref [10] (b) Schematic of the multilayer structure (F) used between the two Nb electrodes shown in Fig. 1.15(a).	33
2.1 Schematic illustration of (a) a Bloch domain wall with spins rotating perpendicular and (b) a Néel domain wall with spins rotating in the plane of domain walls. The region shown between the two outer planes is a magnetic domain wall, which exists at the boundary of two magnetic domains.	39
2.2 Thickness dependence of domain wall energy of Bloch and Néel domain walls [92].	40
2.3 Steps followed during the patterning of Ni stripe.	41
2.4 Steps followed during the patterning of Ni/Nb stripe.	42
2.5 Schematic of MOKE showing the formation of elliptically polarized light from the incident linearly polarized light [94]. The incident linearly polarized light converts into elliptically polarized light after being reflected from the magnetized sample. The polarization axis is rotated by an angle θ_K , known as Kerr-rotation.	44

2.6	Schematic illustration showing different geometries of MOKE, (a) Longitudinal mode (b) Transverse mode, and (c) Polar mode. The incident and reflected light are in the same plane, which is marked as the plane of incidence.	45
2.7	Finding magnetic domains using Kerr microscope set up [38], Red and blue color regions in the sample represent magnetic domains oriented in opposite directions.	46
2.8	FESEM micrograph of the Ni stripes with aspect ratios (ratio of length to width of a segment) varying from 2 to 19.	48
2.9	(a) $M(H)$ loop for segment R_3 of Ni stripe shown in Fig. 2.8 in parallel configuration at 300 K for Ni(15 nm) using Kerr microscope, (b), (c), (d), and (e) are the Kerr micro-graphs for points marked A, B, C, D in (a), Black arrows in (b) and (g) gives the direction of external magnetic field, (f) represents the $M(H)$ loop for segment R_3 of Ni stripe shown in Fig. 2.8 in transverse configuration at 300 K, (g), (h), (i), and (j) are the Kerr micro-graphs for point marked A, B, C, and D in (f). The scale bar shown in (b) is valid for all the images (b), (c), (d), and (e) and the scale bar shown in (g) is valid for all the images (g), (h), (i), and (j), respectively.	49
2.10	(a) $M(H)$ loop for segment R_1 of Ni stripe shown in Fig. 2.8(a) in parallel configuration at 300 K for Ni(90 nm) using Kerr microscope, (b), (c) are the Kerr micro-graphs for points marked A, B in (a); Black arrows in (b) and (e) denotes the direction of external magnetic field, (d) represents the $M(H)$ loop for segment R_3 of Ni stripe shown in Fig. 2.8(a) in transverse configuration at 300 K, (e) is the Kerr micro-graph for point marked A in (f); The scale bar shown in (b) is valid for all the images.	50

2.11 (a), (b) represents the coercive field (H_c) vs width (w) variation for parallel configuration (magnetic field (H) along the length) for Ni(15 nm) and Ni(90 nm). Red curves represents the fits to the data points shown in blue color. (c), (d) represents the coercive field (H_c) vs width (w) variation for transverse configuration (magnetic field (H) along the width) for Ni(15 nm) and Ni(90 nm).	52
2.12 Schematic illustration showing an Ni/Nb bilayer stripe in four-probe geometry. An overlying Nb layer would directly sense the out-of-plane stray field of DWs of the Ni.	53
2.13 $T_c(H)$ curve for Ni(40nm)/Nb(55nm) bilayer stripe (Red points; left hand axis). An in-plane applied magnetic field is swept in backward and forward directions. The corresponding $M(H)$ loop (blue points; right hand axis) is at $T = 10$ K. Minima in low field $T_c(H)$ matches closely with the H_c of Ni.	54
2.14 (a) Normalized $R(T)$ curves at field values near H_c (-300 Oe) and near saturation (1572 Oe, -1572 Oe) for Ni(100 nm)/Nb(55 nm) stripes. (b) $T_c(H)$ phase diagrams for Ni(x nm)/Nb(55 nm) stripes for $x = 20$ nm, 40 nm, 80 nm, and 100 nm.	55
2.15 (a) $T_c(H)$ phase diagram of Ni(40 nm)/Nb(55 nm) stripes (blue points; left hand axis) and stray field (H_s) calculation for stripes from $M(H)$ loop measured at 10 K (pink points; right hand axis). The dashed horizontal line is drawn through the minimum T_c near H_c , giving an estimate of DW stray field (H_{s0}) from $T_c(H)$ phase diagram, (b) H_{s0} is plotted with maximum suppression in T_c obtained from $T_c(H)$ phase diagrams of panel b for Ni(x)/Nb(55 nm) stripes, where $x = 20$ nm, 40 nm, 80 nm, 100 nm.	56
3.1 Steps followed during the fabrication of a Nb/Ni/Nb planar structure. .	61

3.2	(a) Schematic illustration of Nb/Ni/Nb planar structure in four-probe geometry. The gap between two Nb electrodes is $\sim 3 \mu\text{m}$, (b) Cross-sectional view of the region near the gap, a Bloch domain wall exists at the interface of two magnetic domains represented by red and blue color (oriented oppositely), the schematic of a Bloch domain wall at the bottom emphasize the magnetic non-collinearity needed for singlet-triplet conversion.	62
3.3	$R(T)$ curve for a Ni/Nb bilayer stripe (without any gap in Nb layer) at zero magnetic field. Inset shows the schematic of the top view of the sample. Superconducting transition temperature, $T_c = 8.5 \text{ K}$	62
3.4	$R(T)$ curves for Nb/Ni/Nb planar structure at three separations (d_1, d_2, d_3) between voltage contacts but fixed distance between the current contacts, the resistance is higher for larger separation (d_1) indicating the diffusion of Cooper-pairs from Nb to Ni beyond the gap region, Inset shows the schematic illustration of the top view of the sample in a four-probe geometry. Another inset shows the T_c for all the three cases, which was 8.5 K	63
3.5	DWMR of Nb/Ni/Nb planar structures at $T > T_c$, (a) $R(H)$ curves for parallel field configuration, showing the intrinsic MR of Ni, (b) $R(H)$ curves for transverse field configuration, showing DWMR peaks along with intrinsic MR of Ni. DWMR remains the same for temperatures above T_c , (c) Longitudnal Kerr micrograph for parallel configuration, showing the propagation of a domain wall, (d) Longitudnal Kerr micrograph for transverse configuration, showing multiple DWs during magnetization reversal. Kerr micographs are recorded at room temperature. Red color and blue color represent domains oriented in opposite direction.	64

3.6	DWMR of Nb/Ni/Nb planar structures at $T < T_c$. (a) The $R(H)$ curves at 8K follows the $M(H)$ loop of Ni film. $T = 8K$ is very close to $T_c = 8.3$ K and therefore, sensitive to DW stray fields. (b) The $R(H)$ curves at 7K indicates that superconductivity of Nb is no more affected by the stray fields of DWs.	66
3.7	(a) The $R(H)$ curves at 6K for field sweep direction from positive to negative saturation field, showing a decrease in resistance at positive field. (b) The $R(H)$ curves at 6K for field sweep direction from negative to positive saturation field, showing a decrease in resistance at negative field.	67
3.8	Schematic parallel resistance model. The total current I flows in parallel through Nb (I_{Nb}) and Ni (I_{Ni}) for $T > T_c$. For $T < T_c$, $R_{Nb} = 0$ and the total resistance becomes an addition of (i) magnetic domain resistance R_D , (ii) DW resistance R_{DW} , (iii) Ni/Nb Interface resistance R_{Int} , and (iv) Resistance of Ni present in gap region R_g	69
3.9	Current dependent DWMR for temperature above and below T_c . (a) $R(H)$ curves at 10 K for different bias currents showing DWMR remains the same for all bias currents. (b) $R(H)$ curves at 6 K for different bias currents showing DWMR decreases with increasing bias currents. Inset shows the difference of DWMR peak amplitude for particular bias current w.r.t. that at $100 \mu A$, defined as ΔR_{6K} and ΔR_{10K} for 6K and 10K.	69
4.1	Steps followed during the fabrication of a Nb/Ni/Nb planar Josephson junction.	74

4.2	(a) Schematic illustration of Josephson junction showing triangular notch in the central stripe with 6 μm width. (b) FESEM image showing the top view of the junction. A gap of dimension $70 \times 85 \text{ nm}^2$ was carved in the Nb layer over the notch area. (c) Energy Dispersive Spectroscopy (EDS) image showing the absence of Nb in the gap region, Green color represents the presence of Nb. (d) False color FESEM image showing the cross-sectional view of the junction. The depth of the cut is beyond the Nb layer, confirming the absence of Nb in the gap.	75
4.3	(a) micro-magnetic 3D OOMMF simulation image at remanence state for an in-plane applied magnetic field. Red and blue color represents moments oriented in opposite directions, white color represents a domain wall which separates two magnetic domains represented by red and blue color. (b) micro-magnetic simulation image at remanence state for out-of-plane magnetic field configuration. A domain wall is pinned at the notch area.	76
4.4	<i>I-V</i> characteristics at $H = 0 \text{ Oe}$, 50 Oe , 100 Oe , 150 Oe and $T = 2 \text{ K}$ for out-of-plane field configuration.	77
4.5	Magnetic field dependence of I_c of Nb/Ni/Nb Josephson junction at 2 K for out-of-plane magnetic fields. The inset shows the hysteresis of low field $I_c(H)$ due to internal barrier flux of Ni.	78

- 4.6 $R(T)$ curves at bias current of $10 \mu\text{A}$ for unconditioned and conditioned state. The unconditioned state corresponds to the demagnetized state with random domain structures represented by the black arrows in inset(i). The conditioned state shown in inset (ii) corresponds to remanence, where two oppositely oriented domains are present around the notch and a well defined domain wall is present inside the notch, following the OOMMF simulations of Fig. 4.3(b). Inset (iii) presents the $R(T)$ curve at lower temperature on a logarithmic scale for a clear comparison of the two situations. 79
- 4.7 (a) Schematic illustration of Josephson junction SQUID showing two triangular notches in the central stripe. (b) FESEM image showing the top view of the DC-SQUID. A gap of dimension $70 \times 85 \text{ nm}^2$ was carved in the Nb layer over the two notches. (c) Zoomed view of a single notch showing the Nb electrodes and Ni present in the gap region. 81
- 4.8 (a) micro-magnetic 3D OOMMF simulation image for an out-of-plane magnetic field configuration shows two domain walls at remanence state at the two notches in a Ni loop, remanence state is achieved by saturating the sample first to 400 mT and then reducing the field to zero. Red and blue color represent magnetic moments oriented in opposite directions, white color represents a domain wall which separates two magnetic domains represented by red and blue color. (b) I - V characteristics at $H = 0 \text{ Oe}$ and $T = 2 \text{ K}$ for in plane and out-of-plane field configuration. The $H = 0 \text{ Oe}$ state is achieved by saturating the sample at 400 mT and then sweeping it to zero at 10 K. (c) Flux dependent voltage modulations of Nb/Ni/Nb SQUID for three different bias currents of $300 \mu\text{A}$, $250 \mu\text{A}$, and $150 \mu\text{A}$, marked as A, B and C in (b). The period of oscillation is 3.2 Oe . . 82

5.1	Schematic hysteresis loops of (a) Rigid hard/soft bilayer, (b) exchange-spring bilayer, the minor loops are irreversible in case of rigid hard/soft bilayer, while these loops are reversible in case of exchange-spring in a certain field range, known as spring-range. H_N denoted the nucleation field and H_{ex} denotes the exchange-field.	85
5.2	$M(H)$ loops (major and minor) at 300 K for Nb(55 nm)/Co(30 nm)/Py(30 nm)/Nb(55 nm) multilayer. Magnetic field is applied in the plane of the films.	88
5.3	Schematic showing Nb/Co/Py/Nb multilayer in which Co/Py is an XS (a non-collinear structure of magnetic moments is expected for a specific field sequence).	89
5.4	Magnetization vs temperature measurements for a Nb(55 nm)/Co(30 nm)/Py(30 nm)/Nb(55 nm) multilayer at different in-plane fields of 25 Oe, 20 Oe, 15 Oe, 10 Oe, 5 Oe and 0 Oe.	89
5.5	T_c as a function of an in-plane field H is represented by red points on the right axis and dM/dH is represented by blue points on the left axis for a Nb(55 nm)/Co(30 nm)/Py(30 nm)/Nb(55 nm) multilayer.	90
5.6	Representative $M(T)$ curves corresponding to the points A and B of Fig. 5.5 from which T_c was estimated.	91
5.7	Magnetization vs temperature measurements for a Nb (60 nm) thin film under different magnetic history	91
5.8	Comparison of $T_c(H)$ (extracted from $M(T)$ measurements) curves for Nb/Co(30 nm)/Py(30 nm)/Nb (blue points), Nb/Co(30 nm)/Py(75 nm)/Nb (red points) and Nb/Co(30 nm)/Py(30 nm)/Nb (pink points) multilayers.	92

5.9	<p>$T_c(H)$ curve for Nb(55 nm)/Co(30 nm)/Py(45 nm)/Nb(55 nm) is represented by red points on the right axis and the $M(H)$ loop of the same stack at 10 K is represented by blue points on the left axis). The square $M(H)$ loop indicates that the magnetic configuration is collinear.</p>	94
5.10	<p>(a) $M(T)$ curves for Nb(55 nm)/Co(30 nm)/Py(90 nm)/Nb(55 nm) multilayer, measured at $H_{meas} = 11$ Oe for different returning fields H_{ret} lying inside and outside the spring range. (b) $M(H)$ loop of Nb(55 nm)/Co(30 nm)/Py(90 nm)/Nb(55 nm) multilayer at 10 K, the returning fields for paths a, b, c, d, e shown in (a) are marked as A, B, C, D, and E.</p>	95
6.1	<p>(a) FESEM image showing the pattern of the sample defining the contact pads for the Nb/Co/Py/Nb nano-pillar devices. (b) FESEM micrograph showing the zoomed view of track over which the devices were made using Ga-ion based FIB, (c) the FESEM image showing perspective view of a nano-pillar Josephson junction, (d) the FIB image showing the corss sectional view of a nano-pillar Josephson junction. .</p>	100
6.2	<p>(a) Major and minor magnetic hysteresis loops of an unpatterned Nb/Co(2 nm)/Py(11 nm)/Nb multilayer at 10 K in an in-plane magnetic field. For a range of magnetic fields the minor loops are reversible, which is the hallmark of exchange-spring behavior. (b) The field derivative curve of an unpatterned Nb/Co(2 nm)/Py(11 nm)/Nb multilayer at 10 K. (c) Schematic illustration of a nano-pillar Josephson junction with an XS barrier, the non-collinear magnetic structure is created following a specific field sequence.</p>	102

6.3	(a) I - V curves for different in-plane magnetic fields of 0 mT, 15 mT, 30 mT, 45 mT, 60 mT, 80 mT and 300 mT for a Nb/Co(2 nm)/Py(7 nm)/Nb device with dimensions of $(300 \times 350) \text{ nm}^2$ at 4.2 K. (b) dV/dI versus I curves for different in-plane magnetic fields of 0 mT, 15 mT, 30 mT, 45 mT, 60 mT, 80 mT and 300 mT for the same device.	103
6.4	(a) The Fraunhofer modulation of I_c with an in-plane applied magnetic field for a Nb/Co(2 nm)/Py(7 nm)/Nb XS Josephson junction at 4.2 K for a device dimension of $300 \times 350 \text{ nm}^2$. (b) Low field regime of Fraunhofer modulation showing hysteresis.	104
6.5	(a) Schematic illustration of direction of bias current I and applied magnetic field $\mu_0 H$ (b) Resistance vs direction of applied magnetic field showing manipulation of triplet supercurrents for Nb/Co(2 nm)/Py(11 nm)/Nb Josephson junction with dimensions of $(\sim(300 \times 300) \text{ nm}^2)$ at 1.6 K and for field values of 0 mT, 20 mT and 400 mT. Here, theta denotes the angle of the direction of applied magnetic field with respect to the length of the track (x-axis).	105
6.6	Comparison of $I_c(H)$ and $R(H)$ curves for Nb/Co(2 nm)/Py(7 nm)/Nb Josephson junction. Red points on left hand axis represent the $R(H)$ curve while blue points on right axis represent the $I_c(H)$. The minima in $I_c(H)$ and the maxima in $R(H)$ lie at same magnetic field, signifying the equivalence of both measurements.	106
6.7	(a) I - V curves for different in-plane magnetic fields for a double exchange-spring Nb/Py(7 nm)/Co(2 nm)/Py(7 nm)/Nb Josephson junction with dimensions of $(300 \times 300) \text{ nm}^2$ at 1.6 K. (b) dV/dI versus I curves for different in-plane magnetic fields for the same device. . .	107

6.8	(a) Fraunhofer modulations of $I_c(H)$ for a double exchange-spring Nb/Py(7 nm)/Co(2 nm)/Py(7 nm)/Nb Josephson junction with dimensions ($\sim 300 \times 300$ nm ²) at 1.6 K. (b) Critical current vs direction of applied magnetic field showing manipulation of triplet supercurrents at 1.6 K and a field value of 20 mT; Here, theta denotes the angle of applied magnetic field with respect to the length of the track.	108
6.9	(a) Comparison of I - V curves of a Nb/Co(2 nm)/Py(7 nm)/Nb junction with a Nb/Py(6 nm)/Nb junction at a temperature of 4.2 K and zero field. (b) Comparison of I - V curves of a Nb/Co(2 nm)/Py(11 nm)/Nb junction with a Nb/Co(2 nm)/Cu(4 nm)/Py(11 nm)/Nb junction at a temperature of 4.2 K and zero field.	109
6.10	Comparison of $R(H)$ curves for Nb/Co(2 nm)/Py(7 nm)/Nb and Nb/Py(6 nm)/Nb Josephson junctions at 4.2 K. Fraunhofer type modulations were observed in junction resistance as a function of magnetic field for the Nb/Co(2 nm)/Py(7 nm)/Nb while no field dependence was observed for Nb/Py(6 nm)/Nb junction.	110
6.11	Variation of $I_c R_N$ product with Py thickness for all devices; the green curve presents the $I_c R_N$ for Py-only junction (taken from Ref. [42]). As d_{Py} increases above 5 nm, $I_c R_N$ is almost zero in these junctions, whereas on introducing an additional Co layer, the $I_c R_N$ product is enhanced and decays very slowly. Inset shows the $I_c R_N$ product for double spring Nb/Py/Co/Py/Nb junction with total thickness of the Py layer.	111
7.1	Pictorial summary of thesis.	118

Chapter 7

Summary and Future Scope

7.1 Summary

A summary of the important results of this thesis is presented in this concluding chapter. Generation and control of triplet correlations in superconductor(S)/ferromagnet(F) multilayers and S/F/S Josephson junctions using natural and synthetic domain walls (exchange-spring) have been the focus of this thesis. Generation of triplet correlations in Nb/Ni/Nb planar structures and triplet supercurrents in Nb/Ni/Nb Josephson junctions and SQUIDs have been demonstrated using natural domain walls. Tuning of Nb T_c in Nb/Co/Py/Nb multilayer and tuning of triplet supercurrents in Nb/Co/Py/Nb and Nb/Py/Co/Py/Nb nanopillar Josephson junctions have been demonstrated using exchange-spring (synthetic domain walls). Following a brief summary of the results, we conclude this chapter by identifying a few potential frontiers of further research on triplet supercurrents in S/F/S Josephson junctions.

7.1.1 Triplet correlations using natural domain walls

We have utilized the natural magnetic non-collinearity found in ferromagnets in the form of domain wall, for singlet-triplet conversion in Nb/Ni/Nb planar structures and Josephson junctions. Prior to these studies, we characterized the domain wall

configuration of Ni stripes using Kerr microscopy and studied the effect of these domain walls on an overlying Nb layer by plotting the $T_c(H)$ phase diagrams (in chapter 2). We found a suppression in T_c near coercive fields, where the effect of domain walls becomes maximum. In chapter 3, we utilized this stripe geometry to study singlet-triplet conversion through natural domain walls of Ni. For this purpose, a microscopic gap was carved in the Nb layer in a patterned Ni/Nb bilayer stripe. It is well known [85,106] that when a current passes through a ferromagnetic domain wall, it causes spin accumulation at the domain walls giving rise to domain wall magneto-resistance (DWMR). DWMR appears as an additional component in the MR curves, usually visible in constricted geometry. By carving a gap in the Nb layer, we were able to inject singlet Cooper pairs of Nb into the domain walls of Ni present underneath. We utilized DWMR as a tool to study the effect of this Cooper pair injection into domain walls. We compared DWMR at temperatures above and below the T_c of Nb in a Nb/Ni/Nb planar structure. Conventional DWMR peaks were observed at the coercive field for temperatures above T_c . Due to the presence of a gap in the Nb layer, we were able to measure the DWMR at temperatures below T_c . We observed an unconventional drop in DWMR near H_c for temperatures below T_c . We interpreted this unconventional drop in DWMR in terms of singlet-triplet conversion through the intrinsic domain walls of Ni. This observation was, however, an indirect evidence of singlet-triplet conversion via domain walls. We have extended this study further in chapter 4, looking for a direct signature.

In chapter 4, we used a constricted geometry to pin a single domain wall of Ni at the barrier of a focused ion beam (FIB) based Nb/Ni/Nb planar Josephson junction. A gap of width ~ 70 nm was carved using FIB in the Nb layer over the constriction in a Ni/Nb bilayer stripe. Micromagnetic 3D OOMMF simulations showed that a domain wall remains pinned at the notch for most part of the hysteresis loop. From the transport measurements, we found a supercurrent in these planar junctions. The long-range nature of the supercurrent was apparent from the

fact that supercurrent existed over a magnetic (Ni) barrier width of ~ 70 nm, which is much greater than the singlet pair coherence length (~ 4 nm) of Ni. We have also demonstrated a triplet SQUID using the same technique by putting two planar junctions in a superconductor loop. Characteristic voltage modulations were observed as a function of the magnetic flux, confirming a functional SQUID device. Therefore, we are able to fabricate a triplet Josephson junction SQUID through intrinsic domain walls for the first time.

7.1.2 Triplet correlations using synthetic domain walls

Control and tuning of triplet supercurrents is a major goal of superconducting-spintronics. In this context, an exchange-spring (XS) bilayer (a hard/soft ferromagnets combination), a reversible synthetic domain wall, can offer tuning of triplet supercurrents with small magnetic fields (few mT). We have explored this possibility by studying the $T_c(H)$ curves in S/XS/S multilayers and magnetic field angle dependent triplet supercurrents in S/XS/S magnetic Josephson junctions.

In chapter 5, we studied singlet-triplet conversion effects in S/XS/S multilayers by using diamagnetic screening currents as a probing tool. Nb/Co/Py/Nb multilayers were subjected to a static magnetic field in the plane of the multilayers to induce screening currents. In the $T_c(H)$ curve, we observed a relative enhancement in T_c in the spring range of the magnetic field, following an initial decrease due to the stray field effects. In the XS range, a magnetically non-collinear structure gets established in the Co/Py XS. Therefore, the recovery of T_c in spring samples was interpreted in terms of singlet-triplet conversion through the magnetic non-collinear structure of XS. We excluded the possibility of stray field cancellation as the possible reason for the observed recovery of T_c in these samples. We also demonstrated a tunable T_c with a reversible shift of ~ 400 mK in the spring range of magnetic fields. This reflects a reversible singlet-triplet conversion process due to the reversible nature of XS.

In Chapter 6, we used an XS (a reversible synthetic domain-wall) barrier to fabricate nano-pillar Josephson junctions to control triplet supercurrents. We fabricated FIB based Josephson junctions using Co/Py (XS) and Py/Co/Py (double XS) magnetic barriers. We observed Josephson coupling for Py layer thickness (11 nm) far exceeding the singlet-pair coherence length (~ 1.5 nm) of Py, confirming the existence of triplet supercurrents in these junctions. Magnetic-field-orientation-dependent control of spin-triplet supercurrents in a junction is demonstrated for the first time in this work. Triplet supercurrents were observed in Josephson junctions with both asymmetric (Co/Py) and symmetric (Py/Co/Py) XS interfaces, which was previously believed to be possible only with symmetric barriers. The complete summary of thesis is shown in Fig. 7.1.

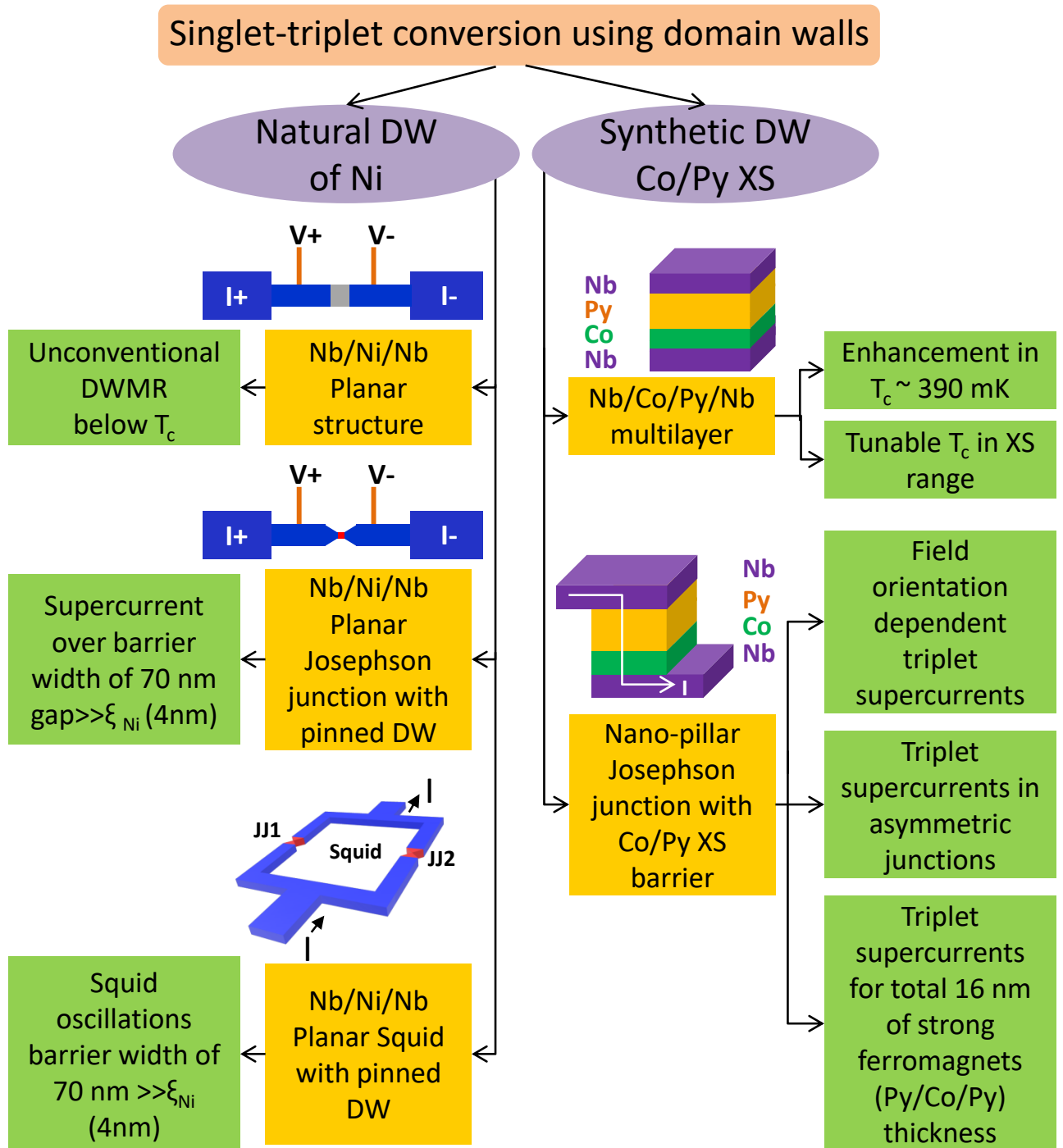


Figure 7.1: Pictorial summary of thesis.

7.2 Future Scope

In this thesis, we have been able to explore only a few aspects of the triplet supercurrents in S/F multilayers and S/F/S Josephson junctions. The work presented in this thesis is a small advance towards the generation and control of spin-triplet correlations in S/F multilayers and S/F/S Josephson junctions and may motivate many new experiments in the field of superconducting-spintronics.

There are certain aspects that can be looked at, in order to achieve more control over the generation and tuning of triplet supercurrents, following the work presented in this thesis:

- In chapter 4 of this thesis, we utilized a pinned Bloch domain wall to generate triplet supercurrents in Nb/Ni/Nb planar Josephson junctions. The natural extension of this work is to utilize Néel and Cross-tie domain walls to generate triplet supercurrents in S/F/S planar junctions. In this way, the influence of the structure of magnetic non-collinearity can be studied, which may be useful in superconducting spintronics.
- S/F/S planar junctions can be made with ferromagnets different from Ni, for example, Co and Py with spin diffusion length higher (~ 60 nm for Co) and lower (~ 5 nm for Py) than Ni (~ 20 nm). By doing so, one can investigate whether the decay length of triplet Cooper-pairs is limited by the spin-diffusion length of F or not, which is still an open question in front of researchers.
- In a planar S/F/S Josephson junction, spin-waves can be excited in the ferromagnet and the non-collinear spin structure of spin-wave can be exploited to couple the two superconducting electrodes by triplet supercurrents.
- Following chapter 3, a systematic study of DWMR for temperatures below T_c can be performed to investigate the singlet-triplet conversion process, in S/F/S planar structures.

- It has been predicted theoretically that a spin-triplet Josephson coupling can be established in S/F'/F/S Josephson junctions through a double Andreev reflection process, in which the current-phase relationship is dominated by a second harmonic term. In the Nb/Co/Py/Nb Josephson junction showed in chapter 6, one can study the Shapiro steps in I - V curves by irradiating the junction with microwave frequency to test this hypothesis.
- Other spring combinations with higher spin-diffusion length of soft and hard ferromagnetic materials can be used to make S/XS/S Josephson junction to obtain even higher range of triplet supercurrents.
- The range of triplet supercurrents in normal metals is unknown till date. This can be investigated by fabricating and characterizing Nb/Py/Co/Cu/Co/Py/Nb Josephson junctions. The range of triplet supercurrents in Cu can be obtained by varying the thickness of Cu to the point when supercurrent becomes zero.

SUMMARY

Superconductivity and ferromagnetism are two antagonistic phenomena which, when integrated into a single device, lead to some interesting effects at the S/F interface. Essentially, Cooper pairs leak into the ferromagnetic side by acquiring a net momentum directly proportional to the magnetic exchange energy. This effect is known as proximity effect. The spin singlet Cooper pairs from the superconductor layer penetrate only a few nanometers into the ferromagnet (F) layer due to the strong exchange field of ferromagnet. This is usually known as short-range proximity effect. A similar effect, known as long-range spin-triplet proximity effect, was predicted in 2001, and observed in hybrid systems having non-collinear magnetization at the S/F interface. In such systems, the spin-singlet Cooper-pair converts to spin-polarized spin-triplet Cooper-pair on passing through the non-collinear magnetization of F at an S/F interface. These triplet Cooper pairs can travel up to hundreds of nm in F. This long range nature is an immediately attractive feature for applications in the field of superconducting-spintronics. In this direction, almost all experiments have utilized artificial magnetic non-collinearity formed by the combination of several ferromagnetic layers next to the superconducting layer. In the first part of this thesis, we have attempted to utilize the natural magnetic non-collinearity found in ferromagnets in the form of domain walls, for singlet-triplet conversion in Nb/Ni/Nb planar structures and Josephson junctions. Prior to the studies of triplet correlations in S/F hybrid systems, we studied the magnetic domain configurations during the magnetization reversal of a single Ni stripe. We found that the density of domain walls in a stripe geometry strongly depends on the magnetic field orientation, irrespective of the thickness of the Ni layer. We also quantified the effect of ferromagnetic domain reversal on an overlying superconductor. We found that, in a stripe geometry the transition temperature of a superconducting Nb layer follows the magnetic hysteresis loop of the underlying Ni layer, approaching a minimum near the coercive field, at all thicknesses. Next, we utilized this stripe geometry to study singlet-triplet

conversion through the natural domain walls of Ni. By carving a microscopic gap in the Nb layer in a patterned Ni/Nb bilayer stripe, we were able to inject the singlet Cooper pairs of Nb into the domain walls of Ni present underneath. We observed an unconventional drop in domain-wall magneto-resistance for temperatures below T_c , which was interpreted in terms of singlet-triplet conversion through the intrinsic domain walls of Ni. Following this observation, we used a notched geometry to pin a single domain wall of Ni at the barrier in focused ion beam (FIB) patterned Nb/Ni/Nb planar Josephson junctions. We observed Josephson coupling in the junction, which existed for magnetic barrier width (~ 70 nm), much greater than the singlet pair coherence length (~ 4 nm) of Ni, confirming the long range triplet nature of supercurrents in this junction. We further fabricated DC-SQUID devices using the same concept of pinning a domain wall in a planar Nb/Ni/Nb junction. These devices showed characteristic flux modulations of voltage at a fixed bias current for magnetic barrier width of ~ 70 nm. In the second part of the thesis, we have used Co/Py exchange spring (XS) for generation and external manipulation of spin triplet correlations in Nb/Co/Py/Nb multilayers and Josephson junctions. We have investigated changes in the superconducting transition temperature (T_c) of the S/XS/S multilayer via magnetization measurements. We found a recovery of T_c (over a suppression in T_c due to domain wall stray field) by ~ 400 mK in the non-collinear range of XS samples, which was interpreted in terms of singlet-triplet conversion through the non-collinear structure of Co/Py XS. We also observed a reversible tuning of T_c in the spring range of magnetic fields, demonstrating external field tunability of superconductivity. Further, we fabricated nano-pillar Josephson junctions with symmetric and asymmetric Co/Py XS barriers using focused ion beam patterning. In these devices we demonstrated control over triplet supercurrents as a function of the direction of constant applied magnetic field. Another key observation of this experiment was that, unlike earlier belief, both symmetric and asymmetric magnetic Josephson junctions can be used for spin-triplet generation and manipulation.

Chapter 1

Introduction

1.1 Background

Ever since the discovery of superconductivity, the interplay between this macroscopic quantum state and ferromagnetism has intrigued researchers equally on theoretical and experimental fronts. The microscopic origin of these two states is very contrasting. Superconductivity is realized due to the condensation of electrons into Cooper-pairs below the superconducting transition temperature (T_c) through phonon mediated attractive interaction. Electrons with opposite spins and momentum pair up into a ground state with energy below the single electron ground state, termed as Cooper-pair [1]. The pair of electrons then move in a correlated manner compensating for the scattering loss of each other, giving rise to loss-less conduction. The Cooper-pair with zero spin tends to oppose any external magnetic field up to a strength equal to the pairing energy. This accounts for the diamagnetic behavior of a superconductor, also termed as Meissner effect. On the other hand, Ferromagnetism arises due to electron spins aligned in the same direction by exchange interaction. Therefore, the coexistence of superconductivity and ferromagnetism can be mapped into a competition between the pair condensation energy (2Δ), and the Zeeman energy ($\mu_B E_{ex}$) [2]. The former tries to align the spins anti-parallel to each other

while the latter favors parallel alignment. This basic difference between the spin states of charge carriers is the prime reason behind the antagonism of the two states. However, the technological prospect associated with the mutual accommodation of the two macroscopic orders makes it a very interesting field of research.

The extreme antagonism poses several fundamental questions in systems (both homogeneous and hybrid), where the coexistence of superconductivity and ferromagnetism has been found. Indeed, superconductivity and ferromagnetism are now considered as sources of emergent states and unique effects, when combined. Although rare, some unconventional superconductors exist, with naturally coexisting superconducting and ferromagnetic order. Some of the examples include UGe_2 [3], UCoGe [4] and URhGe [5]. The coexistence of superconductivity and ferromagnetism can also be realized synthetically using conventional ferromagnets (F) and conventional superconductors (S) to form S/F hybrids. At the heart of all the interesting phenomena is the fact that on passing through an S/F interface, the up-spin and down-spin electrons of the Cooper-pair acquire a phase lag due to the exchange-energy of F. Consequently, the Cooper-pairs form an inhomogeneous superconducting state, so-called FFLO state in the ferromagnet [6,7]. The spin-singlet and the spin-triplet components with zero spin projection of the Cooper-pair coexist with each other in this state [6,7]. The mixed state of singlet and triplet components brings in new physical phenomena. However, this inhomogeneous state can survive only up to a few nm in the ferromagnet, which is not a very useful range from the application point of view.

Naturally, the next question in front of researchers was to know whether it is possible to generate long-range equal-spin triplet Cooper-pairs at an S/F interface. In the search of long-range effects, in 2001, Bergeret *et al.* [8] predicted the generation of long-range triplet correlations at magnetically inhomogeneous S/F interfaces, which was demonstrated experimentally by Keizer *et al.* [9] in 2006. As discussed earlier, the Cooper-pair converts into a mixture of singlet and triplet components on passing

through an S/F interface. Although the singlet component is rotationally invariant, the triplet component is rotationally variant and can be rotated in the spin-space to convert to an equal spin-triplet Cooper-pair by creating a magnetic inhomogeneity at the S/F interface. The equal-spin triplet Cooper-pair is not affected by the Zeeman energy and hence, can travel up to long distances in the ferromagnet. However, one of the limiting factors for the decay length of triplet Cooper-pairs is the spin-diffusion length [10–12], which is the characteristic length scale over which the electron preserves its spin. The spin diffusion length is a material-specific parameter, which may vary from ~ 5 nm in Py [13] to $\sim \mu\text{m}$ in CrO_2 due to its half-metallic nature [14].

Another interesting fact about these equal-spin triplet Cooper-pairs is that they are “odd” in frequency, which essentially means that the electrons forming the pair can not occupy the same state at the same time. This type of pairing is very unique and insensitive to any external impurities or disorder. On the other hand, the naturally existing ferromagnetic superconductors are p-wave in nature and “even” in frequency. The p-wave pairing is very sensitive to any external impurities or disorder and hence, is short-range in nature. This is why the S/F systems become interesting from both fundamental and application perspective. The S/F systems give an opportunity to realize the spin-polarized supercurrents, which is the core requirement for the field of superconducting-spintronics.

1.2 Motivation

The past two decades have witnessed remarkable progress in the understanding of the interplay between superconductivity and ferromagnetism in S/F hybrid devices. In 2006, Keizer *et al.* gave the first demonstration of triplet supercurrents in CrO_2 [9]. This discovery undoubtedly showed that equal-spin triplet Cooper-pairs could travel up to hundreds of nm through a half-metal, CrO_2 in a lateral S/F/S Josephson

junction. Later, in 2007, Houzet and Buzdin [15] proposed that in a S/F'/F'/S Josephson junction, the misalignment between F and F' layers can be used to generate triplet Cooper-pair at first S/F/F' interface. These triplet Cooper-pairs can travel a long distance in F layer. At F/F'/S interfaces, the triplet Cooper-pair will convert back to the singlet Cooper-pair due to a misalignment between F' and F layers. In this way, triplet supercurrents can be generated in a controlled manner in magnetic Josephson junctions. In the past, a series of experiments were performed using this device geometry with the aim to generate and control triplet supercurrents in magnetic Josephson junctions. [10–12,16,17].

This thesis attempts to study the mechanism of generation and control of triplet correlations in S/F multilayers and Josephson junctions to address the following questions: Is it possible to generate triplet supercurrents by exploiting the intrinsic magnetic non-collinearity of domain walls of ferromagnets? Can we make a spin-triplet SQUID using intrinsic domain walls? Can we tune triplet supercurrents by using a tunable magnetic non-collinear structure of an exchange-spring? Can we generate triplet supercurrents for the magnetic barrier width longer than the spin-diffusion length in a planar magnetic Josephson junction? Can we generate triplet supercurrents in asymmetric magnetic Josephson junctions?

In this chapter, we outline the current status of experimental and theoretical understanding of the generation and control of triplet supercurrents in S/F multilayers and S/F/S Josephson junctions. We start with a brief discussion of the theoretical aspects of superconductivity, superconducting devices, ferromagnetism and proximity effects, followed by a survey of the experimental results on triplet supercurrents in S/F hybrids and S/F/S Josephson junctions. In the end, we describe the theme and layout of the thesis.

1.3 Superconductivity and superconducting devices

In 1911, Heike Kamerlingh-Onnes discovered that some materials lose their electrical resistance below a certain temperature, known as transition temperature, T_c [18]. This effect is known as superconductivity. The two defining properties of the superconducting materials are perfect conductivity and ideal diamagnetic behavior, known as Meissner effect [19, 20]. In order to explain this phenomenon, a microscopic theory, known as BCS theory, was developed by John Bardeen, Leon N. Cooper and John R. Schrieffer in 1957 [1]. According to the BCS theory, the interaction of conduction electrons with phonons results in an effective attraction between electrons, giving rise to the Cooper pairs - a pair of two electrons with opposite spins and momentum. These Cooper pairs are bosonic in nature and condense into a common ground state for temperatures below T_c . Therefore, a single order parameter, $\psi(r)$ (also known as the wave function of Cooper pair) is enough to describe the macroscopic quantum phenomenon of superconductivity [1].

$$\psi(r) = \sqrt{n^{CP}} e^{i\phi}$$

Here, the amplitude of the Cooper pair wave function is proportional to the Cooper pair density n^{CP} and the phase ϕ of Cooper pair. The BCS theory explains the conventional, s-wave superconductivity where the Cooper pairs are in a spin-singlet state described as

$$|0, 0\rangle = \frac{1}{\sqrt{2}}(|\uparrow\downarrow\rangle - |\downarrow\uparrow\rangle)$$

This is to be noted that the work described in this thesis utilizes s-wave superconductors throughout. Therefore, the other types of superconductors are beyond the scope of this thesis.

1.3.1 Allowed Cooper-pair symmetries

A Cooper pair consists of two electrons with opposite spin and momentum. The electrons forming the Cooper pair are fermions and therefore, they follow the Pauli-exclusion principle. According to this principle, two fermions can not have the same quantum numbers. Therefore, two electrons forming the Cooper-pair can only be paired if their combined wave function is anti-symmetric.

$$\psi(r_1 - r_2 : s_1, s_2 : t_1 - t_2) = -\psi(r_2 - r_1 : s_2, s_1 : t_2 - t_1)$$

There are three different ways in which this condition can be satisfied. One way is that if the electrons forming the pair have opposite spins. This is the case in conventional s-wave superconductors and d-wave superconductors. Moreover, the Cooper-pair wave function consists of two more components other than the electron spin, which are spatial and temporal components. These components are commonly represented in terms of momentum and frequency. Thus, Pauli's criterion can also be satisfied if any of these two components is antisymmetric in nature for the electrons forming the pair. In that case, the spin part of the Cooper-pair wave function can be symmetric in nature and the net spin can be ± 1 for these Cooper-pairs, known as spin-triplet Cooper pairs. Spin-triplet Cooper pairs can be divided into two categories; (i) Pairs having odd momentum but even frequency; (ii) Pairs having even momentum but odd frequency. There are only a few superconductors found in nature with odd momentum and even frequency [21]. These are known as triplet superconductors. The superconducting condensate in these superconductors is very sensitive to any kind of disorder or impurity scattering. Therefore, the pairing is not long-range in nature and they are not very useful from the application perspective. However, recently they have been demonstrated to generate spin currents without any dissipation in spin-valve devices [22,23]. Still, there are practical problems to overcome for using ferromagnetic superconductors, for example, very low critical temperatures (mK) and high pressures required during the measurement. Triplet

superconductor/ferromagnet bilayer structure was first demonstrated by Anwar *et al.* recently [23]. This may be the initial step towards investigating the bulk triplet superconductors/ferromagnets interfaces.

Spin	Frequency	Momentum	Overall	Type
Singlet (odd)	Even	Even	Odd	A
- - - -	Odd	Odd	Odd	B
- - - -	Even	Odd	Odd	C
Triplet (even)	Odd	Even	Odd	D
- - + -				

Figure 1.1: Four symmetry classifications of Cooper-pair, following the Pauli's exclusion principle. The overall pairing symmetry is decided by three independent components: spin, frequency and momentum.

The second category belongs to odd-frequency spin-triplet Cooper-pairs, which have been generated in carefully engineered S/F hybrid structures. These Cooper pairs have even momentum and therefore, are resistant to any kind of impurity scattering. The resilience to scattering makes these pairs long-range in nature. Therefore, they have various applications in superconducting-spintronics, superconducting electronics and, quantum computing. This makes triplet supercurrents especially interesting and is the main subject of this thesis. Based on this classification, Eschrig *et al.* [51] have divided it into four categories: Type A, B, C and D, as shown in Fig. 1.1.

1.3.2 Josephson Junction

Two superconducting electrodes joined through a thin barrier, either an insulator (I) or a normal metal (N) or a ferromagnet (F), forms a Josephson junction. The Josephson effect was originally realized for an S/I/S junction, which is a manifestation of macroscopic quantum behavior. The effect was first proposed by Josephson in

1962 [24], according to which, a Cooper pair tunnels from one side of the insulating barrier to the other. In this process, the two superconducting electrodes are coupled through the insulating barrier and the current through the junction is proportional to the phase difference between the two superconductors [24,25]. Therefore, the overlap between the macroscopic wave functions of two superconductors, when separated by a weak link, is known as the Josephson effect, as shown in the schematic of Fig. 1.2.

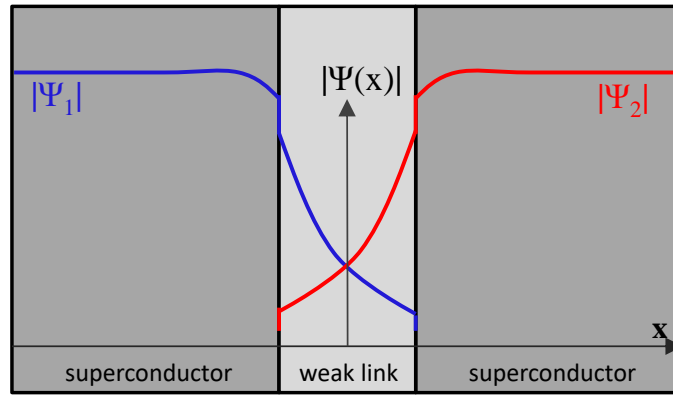


Figure 1.2: Schematic illustration of a Josephson junction, where two superconductors are separated by a barrier, which may be an insulator or a normal metal or a ferromagnet. The wave functions of two superconductors overlap in the barrier region.

The first Josephson relation [24] is:

$$j_s = j_c \sin \varphi$$

where j_c is the critical current density of the junction, and φ is the phase difference between the two electrodes. The free energy E_J of the Josephson junction, also known as Josephson energy is written as [26]:

$$E_J(\varphi) = \frac{\Phi_0}{2\pi} A \int_0^\varphi j_c \sin(\varphi) d\varphi = \frac{\Phi_0}{2\pi} I_c (1 - \cos \varphi)$$

Here, I_c is the critical current, given by, $I_c = j_c \cdot A$, where A is the junction area. The Josephson energy becomes maximum, when the phase difference between two superconductors is $\pi/2$ and is minimum for $\varphi = 0$. The Josephson junction switches into the voltage state for applied currents $I > I_c$. The time variation of the phase difference φ leads to the second Josephson relation:

$$\frac{\partial\varphi}{\partial t} = \frac{2e}{\hbar}V = \frac{2\pi}{\Phi_0}V$$

Conversely, for a constant voltage V across the junction, the phase difference can be written as $\varphi = \varphi_0 + \omega_J t$, where

$$\omega_J = \frac{2\pi}{\Phi_0}V = \frac{2e}{\hbar}V \quad \text{with} \quad \frac{1}{\Phi_0} = 483.6 \frac{\text{MHz}}{\mu\text{V}}$$

Using the first Josephson relation:

$$j_s = j_c \sin(\omega_J t + \varphi_0)$$

The time average of the phase evolution across the junction can be studied by measuring the DC voltage across the junction and using the second Josephson relation as:

$$\langle V \rangle = \left\langle \frac{\partial\varphi}{\partial t} \right\rangle \frac{\Phi_0}{2\pi}$$

Therefore, the current through the junction oscillates with Josephson frequency ω_J , which is proportional to the applied voltage.

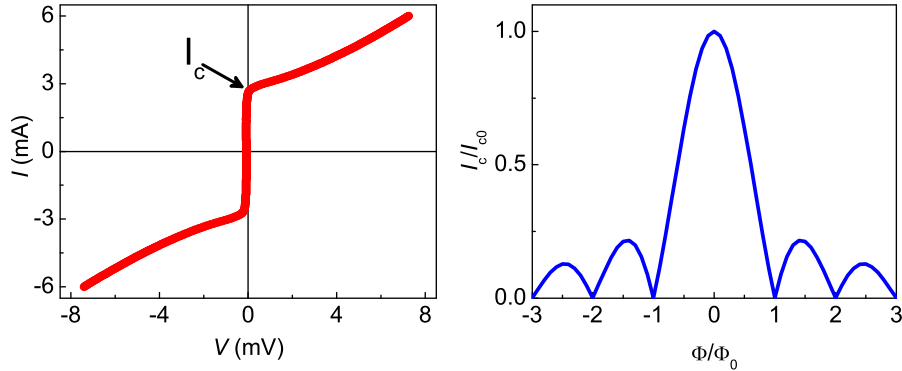


Figure 1.3: (a) Typical $I - V$ characteristic of a Josephson junction, where the arrow denotes the critical current I_c , at which the junction switches into voltage state. (b) Characteristic Fraunhofer modulations of a Josephson junction showing the modulations of normalized critical current with external magnetic flux Φ , normalized with flux quantum Φ_0 .

A typical $I - V$ curve of a current-biased Josephson junction is shown in Fig. 1.3(a). The junction critical current is marked in the figure as I_c . The fact that the current through a Josephson junction is dependent on the phase difference

between the electrodes becomes apparent in the magnetic field dependence of junction critical current. Changing magnetic flux through the junction is a convenient way to manipulate the phase difference across the junction. It has been shown that for magnetic flux corresponding to one flux quantum (Φ_0), phase changes by 2π . I_c as a function of φ , therefore follows the relation [26]:

$$I_c(\varphi) = I_c \left| \frac{\sin \pi \frac{\Phi}{\Phi_0}}{\pi \frac{\Phi}{\Phi_0}} \right|$$

where Φ is the flux through the junction. The corresponding curve, shown in Fig. 1.3(b) is a characteristic feature of Josephson junction.

1.3.3 DC-SQUID

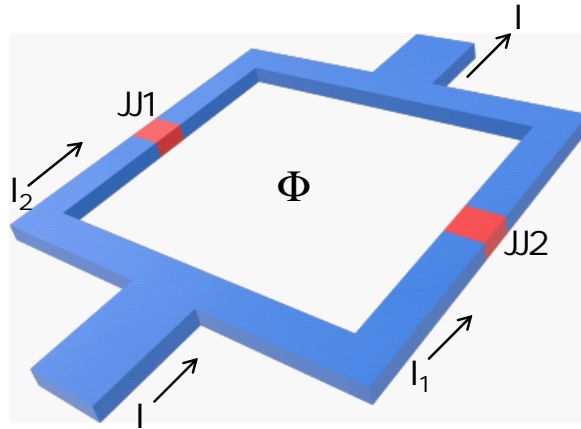


Figure 1.4: Schematic illustration of a DC-SQUID

When two Josephson junctions are connected in parallel through a superconducting loop, they form a DC-SQUID [27,28] (Superconducting Quantum Interference Device), as shown in Fig. 1.4. In a superconductor loop, the total flux is quantized in units of $h/2e$. Therefore, if we apply an external magnetic field, a current will be induced in the loop such that the total flux through the loop is an integral multiple of one flux quantum ($\Phi_0 = h/2e$). The total phase difference around the loop can only be an integral multiple of 2π , which can be written as:

$$2\pi \frac{\Phi}{\Phi_0} + \varphi_1 - \varphi_2 = 2\pi n$$

where φ_1 and φ_2 are phase shifts across the two junctions, Φ is the external magnetic flux and n is an integer. A bias current I splits into two parts I_1 and I_2 , through the two junctions:

$$I = I_1 + I_2 = I_{c1}\sin\varphi_1 + I_{c2}\sin\varphi_2$$

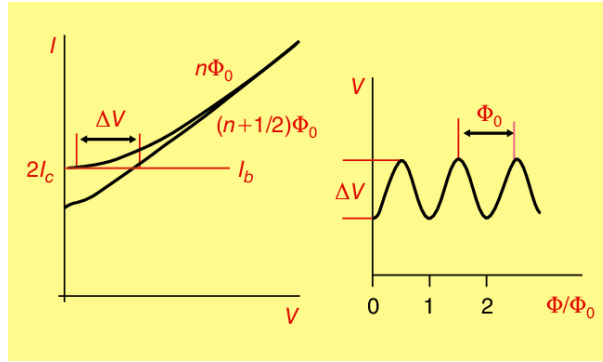


Figure 1.5: Typical $I - V$ characteristic of a DC-SQUID at two different magnetic fields, the trace on the right represents the modulations of voltage versus external magnetic flux Φ , normalized with flux quantum Φ_0 . The period of modulations is equal to one flux quantum Φ_0 .

For a symmetric DC-SQUID with identical junctions, $I_{c1} = I_{c2} = I_c$. For an external magnetic flux Φ_{ext} , the critical current through the individual junction modulates and the critical current through the SQUID is the result of interference between the currents of individual junctions:

$$I = 2I_c \left| \cos \frac{\pi\Phi}{\Phi_0} \right|$$

If we send a bias current I_B through the SQUID, a voltage V is generated across the SQUID, which modulates periodically as a function of an external magnetic field with a period equal to one flux quantum Φ_0 [28], as shown in Fig. 1.5. This curve is a characteristic feature of a DC-SQUID. Therefore, it is also known as flux to voltage converter. It is possible to measure very tiny changes in magnetic flux ($\Phi \ll \Phi_0$) if a proper selection of bias current is made such that the amplitude of the voltage modulation becomes maximum.

1.4 Ferromagnetism

A material showing spontaneous magnetization is known as a ferromagnet. Irrespective of the microscopic mechanism, macroscopic ferromagnetism is a resultant effect of the microscopic spin alignment. In this thesis, we are dealing with 3d transition metal ferromagnets such as Co, Ni and $\text{Ni}_{80}\text{Fe}_{20}$ alloy (Py). Ferromagnetism in these layers is well understood in terms of the band model [29]. In the ferromagnetic

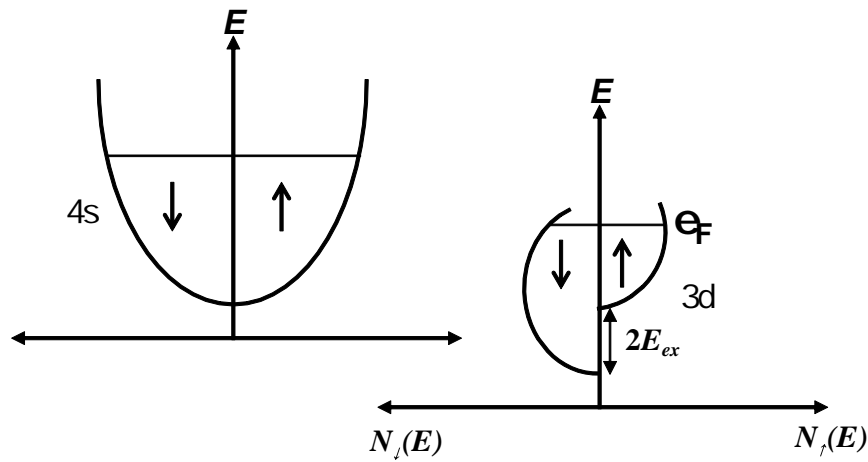


Figure 1.6: Schematic illustration of 4s and 3d bands of an itinerant ferromagnet close to Fermi level (adapted from Ref. [30]).

transition metals, the outer shell electrons belong to 4s and 3d bands, respectively. The spin-up and spin-down sub-bands of 3d are split due to the exchange-energy, E_{ex} , as shown in Fig. 1.6. This unequal distribution of electrons in the two sub-bands gives rise to a net magnetic moment in the system. The exchange interaction and hence, exchange energy is purely quantum mechanical in origin and are a result of the Pauli exclusion principle. According to this principle, electrons (fermions) must be anti-symmetric with respect to their exchange. Considering a two-particle system, with particles located at positions x_1 and x_2 with spins s_1 and s_2 , respectively,

$$\psi(x_1, s_1; x_2, s_2) = -\psi(x_2, s_2; x_1, s_1)$$

Therefore, if the space part is symmetric, they must be anti-symmetric in spin and vice-versa. In a ferromagnet, Coulomb repulsion becomes minimum for a wave function anti-symmetric in space and therefore, it should be symmetric w.r.t. the exchange of spins. The property of ferromagnetism can also be explained using Stoner criterion [31]:

$$I.\tilde{D}(E_F) > 1$$

where I is the exchange integral and $\tilde{D}(E_F) = (V/2N).D(E_F)$, here V is the volume and $D(E_F)$ is the density of states (DOS) at the Fermi level. We can relate I with E_{ex} as: $E_{ex} = I(n_{\uparrow} - n_{\downarrow})/N$. Here, n_{\uparrow} and n_{\downarrow} represents the number of electrons with up-spin and down-spin and N presents the total number of electrons, respectively.

When a magnetic sample is placed in an external magnetic field, the magnetic moments start to precess around the magnetic field and, for a certain magnetic field, all the moments are aligned in the same direction. This critical field is known as saturation field H_{sat} . The magnetization (M) becomes constant for fields applied beyond the saturation field and, is known as saturation magnetization, M_s . On reversing back the field to zero, a finite magnetization remains in the sample and, is known as remnant magnetization, M_r . The field required to make the magnetization zero is known as coercive field, H_c . Since the magnetization lags behind the applied magnetic field, the $M(H)$ curve is hysteretic and is the characteristic of a particular ferromagnetic material.

1.4.1 Formation of magnetic domains

It was first proposed by Weiss in 1907 that a ferromagnetic material is made up of small regions magnetized in different directions, known as magnetic domains [32]. Magnetic domains are formed to minimize the total free energy given as [33]:

$$E_{tot} = \underbrace{A \cdot \nabla m^2}_{\text{exchange-energy}} + \underbrace{\varepsilon_{an}}_{\text{anisotropy-energy}} + \underbrace{\frac{1}{2} \mu_0 M \cdot H_d}_{\text{magnetostatic-energy}} - \underbrace{\mu_0 M \cdot H_a}_{\text{Zeeman-energy}} - \underbrace{\sigma_{ex} \cdot \epsilon^0}_{\text{external-stress}} + \underbrace{\frac{1}{2} (p_e - \epsilon^0) \cdot \bar{c} \cdot (p_e - \epsilon^0)}_{\text{magnetostriction-energy}}$$

Here, A is the exchange-stiffness constant, m is the normalized magnetization (M/M_s), ε_{an} is the anisotropy energy, H_d is the demagnetizing field, H_a is the applied field, σ_{ex} is external stress tensor, ϵ^0 is strain and p_e is deviation from initial magnetic fields and \bar{c} is tensor of elastic constants. In the above expression, the first term corresponds to exchange interaction, which tries to align all the spins in the same direction, the second term represents magneto-crystalline anisotropy which makes certain directions energetically more favorable for the alignment of magnetic moments. The third term is due to dipole-dipole interaction which tries to align the moments in the opposite direction on a large length scale. The fourth term corresponds to the interaction of magnetic moments with an external magnetic field, commonly known as the Zeeman term. The fifth and sixth terms are due to external stress or the atomic displacement of crystal resulting in the modification of the overlap of neighboring orbitals. In conventional systems, the last two terms are usually negligible. As discussed earlier, the minimum exchange energy corresponds

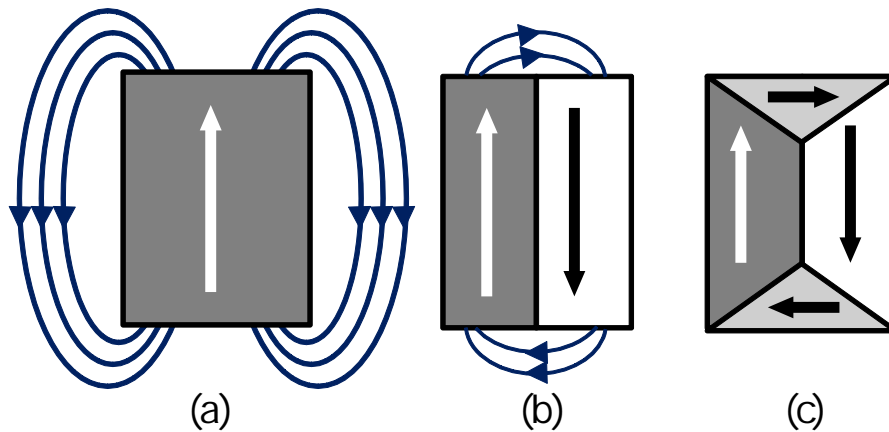


Figure 1.7: Schematic illustration showing the formation of multiple domains in order to reduce the magnetostatic energy in a ferromagnet.

to magnetic moments aligned in the same direction. However, this leads to an

increase in the magnetostatic energy of the system. The competition between these two energies results in the formation of domains, as shown in Fig. 1.7(b). Landau and Lifshitz [34] suggested that the magnetostatic energy can be reduced to zero by the formation of flux enclosure domains, as shown in Fig. 1.7(c). However, the anisotropy and exchange energies also play an important role in the formation of domains with different shapes and sizes [33].

1.4.2 Domain walls

The neighboring ferromagnetic domains are separated from each other by a region/boundary, known as the domain wall, which was first verified by Sixtus and Tonks [35]. In a domain wall, the direction of magnetization varies continuously from one domain to the neighboring one, in order to minimize the exchange energy. To understand this, we consider the exchange energy between the two magnetic moments at an angle θ as:

$$E = -2J\mathbf{S}_1 \cdot \mathbf{S}_2 = -2JS^2 \cos\theta$$

where J is exchange-integral and S is spin angular momentum. Therefore, the flipping of the magnetic moment costs an energy $= 2JS^2$ for $\theta = \pi$. However, if the same flipping is performed over N number of magnetic moments, the angle between the neighboring moments will be equal to θ/N . Therefore, the total exchange energy gets distributed over N number of spins. Taking the approximation: $\cos\theta = 1 - \theta^2/2$, the net energy cost is $JS^2 \frac{\pi^2}{N}$, which is much smaller than $2JS^2$.

$$\Delta E_{total} = JS^2 \frac{\pi^2}{N}$$

The minimization of exchange energy involves a gradual rotation of spins which will increase the width of the wall, resulting in an increase of anisotropy energy. The anisotropy energy is $E_{an} = K \sin^2\theta$, where K is the anisotropy constant and θ is the angle between two neighboring magnetic moments. Therefore, anisotropy energy

increases and exchange energy decreases with an increase in the width of the wall. The resultant width of the domain wall is decided by the competition of anisotropy and exchange energy, so as to minimize the total energy of the system [33].

1.4.3 Micro-magnetic OOMMF simulations

The magnetic configuration of any magnetic system for a particular magnetic field corresponds to the minimum free energy of the system at that field. For the simulations of spin-orientations and the hysteresis loop, we have used Object Oriented Micromagnetic Framework (OOMMF) simulations, which is an open-source software package, developed by the National Institute of Standards and Technology (NIST), USA [36]. The code solves the Landau-Lifshitz-Gilbert (LLG) equation to find the magnetic configuration of the system.

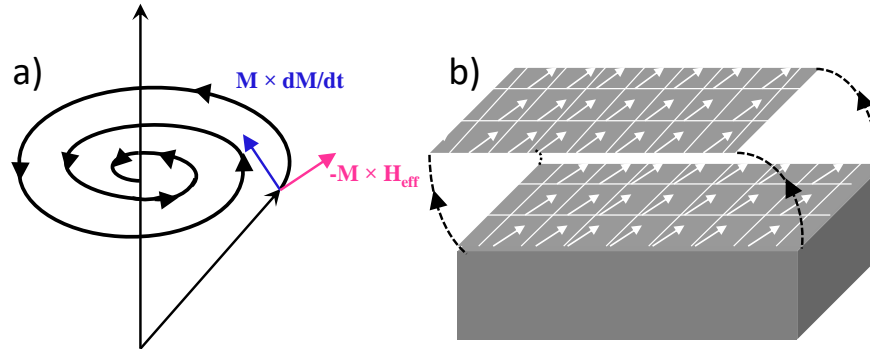


Figure 1.8: (a) Schematic illustration of Precession (pink) and damping (blue) of magnetization vector M under an effective magnetic field H_{eff} , (b) Schematic of the 3D magnetic sample for micro-magnetic simulations, the sample is divided into 3D discrete cells. Based on the cell size, the sample is divided into different planes shown in the figure. Each cell can be assigned with a magnetization vector m represented by the arrow. The orientation of the arrow is decided by the direction and magnitude of external magnetic field.

Let us consider a 3D ferromagnetic system, as shown in Fig. 1.8(b). The OOMMF simulation is a numerical method to find the magnetic configuration corresponding to the minimum energy for a particular magnetic field. It assumes that the magnetization is a spatially continuous function, $M(r)$. Therefore, the 3D

system can be divided into discrete units each having a unit magnetization vector, as shown in Fig. 1.8(b). Hence, the total energy of the system and the local effective field experienced by each segment is given by:

$$E_{tot} = - \int \mu_0 H_{eff}(r) \cdot M(r) d^3r$$

$$H_{eff}(r) = - \frac{1}{\mu_0} \nabla_M E_{tot}$$

Now, a single magnetic field is representing all the components of magnetic energy. Therefore, it is possible to achieve the dynamic magnetization of each segment by solving the Landau-Lifshitz-Gilbert (LLG) equation

$$\frac{d\vec{m}}{dt} = \gamma \mu_0 \vec{m} \times H_{eff} - \alpha \vec{m} \times \frac{d\vec{m}}{dt}$$

where \vec{m} is the normalized magnetization (= M/M_s), H_{eff} is the applied field, γ is the gyro-magnetic ratio, and α is a material-dependent damping term, also known as Gilbert damping parameter.

In the equation, the first term describes the precession of magnetization M in a local magnetic field H_{eff} , while the second term represents the loss of energy by the system due to damping parameter α , which causes the magnetic moment to align with the magnetic field, as shown in Fig. 1.8(a). In the simulation, the LLG equation is solved for each cell, in succession, for the whole system, over many iterations. This allows the magnetization of every cell to interact with neighboring cells and re-orient with time and, is then integrated using Runge-Kutta algorithms [37] to calculate the magnetization of the system. The overall magnetization of the system evolves to minimize the total energy so that the system relaxes into a minimum energy configuration of magnetic moments.

The size of the discrete unit (cell size) is a crucial parameter, since a smaller cell size may provide a more realistic picture of the given object in some cases. However, much smaller cell size may increase the computation time significantly. Typically, this value should be of the order of the exchange length of a ferromagnetic material, given by

$$l_{ex} = \sqrt{\frac{2A}{\mu_0 M_s^2}}$$

Here A is the exchange stiffness constant in units of J/m and M_s is saturation magnetization. Usually, l_{ex} can be defined as the length scale over which magnetic moments of the ferromagnetic system can change their arrangement in the presence of an exchange field. Damping constant (α) is another important parameter, which is a measure of the rate at which the magnetization aligns with the field. For OOMMF simulations, we can define the magnetic anisotropy of the particular cells such as uniaxial anisotropy for Co and cubic anisotropy for Ni. For polycrystalline films, for which each grain has random orientation, one can use a random vector field as the magneto-crystalline anisotropy to set the principal axes in each unit cell. Shape anisotropy is another important factor that corresponds to the minimization of stray fields [38]. Apart from these parameters, exchange stiffness constant A and saturation magnetization M_s are material specific input parameters for the simulation. We have used the literature values of these parameters for OOMMF simulations throughout the thesis.

1.5 Superconducting Proximity Effects

1.5.1 Superconductor(S)/Normal metal(N) Proximity Effects

When a superconductor is brought in close contact with a normal metal, some superconducting correlations leak into the normal metal up to a distance ξ_N . The leakage of Cooper pairs into adjacent normal metal is known as proximity effect [39].

As shown in the schematic of Fig. 1.9, the Cooper pair amplitude is maximum within the superconductor but it decays exponentially and ultimately, reduces to zero in the normal metal. The distance over which the amplitude of the order parameter can vary, is known as coherence length ξ_N , which is a material-specific property.

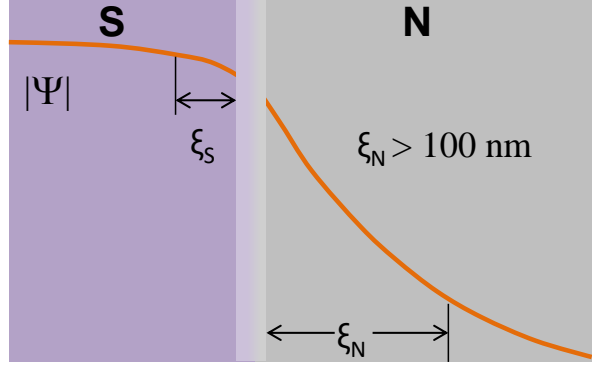


Figure 1.9: Schematic illustration of proximity effect at the interface of superconductor and normal metal.

At an S/N interface, Cooper-pairs are drained from the superconductor over a length scale given by

$$\xi_S(T) = \xi_0 (1/\sqrt{T/T_c - 1})$$

where ξ_0 is the coherence length of superconductor at 0 K. Depending on the material, The value of ξ_0 may vary from few nanometers to few microns [40]. In the diffusive metal, superconducting order parameter decays over a length scale given by [39]

$$\xi_N = \sqrt{\frac{\hbar D_N}{K_B T}}$$

where \hbar is the reduced Planck's constant, D_N is diffusion coefficient of N, k_B is the Boltzmann constant and T is the temperature. The decay length of Cooper pairs varies in the range of hundreds of nm for a transparent interface [39].

1.5.2 Superconductor(S)/Ferromagnet(F) Proximity Effects

If we replace normal metal with ferromagnet, we obtain superconductor(S)/ferromagnet(F) hybrid system. The difference between N and F is that there is exchange interaction in F, due to which the up-spin and down-spin bands are split at Fermi level by the exchange energy E_{ex} [39,41], as shown in Fig. 1.10(a). In a superconductor, the Cooper pair consists of two electrons with equal and opposite momentum ($k_F, -k_F$)

at the Fermi surface. Therefore, the total momentum of the pair is zero. When this Cooper-pair enters the ferromagnet, the up-spin electron acquires a momentum $Q/2$ whereas the down-spin electron loses a momentum $Q/2$. Therefore, the $|\uparrow\downarrow\rangle$ part acquires a finite momentum: $k_{F\uparrow} - k_{F\downarrow} = Q$ and $|\downarrow\uparrow\rangle$ acquires a momentum $k_{F\downarrow} - k_{F\uparrow} = -Q$. Then, the singlet Cooper-pair converts to a mixture of singlet and triplet Cooper-pairs with

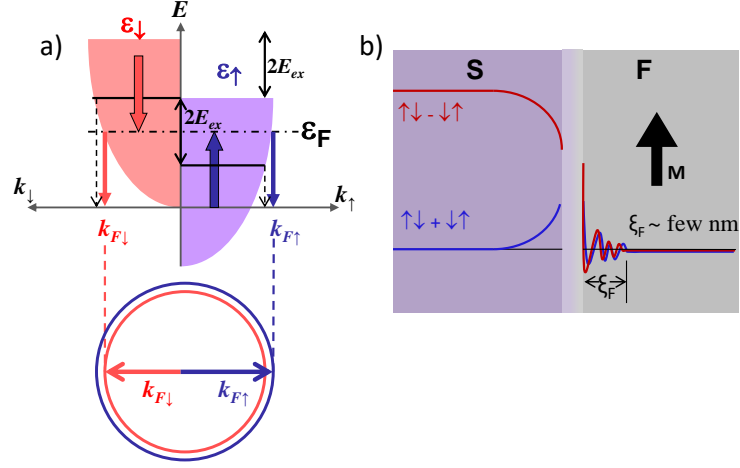


Figure 1.10: (a) Schematic illustration showing the momentum gained by the Cooper-pair, when entering a ferromagnet at the S/F interface. In a ferromagnet, the spin up and spin down bands are split by $2E_{ex}$ at the Fermi surface ε_F due to exchange-interaction. When a Cooper-pair enters a ferromagnet, it acquires a finite momentum ($k_{F\uparrow} \neq -k_{F\downarrow}$), (b) Schematic illustration showing singlet (red)-triplet (blue) mixing at the S/F interface. The singlet and triplet correlations with $S_z = 0$ decay exponentially over $\xi_F \sim 1-5$ nm in the ferromagnet [39,41]. The reflections from F layer cause spin-dependent phase shifts on the other side of the interface, forming a singlet-triplet mixture in S.

In a diffusive system, these correlations can survive over a finite length scale ξ_F , known as the coherence length and is given by [39]

$$\xi_F = \sqrt{\frac{\hbar D_F}{E_{ex}}}$$

where D_F is the diffusion coefficient and E_{ex} is the exchange energy. The decay length in a ferromagnet is governed by the exchange energy E_{ex} , unlike the case of normal metal, where it is governed by the thermal processes. One can translate the E_{ex} to the Curie temperature, which may have very different values for different materials (ranging from few tens of K to few 100s of K). However, the typical

value of ξ_F is $\sim 3-5$ nm for strong ferromagnets such as Co and Ni [42] and ~ 10 nm for weak ferromagnets such as PdNi and CuNi [26,121]. Therefore, it is also known as short-range proximity effect.

The exchange field of ferromagnet causes phase shift ϕ_\uparrow and ϕ_\downarrow for electrons with different spins. Therefore, the net phase difference of the $|\uparrow\downarrow\rangle$ becomes $\phi_\uparrow - \phi_\downarrow = \theta$, also known as the spin-mixing angle. Similarly, the phase difference for $|\downarrow\uparrow\rangle$ becomes $\phi_\downarrow - \phi_\uparrow = -\theta$. Therefore, θ corresponds to the phase difference between the up spin electron with momentum k_\uparrow and the down spin electron with momentum $-k_\downarrow$, constituting the Cooper-pair. Then, the singlet Cooper-pair in the F becomes:

$$\frac{1}{\sqrt{2}}(|\uparrow\downarrow\rangle - |\downarrow\uparrow\rangle) \longrightarrow \frac{1}{\sqrt{2}}(|\uparrow\downarrow\rangle e^{i\theta} - |\downarrow\uparrow\rangle e^{-i\theta})$$

This can be written as:

$$\frac{1}{\sqrt{2}}[(|\uparrow\downarrow\rangle - |\downarrow\uparrow\rangle)\cos\theta + i(|\uparrow\downarrow\rangle + |\downarrow\uparrow\rangle)\sin\theta]$$

Here, we obtain a mixture of singlet and triplet components with $S_z=0$ spin projection, similar to the case above. However, the Cooper-pair acquires a phase shift θ instead of momentum. The phase shift θ can be considered as a measure of singlet-triplet mixing, which is necessary for the generation of triplet pairs in S/F hybrids.

Due to this phase shift θ gained by the Cooper-pair, the order parameter oscillates with an oscillation period ξ_{F2} , which leads to a new phase state, known as π ground state [39], as shown in Fig. 1.10(b).

The oscillatory nature of this short-range proximity effect has been reported to give rise to very interesting effects in S/F heterostructures. For example, these oscillations are known to result in oscillations of critical superconducting temperature (T_c) with F-layer thickness in S/F structures [44–46], and oscillation of Josephson critical current (I_c) as a function of F-layer thickness [47–49]. The short-range S/F proximity effect in these systems is an extensively studied area. Our interest in S / F systems, on the other hand, lies in the exotic long-range proximity effect that

is predicted to occur in such systems under certain conditions. The next section describes more about this long-range proximity effect.

1.5.3 Long-range proximity effects

As discussed previously, the spin-dependent density of states at the Fermi level leads to a phase shift of the Cooper-pair, known as spin-mixing, which gives spin $S_z=0$ triplet component in addition to the $S_z=0$ singlet component. It is natural to wonder whether it is possible to generate other triplet components with spin $S_z = \pm 1$ at the S/F interface. Such pairs will have electrons with spins orienting in same direction and, therefore, they will be immune to any destructive effect due to the E_{ex} of ferromagnet [50–53]. Therefore, they can travel up to long distances in a ferromagnet, as shown in Fig. 1.11(a). These can provide dissipationless spin-polarized current and hence, can address one of the major challenges associated with superconducting-spintronics. In 2001, Bergeret *et al.* made a prediction that

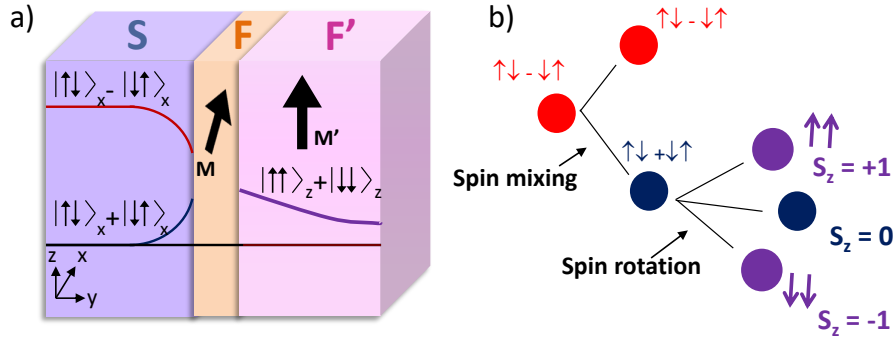


Figure 1.11: (a) Schematic illustration showing the mechanism of singlet-triplet Cooper-pair conversion at an S/F interface. The misaligned moments at the S/F interface and F' layer rotates the $S_z=0$ triplet component in spin space and converts them to $S_z=\pm 1$ triplet component [50,52,53], (b) Schematic showing the spin-mixing and spin-rotation process at the S/F and F/F' interfaces [52]

it is possible to generate long-range spin polarized triplet Cooper-pairs through a magnetic inhomogeneity at an S/F interface. To understand this, we consider a case where there are two F and F' layers adjacent to the S layer, as shown in Fig. 1.11(a). The respective magnetizations M and M' of F and F' layers are along x

and z directions, respectively. As discussed earlier, at the S/F interface, a mixture of singlet and triplet $S_x=0$ components are obtained due to the phase shift acquired by the Cooper-pair in F. However, this triplet state is short-range in nature due to zero spin projection along the x-axis. In the F'layer, the spin quantization axis of the singlet-triplet mixture is defined as the direction of M' (z-axis). Due to spin-rotation at F/F' interface, the triplet state with $S_x = 0$ decomposes to $|\uparrow\uparrow\rangle_z$ and $|\downarrow\downarrow\rangle_z$ with spin-projection 1 and -1 along the z-axis, as shown in Fig. 1.11(b). These pairs are known as spin-polarized triplet Cooper-pairs. Since the spins of both the electrons are same, the exchange field of ferromagnet has no destructive effect on the transport of these Cooper-pairs. They can travel through the ferromagnet like the case of a normal metal. The decay length of spin-polarized triplet Cooper-pairs is given as [50]:

$$\xi_F^{Tr} = \sqrt{\frac{\hbar D_F}{K_B T}}$$

which is similar to the case of S/N proximity effect. Therefore, its value is much higher compared to the zero spin-projection triplet Cooper-pairs. In practice, it has been demonstrated to be about tens of nm in a strong ferromagnet such as Co [10,11] and about a micron in a half-metal CrO_2 [9]. The amplitude of triplet correlations depends on the amount of magnetic inhomogeneity at the S/F interface.

1.5.3.1 Bloch sphere representation of triplet generation mechanism

In this section, we have tried to give a simplified picture of the generation mechanism of triplet Cooper-pairs from singlet Cooper-pairs. Here, we emphasize the importance of non-collinear magnetization in the generation of long-range triplet correlations (LRTC). As discussed in the previous section, a Cooper-pair acquires a center of mass momentum Q on entering a ferromagnet at the S/F interface. Therefore, the singlet Cooper-pair in superconductor transform as a mixture of singlet and triplet Cooper-pairs in the ferromagnet transforms as:

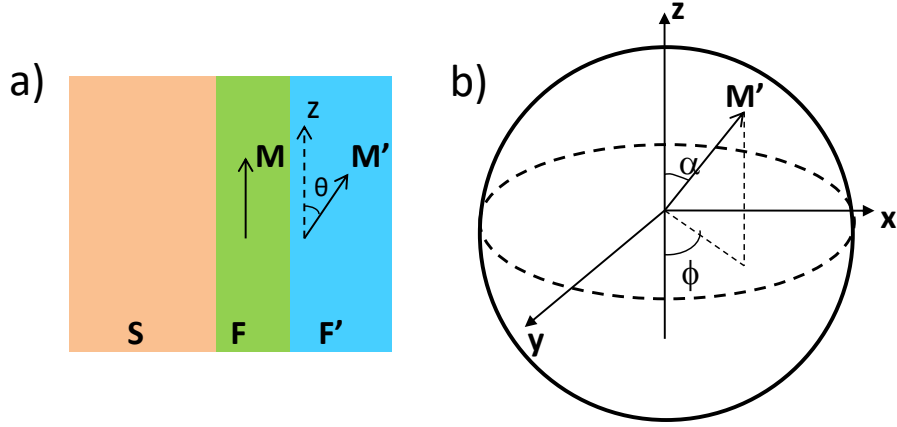


Figure 1.12: (a) Schematic illustration showing the S/F/F' trilayer, where the magnetization M and M' are misaligned relative to each other, (b) Bloch sphere representation of spin-rotation process at F/F' interface. The magnetization (M) of F layer is along the z direction while the direction of magnetization (M') of F' layer is at an angle (α, ϕ) in the Bloch sphere.

$$\frac{1}{\sqrt{2}}(|\uparrow\downarrow\rangle - |\downarrow\uparrow\rangle) \longrightarrow \frac{1}{\sqrt{2}}(|\uparrow\downarrow\rangle e^{ix.Q} - |\downarrow\uparrow\rangle e^{-ix.Q})$$

This can be written as:

$$\frac{1}{\sqrt{2}}[(|\uparrow\downarrow\rangle - |\downarrow\uparrow\rangle)\cos(x.Q) + i(|\uparrow\downarrow\rangle + |\downarrow\uparrow\rangle)\sin(x.Q)]$$

Here, the first term is the singlet state and the second term is a triplet state with spin projection $S_z = 0$, where z -axis is the spin quantization axis, which is defined by the direction of the magnetization of F.

Let us consider another ferromagnet F' with magnetization at an angle with the magnetization of F layer, as shown in the schematic of Fig. 1.12(a). Considering the general orientation of the magnetization in a Bloch sphere, we parameterize its direction by polar and azimuthal angles, α and ϕ , respectively, measured from the z -axis in spin space, as shown in Fig. 1.12(b). From the formulas of basis transformation, we can represent basis vectors quantized along the α, ϕ direction in terms of the basis vectors quantized along the z -axis as [51]:

$$\begin{aligned} \uparrow_{\alpha, \phi} &= \cos\frac{\alpha}{2} e^{-i\frac{\phi}{2}} \uparrow_z + \sin\frac{\alpha}{2} e^{i\frac{\phi}{2}} \downarrow_z \\ \downarrow_{\alpha, \phi} &= -\sin\frac{\alpha}{2} e^{-i\frac{\phi}{2}} \uparrow_z + \cos\frac{\alpha}{2} e^{i\frac{\phi}{2}} \downarrow_z \end{aligned}$$

Therefore, the basis transformation of pair amplitudes can be written as:

$$\frac{1}{\sqrt{2}}(|\uparrow\downarrow\rangle - |\downarrow\uparrow\rangle)_{\alpha,\phi} = \frac{1}{\sqrt{2}}(|\uparrow\downarrow\rangle - |\downarrow\uparrow\rangle)_z$$

$$\frac{1}{\sqrt{2}}(|\uparrow\downarrow\rangle + |\downarrow\uparrow\rangle)_{\alpha,\phi} = \frac{1}{\sqrt{2}}(-\sin\alpha[e^{-i\phi}|\uparrow\uparrow\rangle - e^{i\phi}|\downarrow\downarrow\rangle]_z + \cos\alpha(|\uparrow\downarrow\rangle + |\downarrow\uparrow\rangle)_z)$$

Therefore, the $S_z = 0$ triplet Cooper-pair converts into $S_z = \pm 1$ triplet Cooper-pairs due to a rotation in spin-space, also known as spin rotation. These triplet Cooper-pairs are spin-polarized and therefore, can travel up to long distances in the ferromagnet.

1.5.3.2 Ways to induce LRTC in S / F hybrid Systems

Long-range effects occur only when the Cooper-pair passes through magnetically inhomogeneous regions at S/F interface. There are several ways in which the magnetic inhomogeneous structure can be created at S/F interface:

- **Spiral magnetic inhomogeneities and domain walls:** The domain walls of ferromagnets can provide the necessary non-collinear magnetization for the conversion from spin-singlet to spin-triplet Cooper-pairs. The domain wall should be at the S/F interface so that the singlet Cooper-pair can sense the magnetic non-collinearity and converts into triplet Cooper-pair. In this context, Bergeret *et al.* studied the effect of a Bloch domain wall at the S/F interface. They conclude that a small total angle of rotation of the magnetization is preferable to get large LRTC [8]. There are also theoretical proposals, which consider Néel domain wall as a magnetic non-collinear structure, in which the magnetization vector rotates along a direction parallel to the S/F interface. In these cases, long-range triplet components are predicted to arise at the domain walls. Some materials such as Holmium has intrinsic spiral magnetic order, which can be used as a magnetic inhomogeneity required for singlet-triplet pair conversion. Another system with inhomogeneous magnetic structure is a ferromagnetic disc, where a ferromagnetic vortex in the disc is

brought in contact with superconducting electrodes [54,55]. In this geometry, long-range triplet correlations are induced through the inhomogeneous structure of ferromagnetic vortex.

- Multi-layer geometries:** Magnetic non-collinearity can also be induced by using magnetic multilayers in such a way that the different F layer magnetizations are misaligned relative to each other. In this context, a diffusive structure $S/F'/F/F'/S$ was proposed by Houzet and Buzdin [15], where the magnetizations of F' and F layers are misaligned relative to each other. A diffusive $S/F'/F/F'/S$ structure is also discussed in the literature [56] to realize long-range triplet correlations. The middle F layer magnetization is misaligned relative to the F' layer magnetization. This structure was experimentally realized by Khaire *et al.* [10] in their experiments. It is also possible to generate triplet correlations in an $S/F_1/F_2/S$ Josephson junction with misaligned ferromagnetic layers F_1 and F_2 . However, in junctions with asymmetric magnetic barrier, Josephson current-phase relation is dominated by the second harmonic term [57]. Another diffusive structure $S/F/N/F/S$ was proposed [58], with a spin-valve embedded between two superconductors. The long-range triplet correlations are generated in this structure due to the misalignment between two F layers. Another example of multilayer geometry is an $F/S/F$ superconducting spin valve, where the magnetizations of two F layers are misaligned relative to each other and the thickness of the superconductor is less than its coherence length [52,59]. In this structure, the long-range triplet component arises due to the overlap of triplet components generated by the two F layers in the S layer. Another system to be discussed here is $S/F/F'$ spin-valve, where the thickness of S layer is lower than superconductor coherence length and magnetization vectors of F and F' are misaligned relative to each other [60]. Singlet-triplet pair conversion in this geometry is seen as a gradual decrease of T_c with the angle between the magnetizations of F and F' layers [61–65]. The T_c decreases due

to the leakage of singlet Cooper-pairs from S into F and their conversion into spin-aligned triplet Cooper-pairs through the non-collinear magnetization of F and F' layers. The maximum amplitude of triplet correlations is obtained when the magnetizations of F and F' layers are perpendicular to each other [50–52].

- **Spin Active Interfaces:** Another way to create an inhomogeneous magnetization is a spin active interface that allows for spin-flip processes. One such example [66] is a half-metallic ferromagnet, CrO₂, in which electrons with only one spin orientation exists at the Fermi level. In this case, the spin-dependent scattering happens at the S/F interface and the spin-rotation happens due to the misalignment between the interface magnetic moment and bulk magnetization of the ferromagnet. This leads to the creation of long-range spin-triplet correlations in this structure [9,66].
- **Spin injection:** In an S/F/S Josephson junction, long-range triplet correlations can be induced by injecting spin into the superconducting electrodes [67], as shown in the schematic of Fig. 1.13.

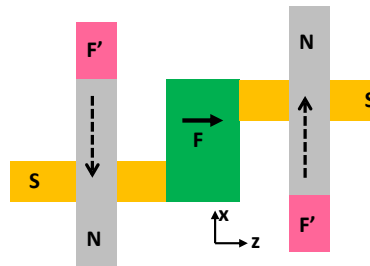


Figure 1.13: Schematic of the device geometry proposed for generating long-range triplet supercurrents by spin-injection [67].

The non-collinear magnetization for triplet supercurrent generation is provided by the relative angle between the spin-polarizations in the superconductor and the ferromagnetic layer. In fact, it is possible to vary the magnitude and sign of long-range triplet supercurrents by varying the relative angle between the injected spin-polarizations and the ferromagnet layer.

- **Precessing magnetization:** In a diffusive S/F/S Josephson junction, a time-varying magnetization vector can also induce long-range triplet correlations, as suggested by Houzet in 2008 [68]. The non-collinear orientation of time-varying exchange field and spin resolved chemical potential of the superconductors generates the long-range proximity effect. The long-range Josephson current may be observed by performing FMR measurements in a planar S/F/S Josephson junction [68].
- **Spin-orbit coupling:** Long-range triplet correlations can also be induced in S/F/N structure, where the normal metal layer exhibits spin-orbit coupling [69]. The spin-orbit coupling causes the spin-rotation of the triplet $S_z = 0$ component of S/F structure. In these systems, the non-collinear magnetizations of different F layers is not needed. Another structure to be discussed in this case is S/F₁/F₂ multilayer, where the magnetizations of F₁ and F₂ are in the same direction with a spin-orbit coupling at the interface of two F layers. This is to be noted that the spin-orbit coupling discussed in this case is due to a lack in inversion symmetry, which is different from the spin-orbit coupling arising from the disorder in the system [69]. Lack of inversion symmetry can be due to crystallographic inversion asymmetry or lack of structure inversion symmetry or due to the presence of interfaces between materials [69]. It was also demonstrated by Bergeret *et al.* [69] that it is better to use lateral S/F structures rather than multilayer transversal geometry to induce singlet-triplet conversion via spin-orbit coupling.

1.6 Previous studies of long-range triplet supercurrents

In the 1990s, the rapid development of spintronics and spin-based transport phenomena strongly motivated the search for long-range superconducting proximity effects. The long-range triplet supercurrents in Josephson junctions would ultimately lead to

valuable applications in the field of superconducting-spintronics. The long-range triplet correlations are predicted to occur only in the presence of an inhomogeneous magnetization. However, Petrashov *et al.* [70] in 1994 observed an unexpected decrease in the resistance of ferromagnetic Ni wire of length greater than $2 \mu\text{m}$, when attached to superconducting Al islands at the ends of the wire. This long-range proximity effect could not be explained in terms of spin-singlet correlations, which exceeds 30 times than the expected length scale of $\hbar v_F/|J|$, where v_F is Fermi velocity and J is exchange-integral. This observation was indeed a surprise and was attributed to anomalous interface effects. Another study [71] on Sn/Ni/Sn structures with ~ 40 nm wide Ni wire, showed an unexpectedly long proximity length of ~ 50 nm, much higher than the theoretically predicted value of 4 nm. Petrashov *et al.* [72] in 1999 observed a giant mutual proximity effect in Ni/Al structures, with conductance values, two orders in magnitude higher than the theoretically predicted value. The observations in all these experiments were attributed to interface effects. However, the controversies led to a vivid discussion about the existence of long-range triplet correlations.

Later in 2001, F.S. Bergeret *et al.* [8] predicted triplet supercurrent in S/F structures for the first time by modeling a Bloch type domain wall at the S/F interface. In the limit of a short mean free path for both low and high transparency of the interface, calculations indicated a triplet supercurrent component with a decay length $\xi_F \sim 100$ nm inside the ferromagnetic layer. This study indicated for the first time that magnetization non-collinearity is an essential condition for the observation of spin-triplet supercurrent in S/F structures. A similar result was obtained by F. Volkov *et al.* [73] in 2003 in a model calculation of S/F multilayer where the magnetization direction of successive layers was rotated. These calculations were done in dirty limit and the results are valid for all temperatures below the critical temperature T_c . They have shown that the triplet component may arise in such a structure if the thickness of the superconducting layers $2d_S$ is less than or

comparable with the coherence length $\xi_S = \sqrt{D_S/2\pi K_B T}$. The penetration of triplet component was shown to be over a long distance $\xi_T = \sqrt{D_T/2\pi K_B T}$, thus ensuring a Josephson coupling between the nearest S layers.

The mechanism for triplet supercurrent generation was first explained by M. Eschrig *et al.* in 2003 [66]. At an S/F interface with a homogeneous ferromagnet, spin mixing gives short-range singlet and triplet components with zero spin projection ($S_z = 0$) [66]. When this short-range correlation encounters non-collinear magnetization in the ferromagnetic layer, spin rotation converts short-range $S_z = 0$ triplet component into long-range $S_z = \pm 1$ triplet component. This process gives spin-polarized triplet Cooper pairs ($S_z = \pm 1$) in which both the electrons of a pair are having same spin. The spin-polarized triplet Cooper pair can propagate through F without experiencing any pair-breaking effect due to Zeeman field. Therefore, triplet Cooper pairs can travel up to long distances in F [50]. In a calculation of Josephson coupling through a half-metallic layer, Eschrig *et al.* [66] showed that a combination of spin mixing and spin-flip scattering at the superconductor/half-metal interface could lead to a Josephson coupling via equal-spin pair correlation, where singlet Josephson coupling is strictly cut off due to the half-metallic nature of the barrier. This was a compelling finding in favor of the argument that spin-mixing and spin rotation are the two essential components for the generation of long-range spin-triplet correlation. For this reason, natural and synthetic spiral magnetic structures are, in general, the subject matter of all calculations and experiments in this direction. The first experimental observation of long-range triplet current was reported by Keizer *et al.* [9] in 2006 in Josephson supercurrent measurement through a completely spin-polarized, half-metallic ferromagnet CrO_2 . Because of its half-metallic nature, it should not allow any singlet cooper pairs to pass through it. However, a current was observed in a planar S/F/S structure with NbTiN as the superconductor and CrO_2 as the half-metallic ferromagnet, as shown in Fig. 1.14. Supercurrent was observed with as much as 1 μm gap between the superconducting electrodes, which

is much longer than the expected length scale for singlet supercurrent. Theoretically, this current depends on the orientation of the magnetization in the ferromagnet, and to observe a Josephson current, both S/F and F/S interfaces should be magnetically non-collinear. However, in this experiment, a large spread in critical currents was observed suggesting that the process creating the inhomogeneous field and thus the process responsible for the singlet-triplet conversion is poorly defined. Another experiment reporting phase-dependent conductance oscillations of a Holmium (Ho) wire attached to superconducting electrodes on its both side were attributed to the presence of triplet correlations [74]. It was believed that the spiral magnetization in Ho is responsible for triplet correlations. After the above mentioned experiments, there was a surge in the number of theory papers suggesting possible ways to generate LRTC.

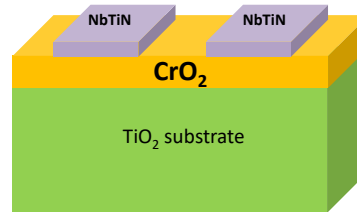


Figure 1.14: Schematic of the device geometry used for generating long-range triplet supercurrents in Ref [9].

Calculations of Josephson current through a conical ferromagnet, which have a Bloch type spiral magnetic structure (such as in metallic Holmium), by Volkov *et al.* [75] have shown that, for certain canting angles ($>19^\circ$), an exponential decay of the long-range triplet correlation into the ferromagnet can also show oscillations. Similarly, the possibility of triplet correlation in a Néel type domain wall structure in a ferromagnet was explored by Ya. V. Fominov *et al.*, in a S/F/S structure. Recently, Baker *et al.* [131] have proposed that an exchange-spring bilayer (soft-hard combination of ferromagnets) could be an interesting way to controllably generate Long Range Triplet supercurrent Component (LRTC) using external field, because, the relative magnetization twist of the soft layer with respect to the hard layer is

field dependent. They have also shown a new kind of singlet-triplet current reversal which is qualitatively different from the $0-\pi$ supercurrent reversal proposed by Buzdin *et al.* [39]. The great advantage of an exchange spring is that the bilayer can be continuously changed from a homogeneous magnetic system to a stable Bloch domain wall only via the external magnetic field of a few mT. Calculations by Baker *et al.* [131], using parameters of two prototype exchange spring systems (Co/Py and Ni₃Mn/Ni), have shown tunable LRTC with magnetic field, in addition to a small singlet super-current component which dies out very quickly in the ferromagnetic layer.

On experimental fronts, the first strong evidence of spin-triplet supercurrent was given by Khaire *et al.* [10] in 2010 in multilayer Nb/X/Co/Ru/Co/X/Nb Josephson junctions shown in Fig. 1.15, where X is PdNi or CuNi. Magnetic inhomogeneity was realized by thin layers of a weakly-ferromagnetic alloy PdNi or CuNi. The critical current of similar Josephson junctions containing Co/Ru/Co trilayers, but without the PdNi(CuNi) layers, were found to decay exponentially with increasing Co thickness [77]. Subsequently, Robinson *et al.* [11] reported spin-triplet supercurrent in Josephson junctions (in Nb/Ho/Co/Ho/Nb geometry) containing Holmium which has a natural spiral magnetic structure providing necessary magnetic inhomogeneity at the two interfaces. The decay length of critical current was found to be much higher (>10 nm) in Ho based junctions compared to Rh based junctions, which have no spiral magnetic structure. In another report, Sprungmann *et al.* [78] used a Heusler compound Cu₂MnAl as the F-layer in a Josephson junction structure. They found that in the non-magnetic (as deposited) state of Cu₂MnAl, critical current decreased exponentially with thickness, while in the magnetic (annealed) state, a significant increase in the critical current decay length was observed. A disordered spin-glass like interface at the S-F boundary was believed to form a canted ferromagnetic state, when the core of the Heusler alloy becomes magnetic after annealing, acting as the source of inhomogeneous field producing triplet current, in this case. However, unambiguous

proof of the triplet character of the supercurrent is not provided by their experimental results. In a recent experiment by Martinez *et al.* [17] S/F''/N/SAF/N/F'/S type structure was used to controllably switch triplet current on and off. Here F'' and F' were thin ferromagnetic layers which provide inhomogeneous magnetization, N was a non-magnetic spacer, and SAF was a “synthetic antiferromagnet” (Co/Ru/Co trilayer). SAF was used to minimize magnetic flux in the junction [79]. Such a structure turns on/off spin-triplet supercurrents using small magnetic fields [80]. Iovan *et al.* [16] used Nb/CuNi/Cu/CuNi/Nb spin-valve junction to control triplet supercurrents via relative orientation of two CuNi layers. Bernardo *et al.* [81] investigated triplet supercurrents in Nb/Ho bilayers by studying magnetic-phase-dependent superconducting subgap DOS in Nb. Visani *et al.* [82] reported quasiparticle and electron interference effects in the conductance spectra of YBCO/LCMO interfaces which demonstrate the long-range propagation of superconducting correlations across LCMO and imply the occurrence of unconventional equal-spin Andreev reflection. In a separate experiment, Gu *et al.* [83] measured the resistance of a Py/SmFe/Nb trilayer in which the magnetization twist of the magnetically soft Py layer was tuned with an external field. They observed a decrease in resistance up to a certain critical angle, which was interpreted as a signature of increasing long-range triplet component (LRTC). In a follow-up experiment, Zhu *et al.* [84] also found similar response of resistance in a Nb/Py/SmCo superconductor/exchange spring system.

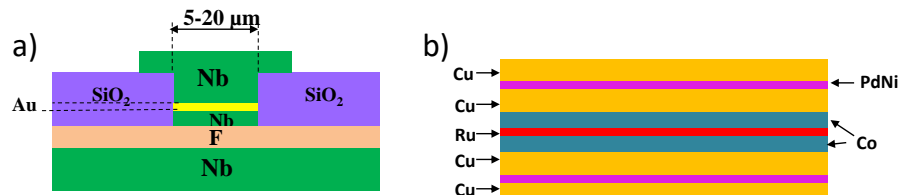


Figure 1.15: (a) Schematic of the device geometry used for generating long-range triplet supercurrents in Ref [10] (b) Schematic of the multilayer structure (F) used between the two Nb electrodes shown in Fig. 1.15(a).

1.7 Theme of the thesis

From the above survey of the relevant literature, we find that the existence of triplet supercurrents has been experimentally demonstrated by using synthetic magnetic non-collinearity at S/F interface, which consists of multiple ferromagnetic layers adjacent to the superconducting layer. However, the control of triplet supercurrents is still a major goal of superconducting-spintronics. In this direction, Banerjee *et al.* [59] have shown control of triplet supercurrents in S/F'/N/F/N'/S Josephson junction while Iovan *et al.* [16] demonstrated a control with spin-valve structure S/F'/N/F'/S. In both of these experiments, the control of supercurrents was shown during the magnetization reversal process. Recently, Martinez *et al.* [17] demonstrated an on-off control of triplet supercurrents by changing the magnetization direction of soft ferromagnet Py in multi-ferromagnet S/F/S Josephson junction with low magnetic fields (\sim mT). However, we believe that a continuous tuning of triplet supercurrents with small applied fields is lacking in the literature. Besides, all the previous reports are based on synthetic magnetic non-collinearity made using several ferromagnetic layers adjacent to the superconducting layer. We know that the basic ingredient for the generation of triplet supercurrents is the magnetic inhomogeneity at the S/F interface. Therefore, the domain walls existing in ferromagnets are natural candidates. However, the domain wall exists at the interface of two domains in a ferromagnet. Therefore, it is difficult to isolate a domain wall and perform a supercurrent measurement through it.

This thesis is centered around using natural and synthetic domain walls as magnetic inhomogeneity to generate and control triplet supercurrents in superconducting multilayers and magnetic Josephson junctions. For this purpose, low T_c Nb has been used as the superconducting component. Ni has been used as the ferromagnetic material for natural domain wall induced triplet study while Co/Py exchange-spring bilayer has been used as a synthetic domain wall for the control of triplet

supercurrents. The motivation behind these studies is two-fold:

- To pin a domain-wall between two superconductor electrodes and study the generation of triplet supercurrents in such Josephson junctions.
- To use a tunable synthetic domain-wall [Co/Py exchange-spring (XS)] to generate and manipulate the triplet supercurrents through the S/XS/S Josephson junction.

1.8 Organization of the thesis

- Chapter 1 is an introduction to the basic concepts of triplet superconductivity and their generation mechanism in S/F hybrid structures and Josephson junctions. It also presents a contextual survey of the theoretical predictions and current experimental results concerning triplet supercurrents in S/F hybrid structures and S/F/S Josephson junctions.
- Chapter 2 is divided into two parts. In the first part, we have presented a detailed study of magnetization reversal and magnetic domain imaging of single layer Ni stripes using Kerr microscopy. Shape anisotropy and field orientation driven magnetization reversal was the primary objective of this study. Since most of this thesis deals with hybrid S/F structures, it becomes pertinent to analyze the effect of the ferromagnetic domain reversal mechanism on an overlying superconductor. Therefore, we have presented a study of the change in T_c of an overlying Nb layer on the Ni stripes, in the second part of this chapter.
- In chapter 3, we utilized the stripe geometry discussed in chapter 2 to study the singlet-triplet conversion process through the natural domain walls of Ni. For this purpose, a microscopic gap was carved in the Nb layer in a patterned Ni/Nb stripe. It is well known that when a current passes through constricted ferromagnetic regions, it causes spin accumulation at domain walls and gives

rise to domain wall magneto-resistance (DWMR) [85]. By carving a gap in the Nb layer, we were able to inject singlet Cooper pairs of Nb into the domain walls of Ni present underneath. In this Nb-Ni-Nb planar structure, We have utilized DWMR as a tool to study the effect of Cooper pair injection into domain walls, comparing DWMR above and below the superconducting transition temperature of Nb.

- In chapter 4, we present a direct measurement showing DWs indeed produce triplet from singlet supercurrents. For this purpose, we used a notched geometry to pin a single domain wall of Ni at the notch [86,87] in focused ion beam (FIB) patterned planar Nb-Ni-Nb junctions. We have fabricated Nb/Ni/Nb planar Josephson junctions, where the barrier width is ~ 70 nm, much higher than the singlet pair coherence length of Ni ($\xi_{Ni} \sim 4$ nm). Transport measurements were performed to confirm the triplet Josephson coupling in these junctions. We further fabricated DC-SQUID devices (with two Josephson junctions in a superconducting loop) using the same concept of pinning a domain wall in a planar Nb-Ni-Nb junction. These SQUID coupling in these devices were confirmed from flux modulations of voltage at a fixed bias current.
- Chapter 5 discusses the use of a Co/Py exchange-spring (XS) to investigate singlet-triplet conversion in S/XS/S multilayers. In a Co/Py XS, a non-collinear structure of magnetic moments forms in Py due to exchange-coupling at Co/Py interface. We have performed magnetization measurements to investigate the changes in T_c of S/XS/S multilayer. Utilizing the tunability of XS, we have also shown the tuning of T_c in the spring-range of Co/Py XS.
- Chapter 6 deals with the use of Co/Py XS (a synthetic domain-wall) to fabricate nano-pillar Josephson junctions to control triplet supercurrents magnetically. We have fabricated FIB based Josephson junctions using Co/Py (XS) and Py/Co/Py (double XS) magnetic barriers. We have performed transport measurements in

these devices for Py thicknesses varying from (1-13) nm and for fixed thickness of Co (2 nm) to confirm the existence of triplet supercurrents. We have also investigated a continuous manipulation of triplet supercurrents as a function of the direction of applied magnetic field for both symmetric and asymmetric junctions.

- Chapter 7 presents a brief summary of our experimental results on generation and control of triplet supercurrents using natural and synthetic domain walls. We also present key issues which are potentially interesting for future studies.

Chapter 2

Magnetization reversal in ferromagnetic film and ensuing effects on proximal superconducting films

2.1 Introduction

In superconducting-spintronics devices, superconducting (S) and ferromagnetic (F) layers are essential building blocks that work in unison [51,52]. In most cases, spintronics devices function by reversing the direction of magnetization in one or more F layers. It is well known that during the magnetization reversal of ferromagnet, domain walls (DW) start to form in ferromagnet which may cause significant stray magnetic fields. While the domain wall itself may be a useful entity for spintronics devices, the stray field may affect a proximal superconducting layer significantly. Therefore, it is very important to know the effect of DW stray fields on superconductor during the magnetization reversal of ferromagnet in a S/F hybrid system.

In ferromagnetic materials, a domain wall (DW) exists at the boundary of two magnetic domains. The DWs form as a result of the competition between anisotropy energy and the exchange energy of ferromagnet [88,89].

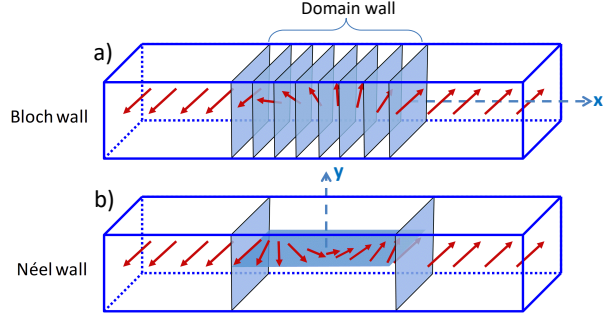


Figure 2.1: Schematic illustration of (a) a Bloch domain wall with spins rotating perpendicular and (b) a Néel domain wall with spins rotating in the plane of domain walls. The region shown between the two outer planes is a magnetic domain wall, which exists at the boundary of two magnetic domains.

The DWs are mainly classified as Bloch DW [90] and Néel DW [91], based on the spin structure inside the walls. In the case of Bloch walls, the rotation of magnetization happens in the plane of the DW, as shown in Fig. 2.1(a). The effective wall width in case of Bloch DW δ is given as [90]:

$$\delta_{BW} = \pi \sqrt{\frac{A}{K}}$$

Here, the constant A is known as exchange stiffness constant and K is the anisotropy constant. However, Bloch walls are energetically unfavorable for ferromagnet films with a thickness comparable to the width of the wall. For lower thickness films, Néel walls are energetically favorable in which the magnetization vector rotates perpendicular to the plane of the domain wall, as shown in Fig. 2.1(b). The width of the Néel DW is given as [91]:

$$\delta_{NW} = \pi \sqrt{\frac{2A}{\mu_0 M_s^2}}$$

where M_s is the saturation magnetization and μ_0 is the permeability of free space.

Since the thesis deals with domain walls and superconducting layers, we need to look at the magnetization reversal process of ferromagnet and the ensuing effects on superconducting T_c .

In this chapter, we have investigated the effect of stray fields of Néel and Bloch DWs of Ni on the overlying Nb film for temperatures below T_c . We studied

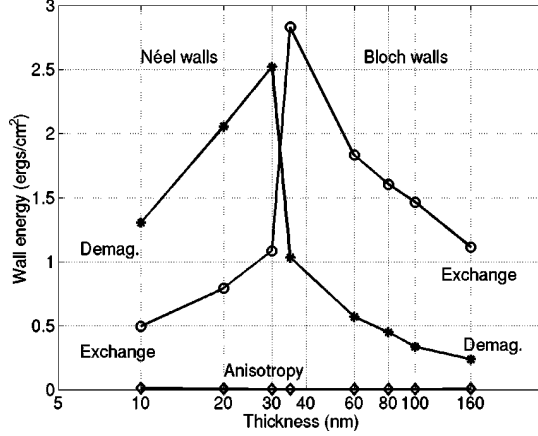


Figure 2.2: Thickness dependence of domain wall energy of Bloch and Néel domain walls [92].

domain configurations by Kerr microscopy measurements in longitudinal mode. We measured $T_c(H)$ curves for Ni/Nb stripes with Ni thicknesses varying from Néel DW to Bloch DW regime. We found a systematic variation of T_c suppression (ΔT_c) of Ni/Nb stripe with Ni thickness. ΔT_c can be mapped directly with the strength of DW stray field below T_c . A larger ΔT_c was observed for Bloch DW compared to Néel DW in a Ni/Nb stripe for temperature below T_c .

2.2 Experimental details

2.2.1 Sample Preparation

2.2.1.1 Thin film growth

Ni/Nb bilayers and plain Ni films were deposited at ambient temperature using DC-magnetron sputtering of high purity (99.99%) Nb and Ni targets on thermally grown Si/SiO₂ substrates. In the SiO₂/Ni/Nb sample, SiO₂ is the substrate, Ni is the bottom layer and Nb is the top layer. The base pressure of the deposition chamber was of the order of 10^{-9} mBar. Prior to the deposition, substrates were cleaned by ultra-sonification in acetone and isopropanol baths. The thickness (d_{Ni})

of the Ni film was varied from 20 nm to 100 nm in steps of 20 nm, while the thickness of Nb layer was kept fixed at 55 nm, in case of Ni/Nb bilayer films. Plain Ni film of thickness 15 nm and 90 nm were also prepared for magnetization reversal study using Kerr microscopy.

2.2.1.2 Optical-lithography

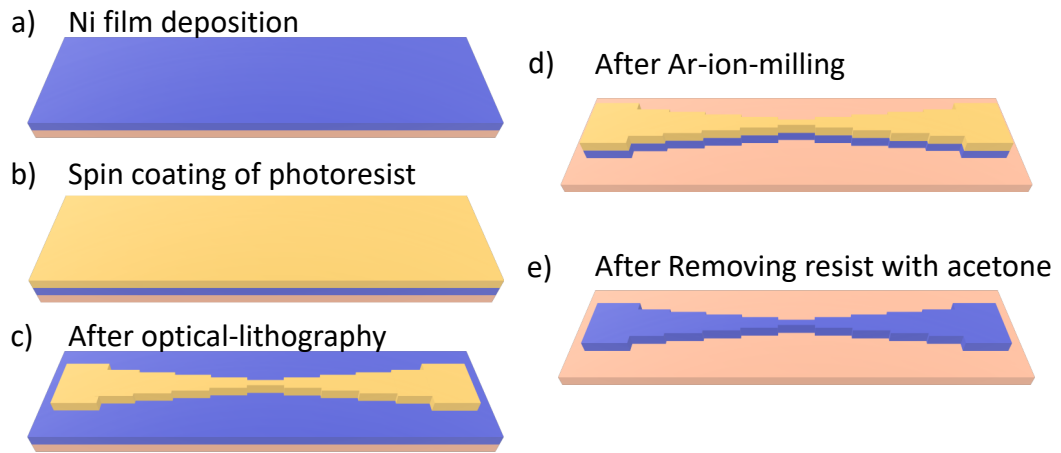


Figure 2.3: Steps followed during the patterning of Ni stripe.

After sputtering the Ni film on Si/SiO₂ substrate, we prepared Ni stripe with segments of varying widths using optical-lithography and Ar-ion-milling, as shown in Fig. 2.3. Optical lithography is a process of transferring a geometrical pattern from a photomask to a photosensitive chemical resist using light. Fig. 2.3 shows the steps followed during the fabrication of Ni stripe. At first, the Ni film was deposited on Si/SiO₂ substrate, as shown in Fig. 2.3(a). Then, a positive photoresist layer of thickness 0.5 μm was coated on the Ni film, using a spin-coater, as shown in Fig. 2.3(b). The photoresist was then baked at a temperature of 110 °C to remove the solvent and to improve the adhesion of the photoresist on the sample. The coated photoresist was then selectively exposed to UV light using a photomask. The photomask acts as a stencil with the desired stripe pattern. The coated resist was then developed using a dilute NaOH developer solution. The exposed areas were dissolved in the developer solution, leaving the unexposed areas with the stripe

pattern, as shown in Fig. 2.3(c). This process created a photoresist pattern with segments of different aspect ratios on the Ni film. In the next step, we used the Ar-ion-milling process to remove the Ni film present outside the resist pattern, as shown in Fig. 2.3(d). Ar-ion-milling is purely a physical etching process, where Ar ions are accelerated from an ion-source onto the material to be etched. This results in a high-resolution anisotropic etching of materials. The photoresist pattern created using optical-lithography acts as a mask during the ion-milling process. The base pressure during the milling process was 2×10^{-6} mBar in our experiment. The milling was performed at an Ar pressure of 8×10^{-2} mBar for about 8 minutes, for a Ni layer of thickness 90 nm. After the milling process, photoresist pattern remained with the Ni layer present underneath, as shown in Fig. 2.3(d). The photoresist layer was removed by dipping the sample in acetone. The result was a Ni stripe with different segments, as shown in Fig. 2.3(e).

2.2.1.3 Electron Beam lithography

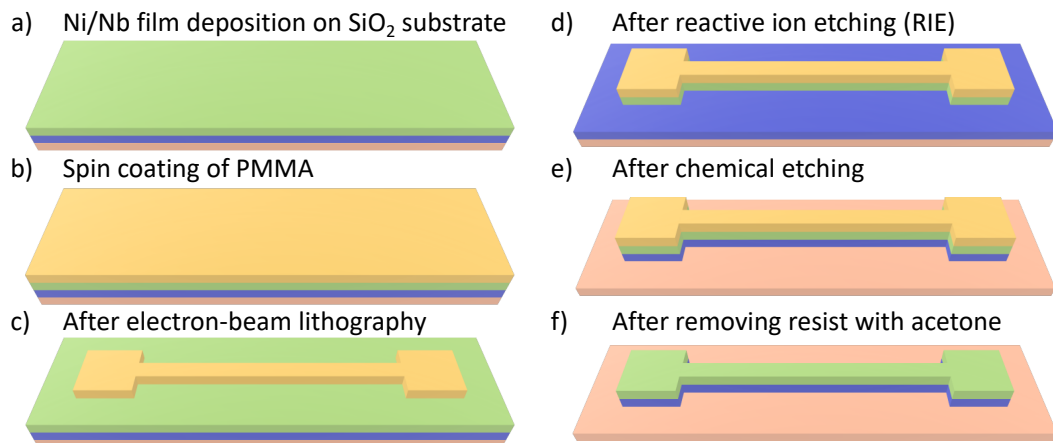


Figure 2.4: Steps followed during the patterning of Ni/Nb stripe.

After sputtering the Ni/Nb bilayer films, we prepared Ni/Nb bilayer stripe of width $\sim 3 \mu\text{m}$, using electron-beam lithography, reactive ion etching (RIE) and chemical etching process, as shown in Fig. 2.4. Electron-beam lithography (EBL) is a process of writing the desired geometrical pattern on a sample covered with an electron

sensitive resist, using the scanning electron-beam. Unlike the optical-lithography, the geometrical patterns with a resolution of ~ 10 nm can be achieved using EBL. Fig. 2.4 shows the steps followed during the sample fabrication process. At first, the Ni/Nb bilayer films were deposited on Si/SiO₂ substrate, using DC-magnetron sputtering. Then, an electron-sensitive resist, PMMA (Polymethyl methacrylate) was spin-coated on the bilayer film, as shown in Fig. 2.4(b). The resist was then baked at a temperature of 110 °C to improve the adhesion of the resist layer on the sample. PMMA is a positive resist, composed of big organic molecules. The effect of the electron beam on PMMA is to break the molecule into small parts, which are easily soluble in the developer solution. After the development, the resist pattern was left with Ni/Nb bilayer films present underneath, as shown in Fig. 2.4(c). Next, we used an Oxford reactive ion etching (RIE) system to selectively remove the Nb layer present outside the resist pattern, as shown in Fig. 2.4(d). The resist pattern acts as an etch mask during the RIE process. For Nb etching, 120 watt SF₆ plasma was used. RIE process performs both physical and chemical etching of the sample. This process is material sensitive, unlike Ar-ion-milling. Different materials can be etched with different gases. After the removal of Nb film, the next step was to remove the Ni film present outside the resist pattern. We performed a wet chemical etching process, which uses a dilute commercial Nichrome etchant from Aldrich. After the chemical etching process, photoresist pattern remained with the Ni/Nb bilayer films present underneath, as shown in Fig. 2.4(e). The photoresist layer was then removed with acetone. The result was a Ni/Nb stripe of width 3 μm , as shown in Fig. 2.4(f).

2.2.2 Domain imaging using Kerr microscope

The change in the polarization of light, when reflected from a magnetized surface, is known as the magneto-optic Kerr effect (MOKE) [93], as shown in the schematic of Fig. 2.5.

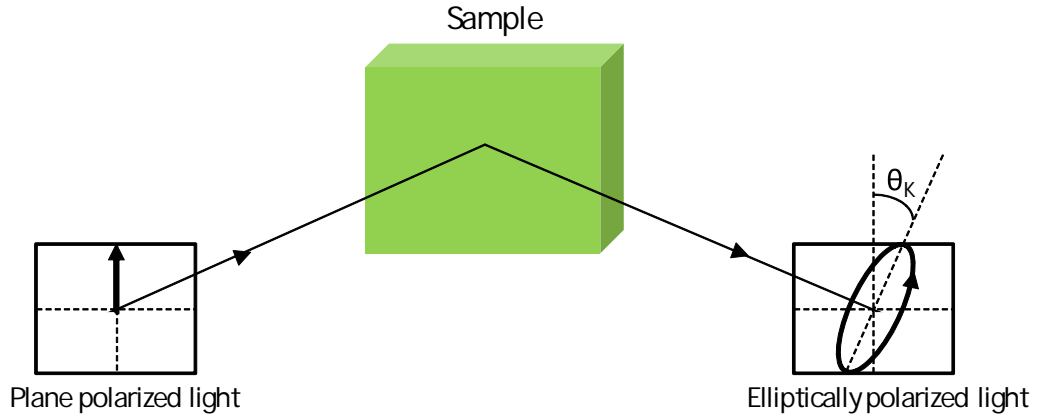


Figure 2.5: Schematic of MOKE showing the formation of elliptically polarized light from the incident linearly polarized light [94]. The incident linearly polarized light converts into elliptically polarized light after being reflected from the magnetized sample. The polarization axis is rotated by an angle θ_K , known as Kerr-rotation.

2.2.2.1 MOKE measurement geometries

MOKE measurement geometries can be classified in three different categories based on the angle between the direction of magnetization of the sample and the plane of incidence of light as [38]:

- Longitudinal MOKE:** If the direction of magnetization of the sample is parallel to the plane of the film and the plane of incidence of light, as shown in Fig. 2.6(a), the geometry is known as longitudinal MOKE. In this case, the linearly polarized light converts to elliptically polarized light with Kerr rotation (θ_K) and ellipticity (ε_K) (the ratio of the major and minor axis of ellipse) after being reflected from the magnetized surface [93], as shown in Fig. 2.5. Therefore, one measures the Kerr rotation (θ_K) and ellipticity (ε_K) at the detector end [95]. Longitudinal MOKE is used for in-plane magnetized samples. In this chapter, we have performed Kerr microscopy measurements of Ni stripes in the longitudinal mode.
- Transverse MOKE:** If the direction of magnetization of sample is parallel to the plane of the film but perpendicular to the plane of incidence of light,

as shown in Fig. 2.6(b), the geometry is known as transverse MOKE. In this case, the change in intensity of plane polarized light is measured at the detector end.

- **Polar MOKE:** If the direction of magnetization of sample is perpendicular to the plane of the film but parallel to the plane of incidence of light, as shown in Fig. 2.6(c), the geometry is known as polar MOKE. In this case, the change in the plane of polarization and ellipticity is measured at the detector end. Polar MOKE is particularly used for out-of-plane magnetized samples.

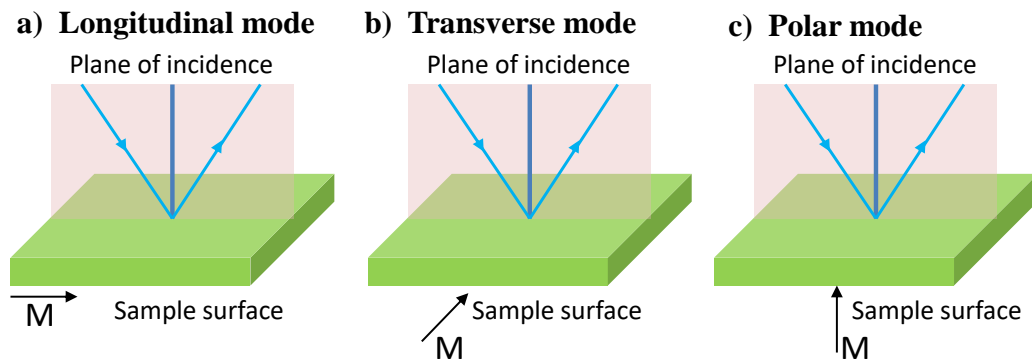


Figure 2.6: Schematic illustration showing different geometries of MOKE, (a) Longitudinal mode (b) Transverse mode, and (c) Polar mode. The incident and reflected light are in the same plane, which is marked as the plane of incidence.

2.2.2.2 Kerr-microscope set-up

Depending on the detector used, MOKE can act either as a magnetometer or a Kerr microscope [38]. In a Kerr microscope, the detector is replaced with a camera to image the magnetic domains in a magnetic thin film or magnetic multilayers. The resolution of the magnetic domain imaging in a Kerr microscope is limited by the wavelength of the visible light used in the set-up.

Fig. 2.7 shows the schematic illustration of magnetic domain imaging by Kerr-microscope [38]. We have considered a situation, where a plane-polarized light is incident on a magnetic sample having magnetic domains oriented in opposite

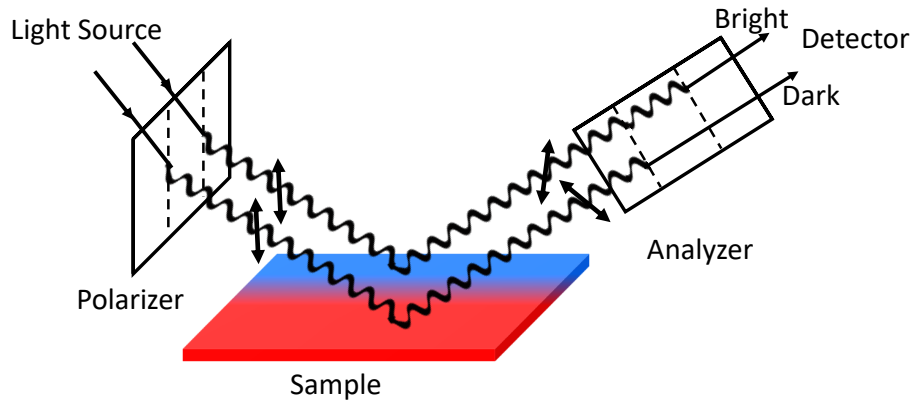


Figure 2.7: Finding magnetic domains using Kerr microscope set up [38], Red and blue color regions in the sample represent magnetic domains oriented in opposite directions.

directions (shown in red and blue color), in the plane of the film, as shown in Fig. 2.7. After being reflected from the magnetized sample, the plane of polarization of light rotates in different directions for the two magnetization orientations. Now, if the analyzer is placed aligned with the plane of polarization of the reflected light from one magnetic domain, the camera will generate a more intense (bright) image corresponding to this domain. However, since the analyzer is now misaligned with the polarization axis of other magnetic domain, the camera will generate a less intense (dark) image for this domain. Therefore, the contrast of different areas in the generated image gives information about the magnetization directions of the magnetic domains of the sample [38,96].

In our experiment, magnetic domains in Ni stripe were imaged using Kerr microscope supplied by Evico magnetics Ltd., which uses a white LED as a light source, with wavelength lying in the visible range. The measurements were performed at room temperature and in the longitudinal mode of the Kerr microscope. An external magnetic field was applied using an electromagnet to magnetize the sample.

2.2.2.3 Hysteresis cycles from magneto-optical images

While scanning the field from positive saturation to negative saturation, it is possible to extract both the magnetic domain images and the magnetization at each magnetic

field for a particular region of the sample. As discussed earlier, the plane-polarized light becomes elliptically polarized light after being reflected from a magnetized sample, as shown in Fig. 2.5. The angle through which the plane of polarization is rotated in this process, is known as Kerr rotation (θ_K), as shown in Fig. 2.5. The Kerr rotation and hence, the average intensity of the domain image in a particular region of interest is proportional to the magnetization of that region [33,97]. Therefore, the plot of average intensity signal versus applied field represents the magnetic hysteretic behavior of the region of interest in the sample. These hysteresis cycles were recorded for different orientations of the applied field with respect to the long axis of the sample shown in Fig. 2.8. From these hysteresis cycles, one can obtain the coercive field and its dependence on the width of the different segments of Ni stripe.

2.2.3 Transport and magnetization measurements

For transport measurements, standard four-probe contacts were made using wire bonder and measurements were performed using Quantum design PPMS. The direction of bias current was reversed for each voltage point and averaged over five measurements. The temperature stability was within ± 2 mK. Magnetization measurements ($M(H)$) were performed using SQUID-magnetometer.

2.3 Results and discussion

2.3.1 Shape anisotropy driven domain reversal in Néel and Bloch DW regimes of Ni

In Fig. 2.8, we show the field emission scanning electron microscope (FESEM) image of a Ni stripe having segments of different aspect ratios, marked as R_1 , R_2 , R_3 , R_4 , R_5 , and R_6 . The length of all the segments was $100 \mu\text{m}$ but the

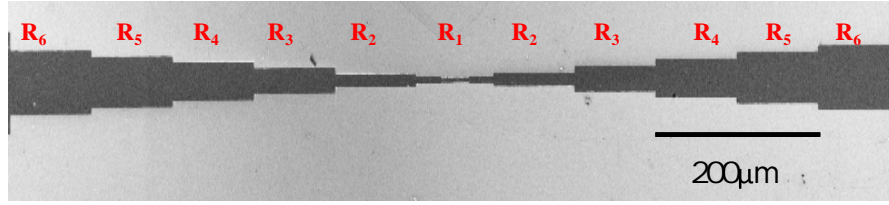


Figure 2.8: FESEM micrograph of the Ni stripes with aspect ratios (ratio of length to width of a segment) varying from 2 to 19.

width was varied from $5 \mu\text{m}$ to $50 \mu\text{m}$, respectively. In a magnetic thin film, the domain wall energy density is directly proportional to the film thickness for Néel DWs while it is inversely proportional to the film thickness for Bloch DWs. Therefore, Néel DWs are favored below a critical thickness while the Bloch DWs are favored [88,90,91] above the critical thickness. In the case of Ni, the critical thickness is $\sim 50 \text{ nm}$ [98,99]. In this section, we have discussed the Ni stripes, with thickness lying in the Néel regime (15 nm) and the Bloch regime (90 nm).

Fig. 2.9(a) shows the hysteresis loop for a rectangular region marked in black in a Ni (15 nm) stripe of aspect ratio 3.33 in Fig. 2.9(b) in parallel configuration (magnetic field applied along the length) in the Néel regime. Fig. 2.9(b), (c), (d), (e) show the Kerr microscope images of magnetic domains corresponding to points A, B, C, D marked in Fig. 2.9(a). The bright and dark portions in images represent magnetic domains oriented in opposite directions. Fig. 2.9(b) and (e) correspond to positive and negative saturation field. In Fig. 2.9(c), magnetization reversal starts in higher width part of the stripe. It then propagates towards the subsequent part of stripe with lower width. In Fig. 2.9(f), we show the hysteresis loop for a rectangular region marked in black in a stripe of aspect ratio 3.33 in Fig. 2.9(g) in transverse configuration (magnetic field applied along the width).

We observe that domain nucleation initiates in the lower width region, at some nucleation points, as shown in Fig. 2.9(h). Domains start growing about the nucleation points and form stripe-like structures, as shown in Fig. 2.9(i). The boundary of dark and bright part in the images represents a magnetic DW. Therefore, multiple

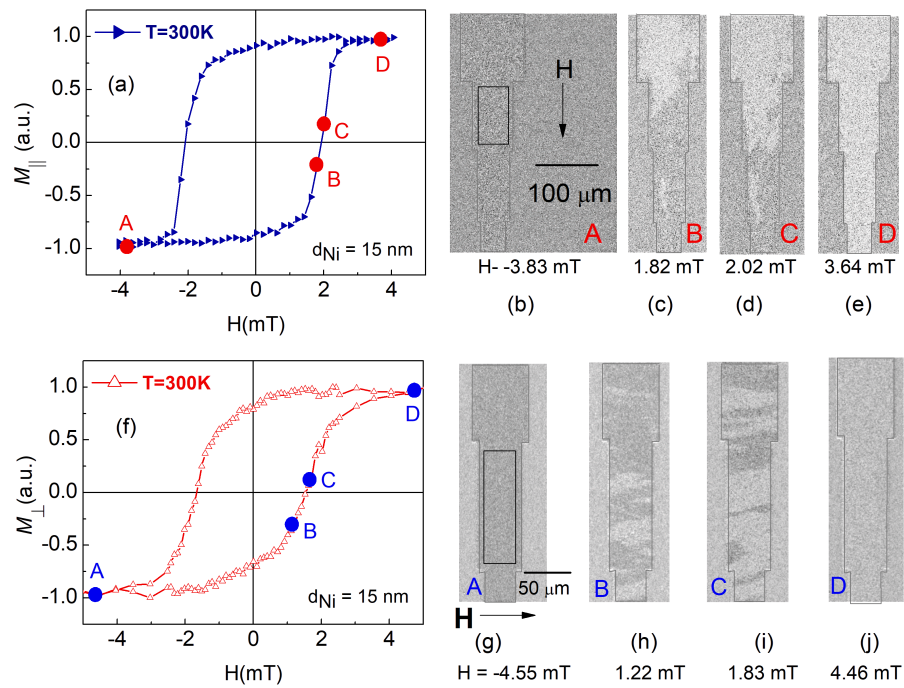


Figure 2.9: (a) $M(H)$ loop for segment R_3 of Ni stripe shown in Fig. 2.8 in parallel configuration at 300 K for Ni(15 nm) using Kerr microscope, (b), (c), (d), and (e) are the Kerr micro-graphs for points marked A, B, C, D in (a), Black arrows in (b) and (g) gives the direction of external magnetic field, (f) represents the $M(H)$ loop for segment R_3 of Ni stripe shown in Fig. 2.8 in transverse configuration at 300 K, (g), (h), (i), and (j) are the Kerr micro-graphs for point marked A, B, C, and D in (f). The scale bar shown in (b) is valid for all the images (b), (c), (d), and (e) and the scale bar shown in (g) is valid for all the images (g), (h), (i), and (j), respectively.

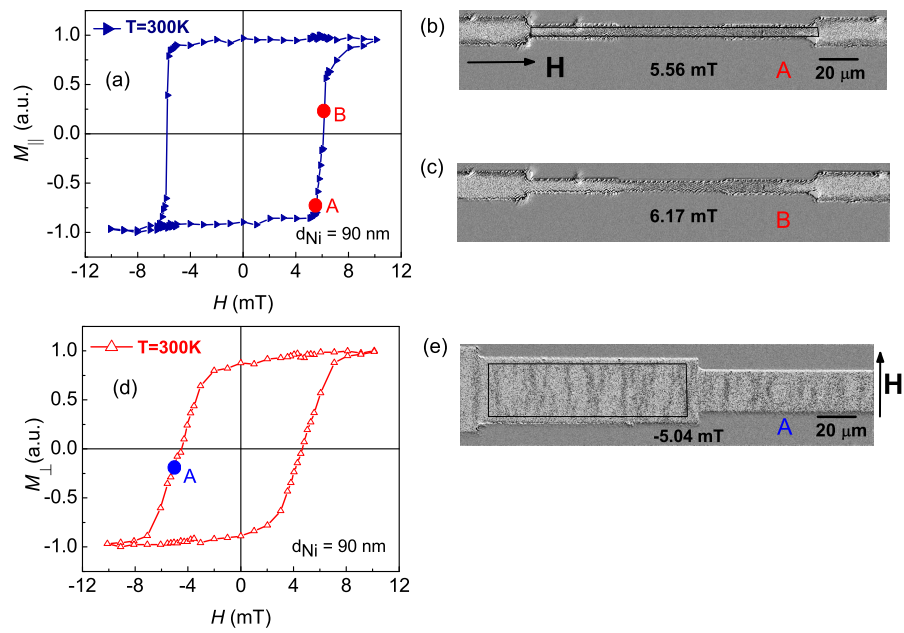


Figure 2.10: (a) $M(H)$ loop for segment R_1 of Ni stripe shown in Fig. 2.8(a) in parallel configuration at 300 K for Ni(90 nm) using Kerr microscope, (b), (c) are the Kerr micro-graphs for points marked A, B in (a); Black arrows in (b) and (e) denotes the direction of external magnetic field, (d) represents the $M(H)$ loop for segment R_3 of Ni stripe shown in Fig. 2.8(a) in transverse configuration at 300 K, (e) is the Kerr micro-graph for point marked A in (f); The scale bar shown in (b) is valid for all the images.

DWs were observed during magnetization reversal of the Ni stripe in transverse configuration.

In Fig. 2.10(a), we show the $M(H)$ loop for a rectangular region marked in black in a Ni (90 nm) stripe of aspect ratio 19.5 in Fig. 2.10(b) in parallel configuration in the Bloch regime. The domain reversal process is similar in segments with different aspect ratios in Fig. 2.8, therefore, the stripes have been chosen randomly for representation purpose. Propagation of two DWs was observed in parallel configuration, as shown in Fig. 2.10(b) and (c), whereas, In transverse configuration, multiple DWs and stripe-like domains were observed, as shown in Fig. 2.10(e).

Discussion

We recorded hysteresis loops for individual stripes using Kerr microscope to investigate the H_c vs width. For this purpose, $M(H)$ loops were extracted from Kerr images for parallel configuration and transverse configuration of Ni stripe. Fig. 2.11 shows the comparison of H_c of segments of Ni stripe with different widths in Néel and Bloch regime of thickness. A decrease in H_c was observed with increasing d_{Ni} in parallel configuration for Néel as well as Bloch DWs. In a stripe with thickness t and width w , the demagnetizing field $H_d \propto t/w$ [100]. In a patterned sample, the internal field is reduced to $H_i = H_a - H_d$, where H_a is the applied field. The $H_c(w)$ curves of Fig. 2.11(a) and (b) are fitted with a model given as [100]:

$$H_c = H_{c0} + A/w$$

Here H_{c0} is the coercive field of the film, A is a parameter depending on the saturation magnetization, shape anisotropy factor, and the thickness of the film. The assumption is that magnetization starts to reverse in a part of the stripe and then propagates along the stripe. For the fitting, H_0 and A are taken as free parameters. The value of H_0 comes out to be 2 mT and 6.5 mT for Ni (90 nm) and Ni

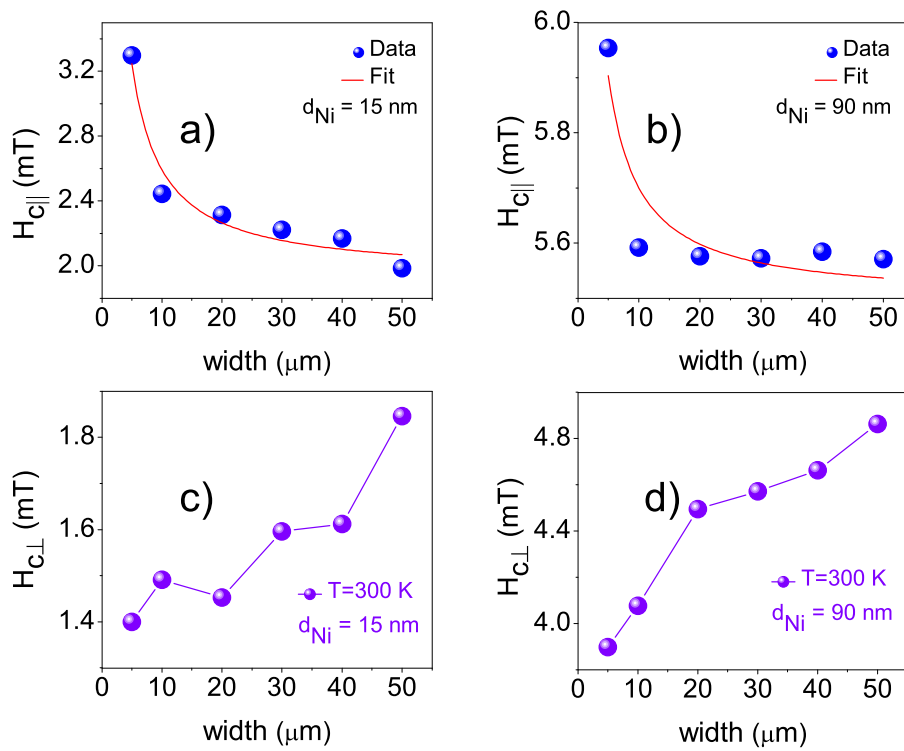


Figure 2.11: (a), (b) represents the coercive field (H_c) vs width (w) variation for parallel configuration (magnetic field (H) along the length) for Ni(15 nm) and Ni(90 nm). Red curves represents the fits to the data points shown in blue color. (c), (d) represents the coercive field (H_c) vs width (w) variation for transverse configuration (magnetic field (H) along the width) for Ni(15 nm) and Ni(90 nm).

(15 nm) stripes, respectively. These values are very close to the reported value of H_c of Ni [101]. The lower width stripe has higher shape anisotropy, leading to higher switching energy and consequently higher H_c . A reverse trend of $H_c(w)$ was obtained for transverse configuration, as shown in Fig. 2.11(c) and (d). A similar variation of $H_c(w)$ has been demonstrated in Co nanowires in a previous report [102].

2.3.2 Effect of domain wall stray field on superconducting transition temperature in Ni/Nb bilayer

After establishing the magnetization reversal process in patterned Ni stripes, our next aim was to study the effect of these DWs on an overlying Nb layer in a patterned Ni/Nb bilayer, as shown in the schematic of Fig. 2.12.



Figure 2.12: Schematic illustration showing an Ni/Nb bilayer stripe in four-probe geometry. An overlying Nb layer would directly sense the out-of-plane stray field of DWs of the Ni.

Typically, Bloch DWs have magnetic moments rotating out of the plane, as shown in Fig. 2.1(a) while Néel DWs have moments rotating in the plane of the ferromagnet, as shown in Fig. 2.1(b). Therefore, in an S/F bilayer stripe shown in Fig. 2.12, the two DWs should affect the overlying S layer differently due to the different out-of-plane stray field of these DWs.

In Fig. 2.13, we have shown the $M(H)$ loop of an unpatterned Ni/Nb bilayer at 10 K along with the $T_c(H)$ phase diagram of a Ni(40 nm)/Nb(55 nm) bilayer stripe. While reducing the field from saturation, the domain activity starts at the point where the hysteresis loop opens up. The domain activity region is marked

by dotted lines in Fig. 2.13. A decrease in transition temperature was observed with decreasing magnetic field in the field range, where magnetic domain activity starts. The low field T_c followed the $M(H)$ loop and the minimum value of T_c corresponded to the H_c of the $M(H)$ loop, as shown in Fig. 2.13. On reducing the field further beyond the coercive field, the T_c again recovered to the value corresponding to the saturation. The superconductivity of the overlying Nb layer is locally suppressed by the DW stray field which follows the $M(H)$ loop and is maximum at H_c . Therefore, T_c is minimum at H_c .

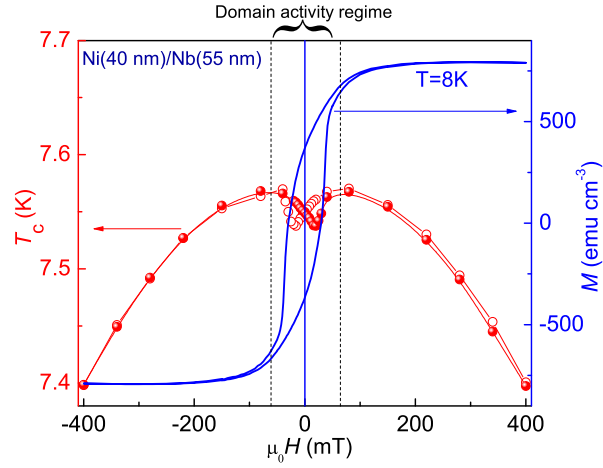


Figure 2.13: $T_c(H)$ curve for Ni(40nm)/Nb(55nm) bilayer stripe (Red points; left hand axis). An in-plane applied magnetic field is swept in backward and forward directions. The corresponding $M(H)$ loop (blue points; right hand axis) is at $T = 10$ K. Minima in low field $T_c(H)$ matches closely with the H_c of Ni.

In order to highlight the changes in T_c , we have shown normalized $R(T)$ curves in Fig. 2.14(a) for three different magnetic fields for patterned Ni(100 nm)/Nb(55 nm) bilayer. We have defined the T_c at resistance value 50% of the resistance at 10 K. We observe that the T_c for field value of -300 Oe is lower by ~ 64 mK compared to the T_c at 1572 Oe and -1572 Oe, because the former field is relatively closer to the coercive field value than the latter two.

We have shown a comparison of $T_c(H)$ curves for Ni/Nb stripes for Ni thickness of 20 nm, 40 nm, 80 nm and 100 nm in Fig. 2.14(b). We observe a suppression in T_c near H_c due to DW stray field in all cases. As shown in Fig. 2.14(b), the

effect was minimal in the case of Ni (20 nm)/Nb(55 nm) (Néel regime) and it was maximum for Ni (20 nm)/Nb(55 nm) (Bloch regime). Therefore, Bloch DWs have a higher out-of-plane component of the stray field compared to the Néel DWs. At saturation field, no DWs are present and, therefore, the DW stray field is zero and the T_c suppression is due to external magnetic fields.

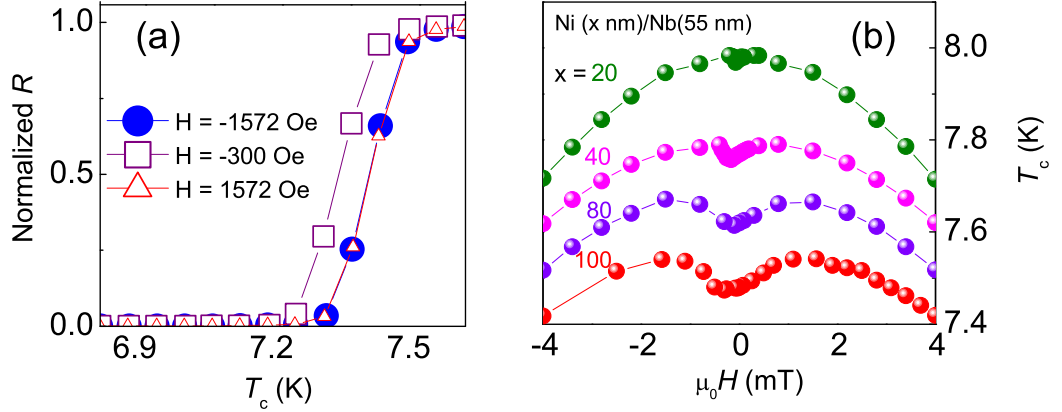


Figure 2.14: (a) Normalized $R(T)$ curves at field values near H_c (-300 Oe) and near saturation (1572 Oe, -1572 Oe) for Ni(100 nm)/Nb(55 nm) stripes. (b) $T_c(H)$ phase diagrams for Ni(x nm)/Nb(55 nm) stripes for $x = 20$ nm, 40 nm, 80 nm, and 100 nm.

Discussion

The number of domains and DWs in a ferromagnetic film follows the $M(H)$ loop. Therefore, the average stray field of ferromagnet is a function of the applied field. The stray field due to DWs becomes maximum at H_c and is zero at saturation. Following Patiño *et al.*, the field dependence of the stray field can be written as [103]:

$$H_s(H_{ap}) = H_{s_0}(1 - |M(H_a)/M_s|)$$

Here, H_{s_0} is the maximum stray field at H_c , M_s is the saturation magnetization and $M(H_a)$ is the magnetization of F at an applied field H_a , respectively.

We have plotted the calculated H_s in Fig. 2.15(a) using the above formalism. We find that the maximum stray field corresponds to the coercive field while the

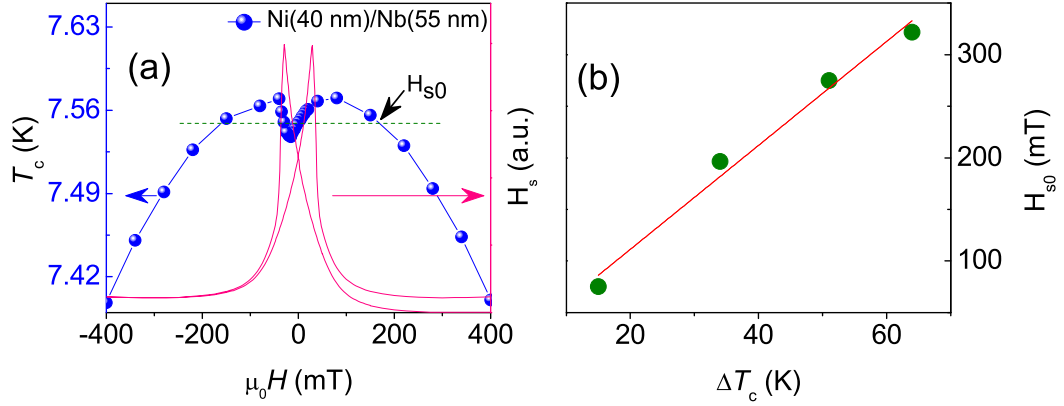


Figure 2.15: (a) $T_c(H)$ phase diagram of Ni(40 nm)/Nb(55 nm) stripes (blue points; left hand axis) and stray field (H_s) calculation for stripes from $M(H)$ loop measured at 10 K (pink points; right hand axis). The dashed horizontal line is drawn through the minimum T_c near H_c , giving an estimate of DW stray field (H_{s0}) from $T_c(H)$ phase diagram, (b) H_{s0} is plotted with maximum suppression in T_c obtained from $T_c(H)$ phase diagrams of panel b for Ni(x)/Nb(55 nm) stripes, where $x = 20$ nm, 40 nm, 80 nm, 100 nm.

minimum stray field is at saturation field. The comparison of $T_c(H)$ and $H_s(H)$ curves in Fig. 2.15(a) shows that the maximum suppression in T_c corresponds to the maximum stray field. A rough estimation of the maximum stray field can be done by tracing a horizontal line through the minimum T_c in the low field region of $T_c(H)$ curve. The intersection point of this line with the $T_c(H)$ curve gives an estimate of the maximum strength of the out-of-plane stray field (H_{s0}) of DW. Keeping in mind the fact that H in the $T_c(H)$ phase diagram is an in-plane magnetic field while DW stray field is an out-of-plane field, the value of H_{s0} determined from this method is not an exact one. However, it gives an upper limit to the strength of DW stray field. In Fig. 2.15(b), we have plotted the extracted estimate of H_{s0} with the change in T_c near the coercive field (ΔT_c), where ΔT_c is defined as the change in T_c near H_c . We observe that ΔT_c scales linearly with H_{s0} . In this way, superconductivity of the overlying Nb layer can be modulated by switching the domain walls either on or off in a S/F hybrid system.

2.4 Conclusion

We have investigated the magnetization reversal process of Ni stripes in Néel and Bloch DW regime of thickness using longitudinal Kerr microscopy. H_c decreased with increasing width of segments of Ni stripe in parallel configuration while it decreased with decreasing width of segments of Ni stripe in transverse configuration. In analogy to these results, Kerr microscopy images showed a DW propagation from the segment with a higher width to the segment with a lower width in the parallel configuration. Multiple stripe-like domains were observed in the transverse configuration. Next, we investigated the effect of these DWs on an overlying Ni film in Ni/Nb stripes for Ni thicknesses varying from the Néel DW regime to the Bloch DW regime. We studied the $T_c(H)$ phase diagrams following the $M(H)$ loop and found a suppressed T_c near H_c . The T_c suppression mapped directly with the DW density and hence, to the DW stray field. The suppression in T_c (~ 64 mK) was found to be higher in the Bloch regime compared to the Néel regime (~ 20 mK). The estimated DW stray field from $T_c(H)$ curves was found to scale with the suppression in T_c .

Chapter 3

Unconventional domain wall magnetoresistance of Nb-Ni-Nb planar structures below superconducting transition temperature of Nb

3.1 Introduction

It is now well established [8,9,51–53] that a magnetically inhomogeneous structure at S/F interface converts singlet Cooper pairs into triplet Cooper pairs. The domain walls (Néel and Bloch) in ferromagnets are natural magnetic inhomogeneities. However, the domain walls exist at the interface of two magnetic domains of a ferromagnet. Therefore, it is difficult to utilize domain walls as a triplet supercurrent generator in S/F/S Josephson junctions. Rather, all the previous experiments [10–12,16,59,81] have used synthetic magnetic non-collinear structures to realize singlet-triplet conversion in S/F hybrids and SFS Josephson junctions. It has been predicted theoretically that a magnetic domain wall (DW) at the S/F interface can be used to realize inhomogeneous exchange-interaction to convert singlet Cooper-pairs to triplet Cooper-

pairs [8,104,105]. In order to use DW as a singlet-triplet converter, singlet Cooper pairs must be injected into the domain walls.

In this chapter, insertion of singlet Cooper-pairs into DWs was facilitated by carving a microscopic gap in the superconducting layer in a Ni/Nb bilayer stripe, as shown in Fig. 3.2(a). We have measured the changes in domain wall magnetoresistance (DWMR) of the underlying Ni layer to study the effect of the Cooper-pair injection into DWs. In general, electric current through DWs in a ferromagnetic film leads to a spin-imbalance across the DW [85]. Although it is a very weak effect and is not observed in many cases, in narrow F stripes the contribution of spin accumulation appears as an increase in resistance of the stripes. This additional component of resistance, which scales with the number of domain walls in the path of the current, is termed as domain wall magneto-resistance (DWMR) [85,86,106]. Usually, DWMR follows the $M(H)$ loop and peaks at the coercive field (H_c) of F, because the number of DWs maximizes at H_c . The presence of a geometrical gap in Nb, as shown in Fig. 3.2(a), promotes the diffusion of supercurrent into Ni, below the T_c . In this process, some Cooper pairs may diffuse directly into DWs. Therefore, it is possible to measure the effects of Cooper-pair injection into domain walls by studying the modifications in DWMR below T_c .

For temperatures above T_c , we found that the measured DWMR of Nb/Ni/Nb planar structure corresponds well to $M(H)$ loop and hence, to the DW density of Ni. However, for temperatures below T_c , we observed an unconventional drop in DWMR in the field range of maximum domain activity. We have discussed the unconventional drop in DWMR in terms of S/F proximity effects, vortex locking-unlocking effects, DW superconductivity and DW induced triplet correlations. It appears that DW induced triplet correlations are the most likely responsible for the observed effects.

3.2 Experimental Details

3.2.1 Sample fabrication

Ni(100 nm)/Nb(55 nm) bilayer films were prepared at ambient temperature using DC-magnetron sputtering of high purity (99.99%) Nb and Ni targets on thermally grown Si/SiO₂ substrates. The base pressure of the deposition chamber was of the order of 10⁻⁹ mBar. A narrow bilayer stripe of width 6 μm, with contact pads at the ends, was made from the Ni/Nb bilayer films by following the steps shown in Fig. 3.1. After sputtering the Ni/Nb bilayer films, a photoresist layer was spin-coated, as shown in Fig. 3.1(a) and (b). Then the resist pattern was made using optical lithography, as shown in Fig. 3.1(c). Subsequently, Ar-ion-milling was performed to remove the Ni/Nb bilayer films present outside the resist pattern, as shown in the Fig. 3.1(d). Next, a new layer of photoresist pattern was spin-coated to define a gap of 3 μm in the top Nb layer of the stripe, as shown in Fig. 3.1(e). The exposed areas were removed after the development process, as shown in Fig. 3.1(g). Then, a selective etching of the Nb layer was performed using a CF₄ plasma in a reactive ion etching (RIE) system, as shown in Fig. 3.1(g). The photoresist layer was then removed by dipping the sample in acetone for 1 minute. This resulted in the requisite gap in the Nb layer, as shown in Fig. 3(h).

3.2.2 Transport measurements

For transport measurements, standard four-probe contacts were made using wire bonder and measurements were performed using a commercial cryogen-free cryostat system. The direction of bias current was reversed for each voltage point and averaged over five measurements. The temperature stability was within ±3 mK. Magnetic domains in Ni stripes were imaged using longitudinal Kerr microscopy.

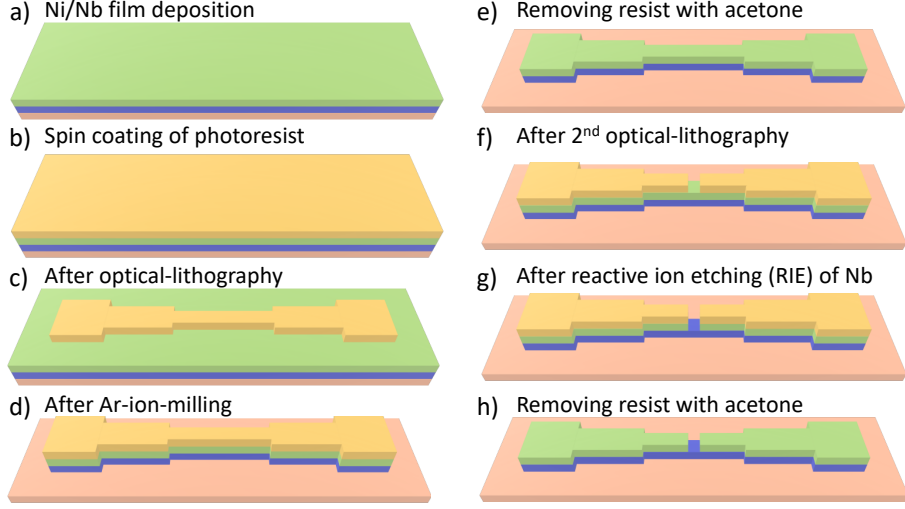


Figure 3.1: Steps followed during the fabrication of a Nb/Ni/Nb planar structure.

3.2.3 Justification of sample geometry

In Fig. 3.2(a), we have shown a Nb/Ni/Nb planar structure, where the gap between the two Nb electrodes is $3 \mu\text{m}$. The gap between the two Nb electrodes is well beyond the singlet pair coherence length of Ni ($\xi_{Ni} \sim 4 \text{ nm}$) [42]. Therefore, any possibility of Josephson coupling is excluded in this geometry. In Fig. 3.2(b), we show the region near the gap along with a schematic of the Bloch domain wall of Ni, to emphasize the magnetic non-collinearity. Multiple domain walls (present at the boundary of two magnetic domains represented in red and blue color) are present in the ferromagnet (Ni), as confirmed from the Kerr microscopy in chapter 2. The singlet Cooper-pairs are injected into these DWs and, subsequent effects have been studied in this chapter.

In Fig. 3.3, we show the $R(T)$ measurements for patterned Ni/Nb bilayer stripe without any gap in the Nb layer. We observe that the current in Nb completely bypasses the Ni layer for temperatures below T_c and the resistance is almost zero. The presence of a gap in Fig. 3.2(b) should promote the diffusion of Cooper pairs from Nb to Ni. Indeed, we found that the geometrical gap enhances the diffusion of Cooper pairs far beyond the position of the gap. Fig. 3.4 shows

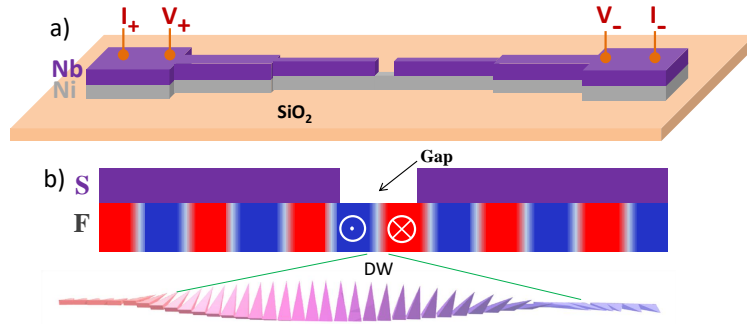


Figure 3.2: (a) Schematic illustration of Nb/Ni/Nb planar structure in four-probe geometry. The gap between two Nb electrodes is $\sim 3 \mu\text{m}$, (b) Cross-sectional view of the region near the gap, a Bloch domain wall exists at the interface of two magnetic domains represented by red and blue color (oriented oppositely), the schematic of a Bloch domain wall at the bottom emphasize the magnetic non-collinearity needed for singlet-triplet conversion.

the residual resistance of Nb/Ni/Nb planar structure below T_c for three different separations between voltage contacts (varying from 1 mm to 1.5 mm), but with a fixed separation between current contacts. We observe a larger resistance for a larger separation (d_1) between the voltage contacts.

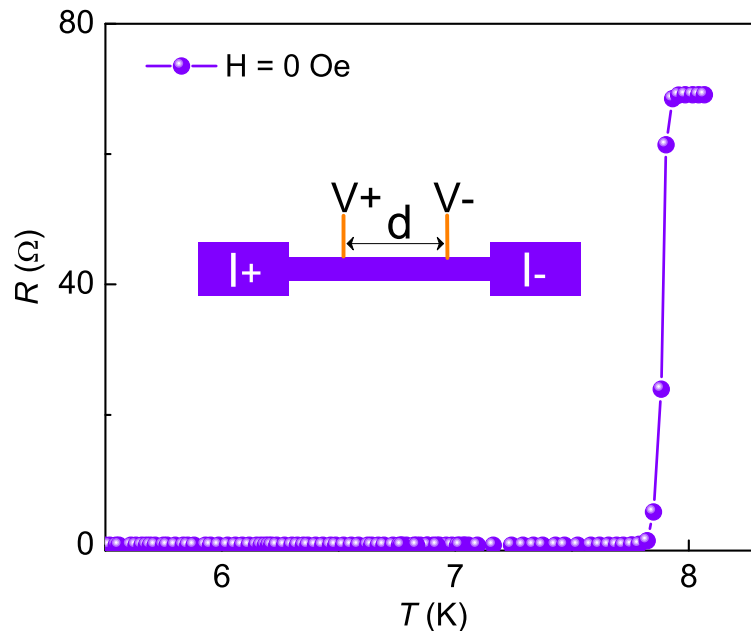


Figure 3.3: $R(T)$ curve for a Ni/Nb bilayer stripe (without any gap in Nb layer) at zero magnetic field. Inset shows the schematic of the top view of the sample. Superconducting transition temperature, $T_c = 8.5 \text{ K}$

One of the possible explanations for the observed effect may be the charge

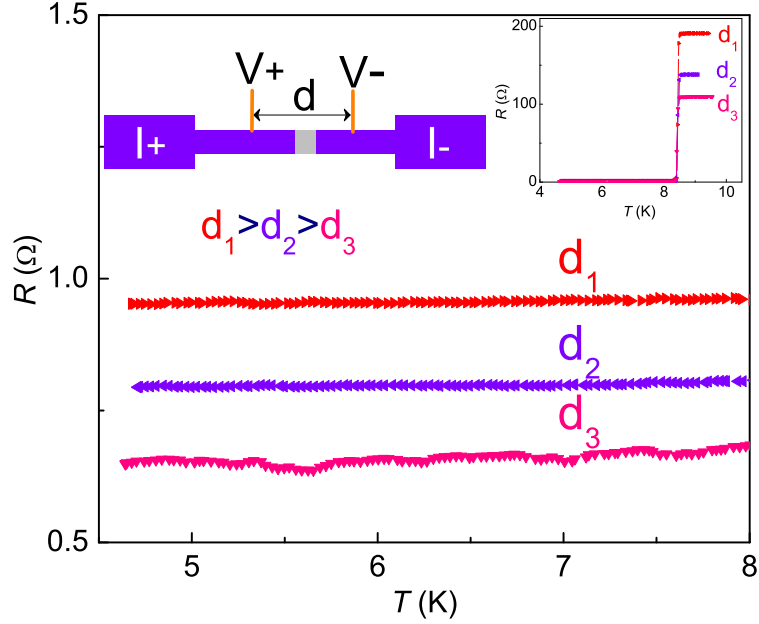


Figure 3.4: $R(T)$ curves for Nb/Ni/Nb planar structure at three separations (d_1 , d_2 , d_3) between voltage contacts but fixed distance between the current contacts, the resistance is higher for larger separation (d_1) indicating the diffusion of Cooper-pairs from Nb to Ni beyond the gap region, Inset shows the schematic illustration of the top view of the sample in a four-probe geometry. Another inset shows the T_c for all the three cases, which was 8.5 K.

imbalance effects, a non-equilibrium phenomenon. Charge imbalance occurs when the quasi-particles in a normal metal (N) transform to Cooper-pairs in S. From previous reports [107,108], in systems having charge imbalance, an increase in resistance is expected below T_c , unlike the case here. Hence, in the present experimental geometry, the possibility of having a charge imbalance is excluded. The other explanation for the increased resistance with increased distance between voltage contacts is that the Ni film present outside the gap region also contributes to resistance. This implies the diffusion of Cooper-pairs from Nb to the Ni layer beyond the gap region.

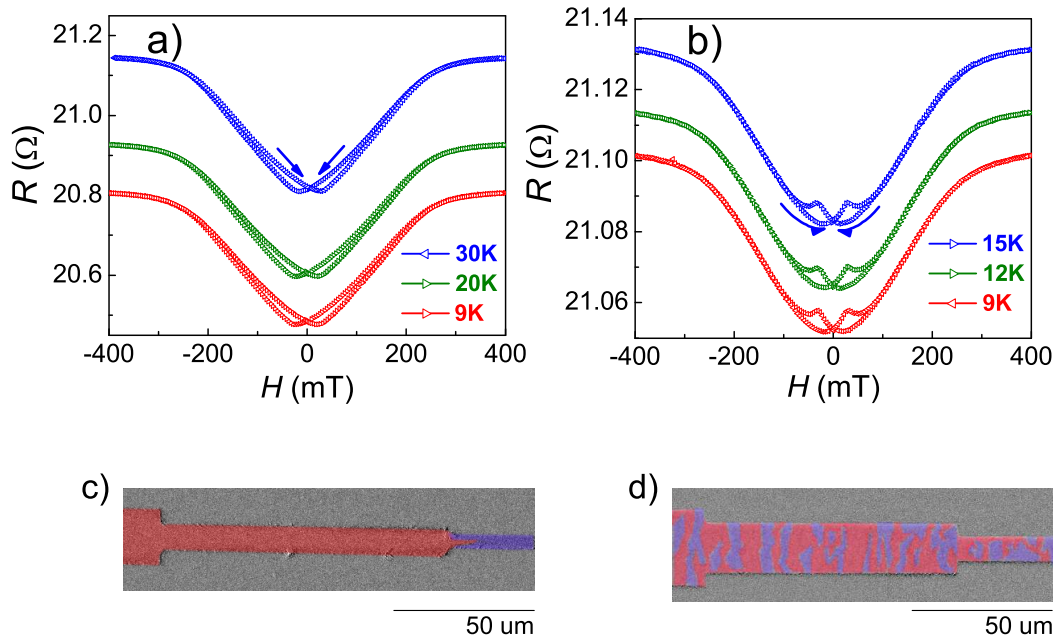


Figure 3.5: DWMR of Nb/Ni/Nb planar structures at $T > T_c$, (a) $R(H)$ curves for parallel field configuration, showing the intrinsic MR of Ni, (b) $R(H)$ curves for transverse field configuration, showing DWMR peaks along with intrinsic MR of Ni. DWMR remains the same for temperatures above T_c , (c) Longitudinal Kerr micrograph for parallel configuration, showing the propagation of a domain wall, (d) Longitudinal Kerr micrograph for transverse configuration, showing multiple DWs during magnetization reversal. Kerr micrographs are recorded at room temperature. Red color and blue color represent domains oriented in opposite direction.

3.3 Results and Discussions

3.3.1 DWMR of Ni/Nb stripes above superconducting transition

Fig. 3.5 shows the $R(H)$ curve of Nb/Ni/Nb planar structure for $T > T_c$. The $R(H)$ curves shown in Fig. 3.5 are for a sample different from the one shown in Fig. 3.4. Fig. 3.5(a) shows the $R(H)$ for magnetic field applied along the length of the stripe (parallel configuration). Fig. 3.4(b) shows the $R(H)$ for the magnetic field applied along the width of the stripe (transverse configuration). This is to be noted that the magnetic field is always applied in the plane of the film. Therefore, we will refer to these two field configurations as parallel and transverse field configuration, respectively. For parallel configuration, we observe the usual magneto-resistance (MR) of Ni, as shown in Fig. 3.5(a). The general behavior was the same for all temperatures up to 30 K, due to a high Curie temperature (T_{curie}) [42] of Ni. In transverse configuration, we observe additional peaks in MR at H_c , termed as DWMR, as shown in Fig. 3.5(b). We find that the DWMR peak amplitude is the same for all temperatures up to 15 K. We further note that these MR peaks appear at H_c which corresponds to the MR minima in parallel configuration shown in Fig. 3.5(a). Usually, the number of domain walls reaches a maximum at H_c in a ferromagnetic film [116]. Therefore, we can correlate the origin of MR peaks in Fig. 3.5(b) to the number of domain walls. We verified this fact using Kerr microscopy of Ni stripes in parallel and transverse field configuration. We observe two domain walls in parallel configuration near H_c , as shown in Fig. 3.5(c). In transverse configuration, we observe a large number of domain walls near H_c , as shown in Fig. 3.5(d). The addition of DWMR contributions of these DWs gives the observed DWMR peak, as shown in Fig. 3.5(b). In parallel configuration, no DWMR peaks were observed due to very low domain wall density, as shown in Fig. 3.5(c). DWMR peaks in transverse configuration ensure that the bias current

crosses a significant number of DWs. Therefore, a large number of diffused singlet pairs may encounter a domain wall directly at temperatures below T_c . For this reason, the transverse configuration is the appropriate measurement geometry to study the effect of Cooper-pair diffusion on DWMR at temperatures below T_c .

3.3.2 DWMR of Ni/Nb stripes below superconducting transition

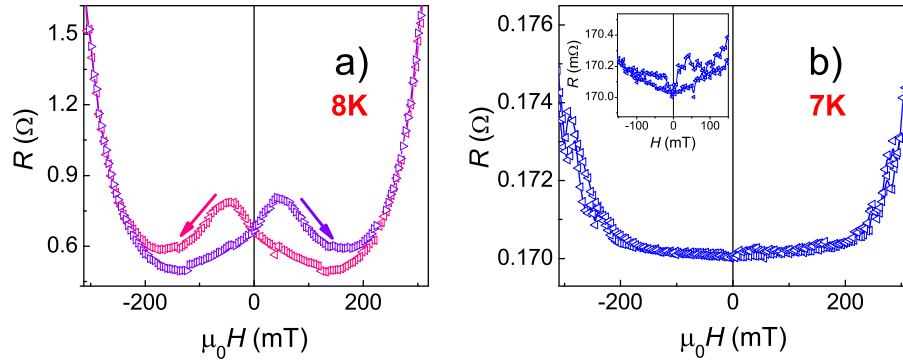


Figure 3.6: DWMR of Nb/Ni/Nb planar structures at $T < T_c$. (a) The $R(H)$ curves at 8K follows the $M(H)$ loop of Ni film. $T = 8\text{K}$ is very close to $T_c = 8.3\text{ K}$ and therefore, sensitive to DW stray fields. (b) The $R(H)$ curves at 7K indicates that superconductivity of Nb is no more affected by the stray fields of DWs.

Fig. 3.6 shows the $R(H)$ curves of Nb/Ni/Nb planar structure below T_c in transverse configuration. In Fig. 3.6(a), we show the $R(H)$ curve at 8K. We observe two distinct MR peaks at H_c and their amplitudes exceed 50 times of the normal state DWMR ($\sim 5.9\text{ m}\Omega$) [Fig. 3.5(b)]. At 8K (close to $T_c \sim 8.3\text{ K}$), Nb is very sensitive to the stray field of DWs. As a result, the superconductivity is suppressed giving rise to MR peaks with maxima at H_c , as reported earlier [103]. At lower temperatures, the superconducting state is relatively less prone to DW stray field of Ni. Stray field effects (MR peaks) should, therefore, be suppressed at lower temperatures. We observe the same in the $R(H)$ curve at 7 K [Fig. 3.6(b)]. However, a DWMR with amplitude of $\sim 0.2\text{ m}\Omega$ was observed at 7K [inset of Fig. 3.6(b)].

In Fig. 3.7(a) and (b), $R(H)$ curves at 6 K are shown with the magnetic field

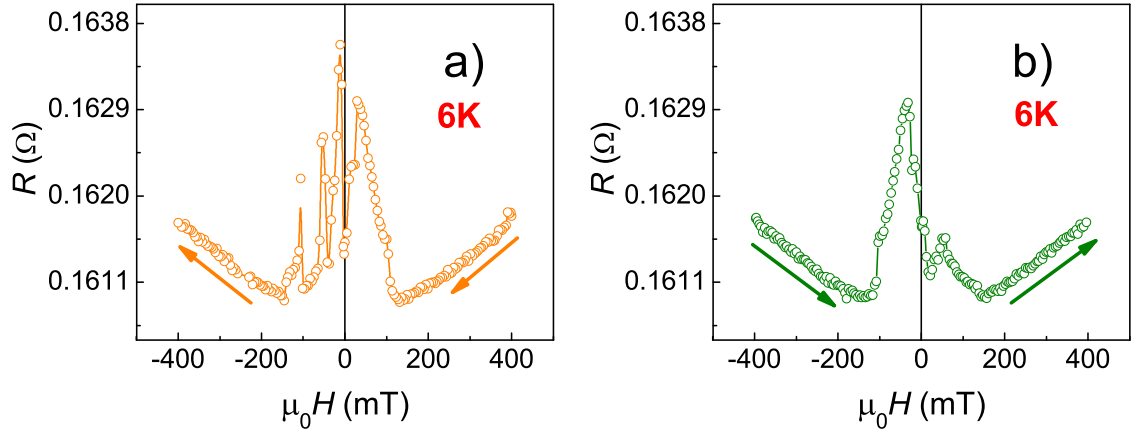


Figure 3.7: (a) The $R(H)$ curves at 6K for field sweep direction from positive to negative saturation field, showing a decrease in resistance at positive field. (b) The $R(H)$ curves at 6K for field sweep direction from negative to positive saturation field, showing a decrease in resistance at negative field.

swept in backward (+ve to -ve field) and forward (-ve to +ve field) directions, respectively. As shown in Fig. 3.6(b), DW stray fields no longer affect the Nb at temperatures ≤ 7 K. Therefore, it was possible to observe the DWMR peaks, which is a much smaller effect. However, we observe that the nature of the DWMR peaks is significantly different than the corresponding DWMR peaks in the normal state. For temperatures above T_c , in the forward (backward) magnetic field sweep, maxima in DWMR appeared at the positive (negative) H_c [Fig. 3.5(b)]. However, in Fig. 3.7(a) and (b), DWMR peak appeared on the opposite side, i.e. for forward (backward) sweep of magnetic field, peak in DWMR appears in the negative (positive) field. As the domain activity starts, while sweeping the field from saturation value, the DWMR effects start to appear, as shown in Fig. 3.7(a). However, the increase in resistance is curtailed at a field value lower than H_c where the number of domain walls reaches a maximum. Similar features were observed in Fig. 3.7(b) while sweeping the field from negative to positive saturation field. We also observed some sharp spike-like features in Fig. 3.7(a). Following previous reports [103], these sharp spikes in $R(H)$ curve at 6 K may be expected due to an abrupt re-arrangement of vortices. In addition, we observe an increase in

DWMR at 6 K compared to that at 7 K. From earlier report on Nb/Garnet bilayer, superconductivity shrinks the domains for temperatures below T_c [117]. Therefore, this increase in DWMR below 7 K may be explained from the increased number of domain walls, as reported earlier [117]. However, the domain structure remains the same with a decrease in temperature. Therefore, it is not possible to explain the unconventional drop in MR at 6 K in terms of the variation of domain structure. This can also not be explained due to S/F proximity effects, which is present at all values of the magnetic field in the R(H) curve. One can study the Ni/Nb interface proximity effects by studying the conductance-voltage characteristics [118,119] but this is beyond the scope of the present work. This work is focused on the changes of DWMR due to Cooper-pair injection into the domain walls of Ni.

Discussion

This unconventional decrease in DWMR may be explained from singlet-triplet conversion process through intrinsic domain walls of Ni. To explain this, we show the schematic of different resistances seen by the bias current for temperatures above and below T_c , in Fig. 3.8. For temperatures above T_c , the total current splits in two branches and carried by Nb (I_{Nb}) and Ni (I_{Ni}) layers in parallel according to their resistances. I_{Ni} encounters many DWs in the path. Therefore, the effective resistance seen by I_{Ni} can be written as a sum of the resistance of Ni domains, (R_D) and DWs, (R_{DW}). Theoretically, an injected current through the DWs causes spin accumulation and hence DWMR, as shown in Fig. 3.5(b) [85].

For $T < T_c$, resistances of the Nb electrodes, R_{Nb} becomes zero. It is probable that some singlet pairs may diffuse into the DWs and may transform into the triplet pairs [8,104,105]. The spin-diffusion length (L_{sf}) of Ni is $\sim 21 \pm 2$ nm [120], which may limit the decay length of triplet pairs beyond L_{sf} [121]. The triplet pairs do not cause any spin accumulation. Therefore, an effective drop in resistance

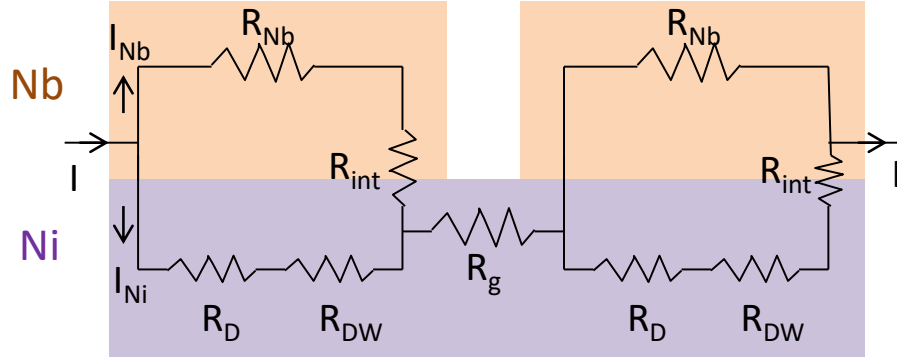


Figure 3.8: Schematic parallel resistance model. The total current I flows in parallel through Nb (I_{Nb}) and Ni (I_{Ni}) for $T > T_c$. For $T < T_c$, $R_{Nb} = 0$ and the total resistance becomes an addition of (i) magnetic domain resistance R_D , (ii) DW resistance R_{DW} , (iii) Ni/Nb Interface resistance R_{Int} , and (iv) Resistance of Ni present in gap region R_g .

is expected on the appearance of triplet pairs, as shown in Fig. 3.7(a) and (b). The singlet pairs entering the domains will become normal electrons due to very low coherence length $\xi_{Ni} \sim 4$ nm [42]. These normal electrons constitute the normal current and give rise to DWMR.

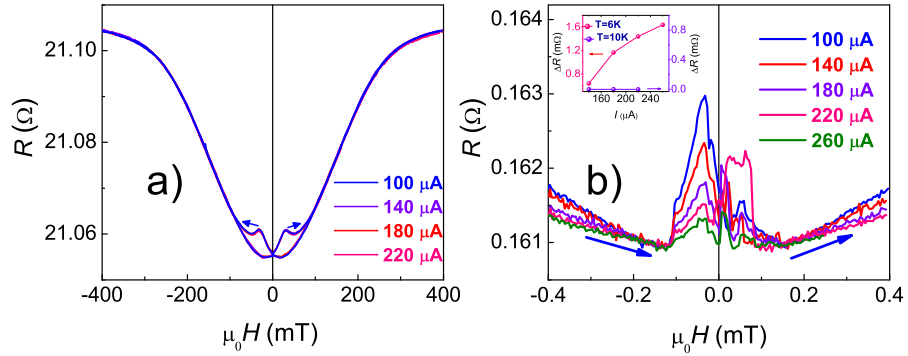


Figure 3.9: Current dependent DWMR for temperature above and below T_c . (a) $R(H)$ curves at 10 K for different bias currents showing DWMR remains the same for all bias currents. (b) $R(H)$ curves at 6 K for different bias currents showing DWMR decreases with increasing bias currents. Inset shows the difference of DWMR peak amplitude for particular bias current w.r.t. that at $100 \mu A$, defined as ΔR_{6K} and ΔR_{10K} for 6K and 10K.

We performed magneto-transport measurements for different bias currents for temperatures above and below T_c shown in Fig. 3.9. We have shifted the curves along the y-axis to compare the DWMR peaks at all bias currents. For a temperature

of 10 K (Fig. 3.9(a)), the DWMR was found to be the same for all bias currents, as expected [85]. However, at 6K, a decrease in DWMR was observed with an increase in bias current [Fig. 3.9(b)]. Inset shows ΔR_{6K} and ΔR_{10K} vs bias current. ΔR_{6K} and ΔR_{10K} have been defined as the difference of DWMR peak amplitude for a particular bias current w.r.t. that at 100 μ A for 6 K and 10 K, respectively. ΔR_{10K} remains 0 for all bias currents which essentially means that the DWMR peak amplitude remains the same for all bias currents at 10 K. However, we observe an increase in ΔR_{6K} , as we increase the bias current. This means a decrease in DWMR peak with increasing bias currents. The decrease in DWMR peak amplitude may be explained from the fact that the increase in bias current leads to an increase in the total number of Cooper pairs. Therefore, the number of Cooper pairs injected into DWs should increase leading to enhanced triplet correlations after crossing the DWs. This may give an effective singlet-triplet conversion process. Higher bias current will result in a higher number of singlet pairs. Therefore, the number of Cooper-pairs entering the Ni domains will increase which eventually converts into normal electrons. However, the DWMR peak amplitude remains the same irrespective of the number of normal electrons passing through Ni, as shown in Fig. 3.9(a). Therefore, the DWMR is unaffected by the increase in the number of singlet pairs of Nb and the normal electrons of Ni. So, the only possible reason for the change in DWMR of Fig. 3.9(b) may be the singlet-triplet conversion process through DWs. This further supports our interpretation of DW induced triplet pairs in Nb/Ni/Nb planar structure.

In an earlier report [110], similar anomalous features have been observed in MR of Nb/BaFe₁₂O₁₉ bilayers where the dips in MR have been ascribed to onset of DW superconductivity. However, these measurements were done at temperatures very close to T_c , where the stray fields of domain and DWs can affect superconductivity significantly. This possibility is excluded in our experiment because, in our data, the effect of the stray field of DWs is minimized below 7 K, as shown in

Fig.3.6(b). Also, the observed anomalous features of DWMR can not be explained by S/F proximity effects which are field independent, unlike the case here. Another possible explanation for this anomalous decrease in DWMR may be the vortex locking-unlocking effects [122]. With an increase in bias current, there will be an increase in the Lorentz force on any possible vortices in Nb. Therefore, the field values corresponding to the drop in DWMR should be different for different bias currents, unlike Fig. 3.6(b). Therefore, this possibility is also excluded. In light of the above discussion, the singlet-triplet conversion of DWs seems to be the most probable reason for the observed unconventional decrease in DWMR.

3.4 Conclusion

We have investigated DWMR for temperatures above and below T_c of Nb in a Nb/Ni/Nb planar structure. For temperatures above T_c , we observed DWMR peaks at H_c , where the number of domain walls reaches a maximum, as verified using longitudinal Kerr microscopy. For temperatures below T_c , we observed an unconventional drop in DWMR. In a patterned Ni/Nb stripe geometry, by carving a microscopic gap in the Nb layer, we have been able to inject singlet Cooper pairs into Ni. Also, it is possible to measure the DWMR of Ni in this geometry, for temperatures below T_c . However, in an S/F bilayer used in earlier reports, the current is mostly shunted by the superconducting layers and, therefore, the DWMR property of intrinsic domain walls would not be possible to measure. We have interpreted the unconventional drop in resistance of the Ni stripe (below T_c) in terms of singlet-triplet conversion through the intrinsic DWs of Ni. We have excluded other phenomenon leading to a similar drop in DWMR, including DW superconductivity, vortex locking-unlocking effects and S/F proximity effect.

Chapter 4

Intrinsic domain wall induced triplet supercurrents in Nb/Ni/Nb planar Josephson junction and DC-SQUID

4.1 Introduction

We have seen in the previous chapter that diffusion of singlet Cooper pairs into domain walls of ferromagnet leads to a decrease in the DWMR, in a Nb/Ni/Nb planar structure. This observation was discussed as a signature of singlet-triplet conversion by natural DWs. Measurement of DWMR is, however, an indirect probe of singlet-triplet conversion through DWs. A more direct study would be to measure current across an S/F/S planar Josephson junction where a DW is pinned at the barrier. If a barrier width of the order of DW width can be achieved, then a triplet supercurrent should be measurable across the S/F/S planar junction.

In this chapter, we have used a constricted Ni stripe to pin a single domain wall of Ni at the constriction. Nb electrodes close to the constriction formed a Nb/Ni/Nb planar junction. We have fabricated such Nb/Ni/Nb planar Josephson junctions using FIB patterning, where a gap of width ~ 70 nm was achieved between

two Nb electrodes over the constricted area. Using micro-magnetic simulations, we found that in our experimental geometry, a domain wall remains pinned at the constriction for out-of-plane magnetic fields. From the transport measurements, we found a supercurrent in the junction. The supercurrent exists over a Ni barrier width of ~ 70 nm, which is much greater than the singlet pair coherence length ($\xi_{Ni} \sim 4$ nm) [42] of Ni. Josephson coupling in this planar junction geometry was confirmed via magnetic field dependence of critical current ($I_c(H)$), which showed a characteristic Fraunhofer pattern. Both of these observations confirmed the long-range triplet Josephson coupling in these junctions. We further fabricated DC-SQUID devices (with two Josephson junctions in a superconducting loop) using the same concept of pinning a domain wall in a planar Nb/Ni/Nb junction geometry. These devices showed characteristic flux modulations of voltage at a fixed bias current, confirming SQUID operation.

4.2 Experimental Details:

4.2.1 Film Growth.

Thin film bilayers of Ni(110 nm)/Nb(65 nm) stack were prepared at room temperature at an Ar pressure of 1.5 Pa, using DC-magnetron sputtering of high purity (99.99%) Nb and Ni targets on thermally grown Si/SiO₂ substrates. The base pressure of the deposition system was of the order of 10^{-9} mBar. Substrates were rotated under the sputtering plasma during the deposition, which ensured uniform deposition across the substrate. Film thicknesses were controlled by the speed of rotation of substrate plate under the sputtering plasma and were calibrated using X-ray reflectivity (XRR).

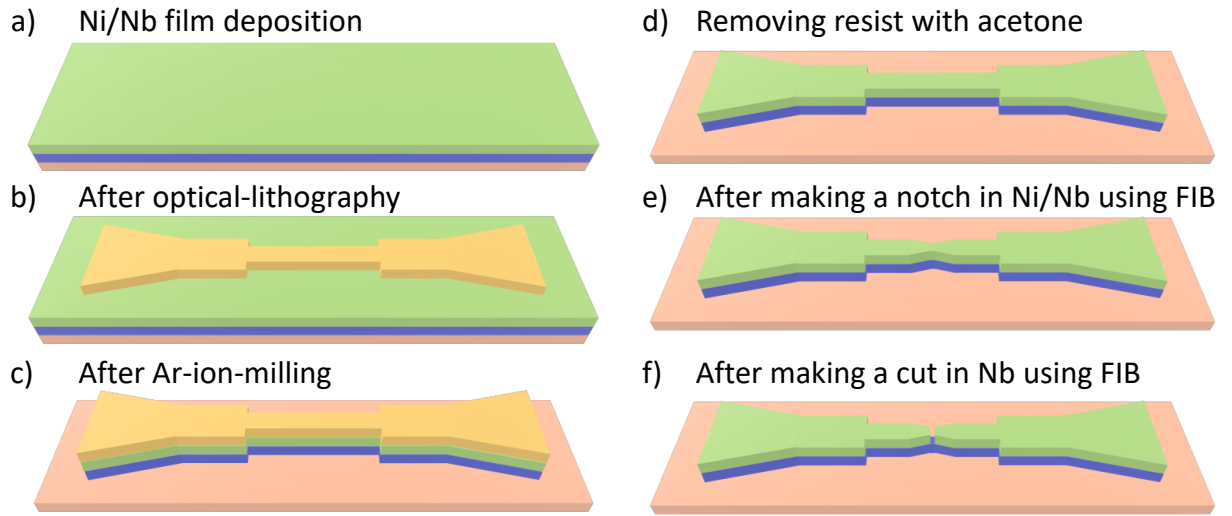


Figure 4.1: Steps followed during the fabrication of a Nb/Ni/Nb planar Josephson junction.

4.2.2 Device Fabrication.

Individual Nb/Ni/Nb planar Josephson junctions were fabricated from the Ni/Nb bilayer films in a three-step process. In the first step, Ni/Nb bilayer films were patterned in the form of a stripe with $6 \mu\text{m}$ width using optical-lithography and Ar-ion-milling, as shown in Fig. 4.1(a), (b), and (c). In the second step, triangular cuts were made in the central part of the stripe to define a notch using Ga-ion based Focused Ion Beam (FIB) milling, as shown in Fig. 4.1(e). A wide gap of $\sim 70 \text{ nm}$ was created in the top Nb layer, on the constricted region in the third step, as shown in Fig. 4.1(f). The dimensions of the Nb/Ni/Nb planar junction made in this way were $(70 \times 85) \text{ nm}^2$. The gap ($\sim 70 \text{ nm}$) between the two Nb electrodes is well beyond the singlet Cooper pair coherence length of Ni ($\sim 4 \text{ nm}$) [42]. Therefore, any Josephson coupling between the two Nb electrodes is possible only through triplet supercurrents. Fig. 4.2(a) shows the schematic illustration of the top view of Nb/Ni/Nb Josephson junction in a four-probe geometry. Fig. 4.2(b) shows the FESEM micrograph of the area near the gap region. The absence of Nb in the gap region was confirmed using energy dispersive spectroscopy (EDS), as shown

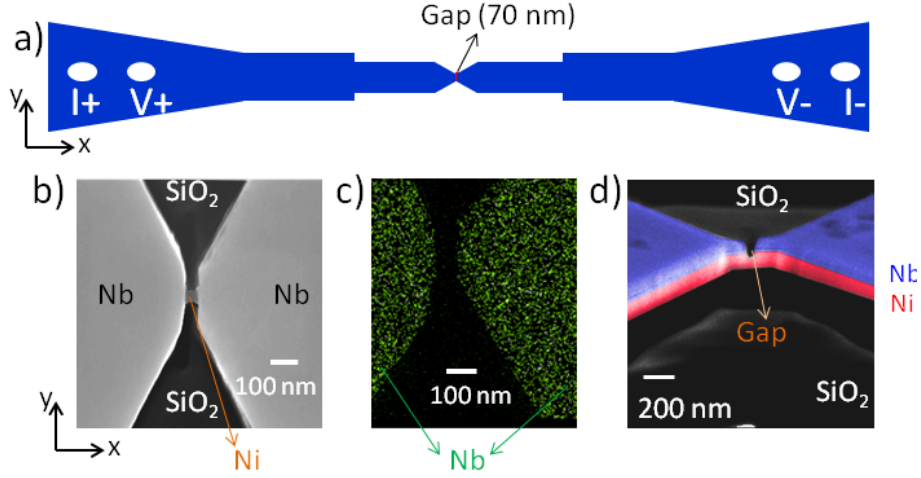


Figure 4.2: (a) Schematic illustration of Josephson junction showing triangular notch in the central stripe with $6 \mu\text{m}$ width. (b) FESEM image showing the top view of the junction. A gap of dimension $70 \times 85 \text{ nm}^2$ was carved in the Nb layer over the notch area. (c) Energy Dispersive Spectroscopy (EDS) image showing the absence of Nb in the gap region, Green color represents the presence of Nb. (d) False color FESEM image showing the cross-sectional view of the junction. The depth of the cut is beyond the Nb layer, confirming the absence of Nb in the gap.

in Fig. 4.2(c). Energy dispersive spectroscopy is a technique used for identifying the elements present in a sample. When a high energy electron beam is incident on the material, characteristic X-rays are emitted. The elements in a sample are identified by measuring the energy spectrum of these X-rays. The green color in the EDS image represents the Nb. Fig. 4.2(d) shows the oblique view of the gap region of Nb, confirming the depth of the cut beyond the Nb layer.

4.2.3 Micro-magnetic OOMMF simulations.

To assess the domain structures for an in-plane and out-of-plane magnetic fields in our sample geometry, we performed micro-magnetic 3D OOMMF simulations for Ni stripe using the NIST mif code [36]. Fig. 4.3(a) and Fig. 4.3(b) show the OOMMF simulation images for in-plane and out-of-plane magnetic fields. These images correspond to the remanence state, obtained by sweeping the field from saturation (400 mT) to zero field. For the simulations, the values of exchange constant and saturation magnetization were taken from the literature [123] as 9×10^{-12}

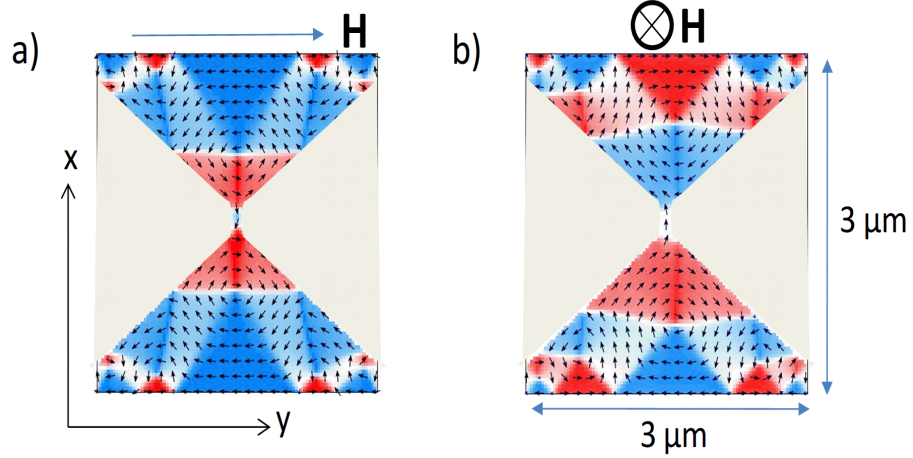


Figure 4.3: (a) micro-magnetic 3D OOMMF simulation image at remanence state for an in-plane applied magnetic field. Red and blue color represents moments oriented in opposite directions, white color represents a domain wall which separates two magnetic domains represented by red and blue color. (b) micro-magnetic simulation image at remanence state for out-of-plane magnetic field configuration. A domain wall is pinned at the notch area.

J/m and $4.9 \times 10^5 \text{ A/m}$, respectively. The x , y and z dimensions of the samples were kept fixed as $3 \mu\text{m}$, $3 \mu\text{m}$ and 90 nm , respectively. In the simulation, x -axis is along the length, y -axis is along the width and z -axis is along the thickness (perpendicular to the sample plane) of Ni stripes. The cell size for the simulation was kept as $(10, 10, 10) \text{ nm}^3$ in (x, y, z) directions. Magnetic field was directed along the y -axis and z -axis of the stripe for Fig. 4.3(a) and Fig. 4.3(b), respectively. We observe oppositely oriented (red and blue color) magnetic domains around the notch in Fig. 4.3(b), while the red color domains are present on both the sides of the notch in Fig. 4.3(a). Therefore, a single, well defined, domain wall (white color separating the red and blue domains) is present in the notch in Fig. 4.3(b), which makes it a suitable measurement geometry for this experiment.

4.2.4 Transport measurements.

Junction measurements were performed in a commercial cryogen-free cryostat system. Devices were wire-bonded in four-probe geometry on chip carriers for transport

measurements. Current-voltage (I - V) curves were measured in a four-probe current-biased configuration for different in-plane applied magnetic fields. The distance between the voltage contacts was more than 2 mm. The temperature stability during the measurement was ± 3 mK.

4.3 Results and Discussion

4.3.1 Nb/Ni/Nb planar Josephson junction characteristics

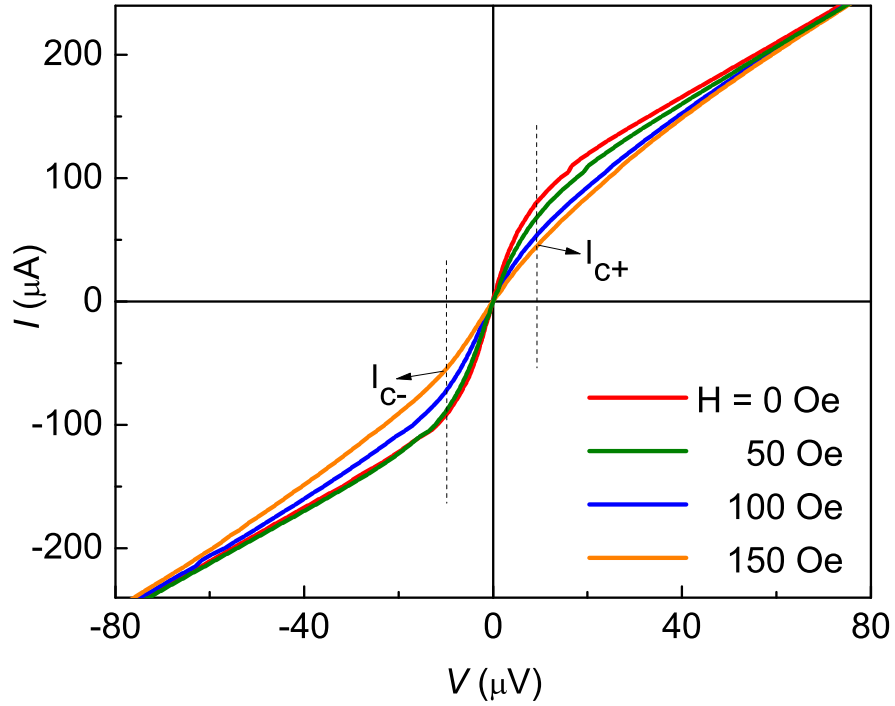


Figure 4.4: I - V characteristics at $H = 0$ Oe, 50 Oe, 100 Oe, 150 Oe and $T = 2$ K for out-of-plane field configuration.

In Fig. 4.4, we show the I - V measurements for out-of-plane field configuration at magnetic field values of 0 Oe, 50 Oe, 100 Oe, and 150 Oe. A supercurrent was observed in this junction despite the large gap (~ 70 nm) between the Nb electrodes. We note that the I - V curves have a tilt about the zero voltage line. Due to a large distance between the voltage contacts (> 2 mm), Ni/Nb interface resistance adds to the I - V curves and leads to the observed tilt. We also mention

here that such a tilt in I - V curves has been seen in earlier reports on planar Josephson junctions [124]. Critical current I_c was defined as the average of I_{c+} and I_{c-} , where I_{c+} and I_{c-} are the current values corresponding to voltage values of $5 \mu\text{V}$ and $-5 \mu\text{V}$, respectively, as shown by the dashed lines in Fig. 4.4.

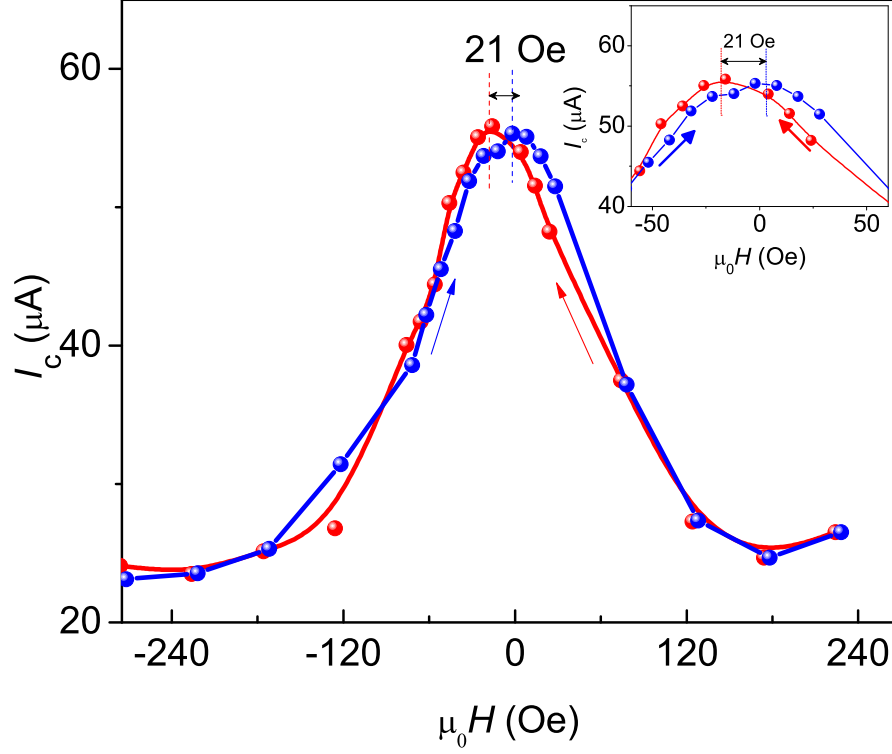


Figure 4.5: Magnetic field dependence of I_c of Nb/Ni/Nb Josephson junction at 2 K for out-of-plane magnetic fields. The inset shows the hysteresis of low field $I_c(H)$ due to internal barrier flux of Ni.

In Fig. 4.5, we show the out-of-plane $I_c(H)$ behavior of Nb/Ni/Nb planar Josephson junction at 2K. The maxima in I_c are offset from $H = 0$ to ± 10 Oe due to intrinsic barrier flux from the barrier magnetization. The inset of Fig. 4.5 shows the low field regime of the $I_c(H)$ curve, emphasizing this shift. The shift in central peak in I_c with field sweep direction is due to the changing magnetization of the barrier and is a characteristic feature of a magnetic Josephson junction. The $I_c(H)$ behavior confirms that the barrier in our Nb/Ni/Nb junction is magnetic in nature.

Discussion

Figure 4.6 shows the comparison of $R(T)$ curves for the unconditioned and

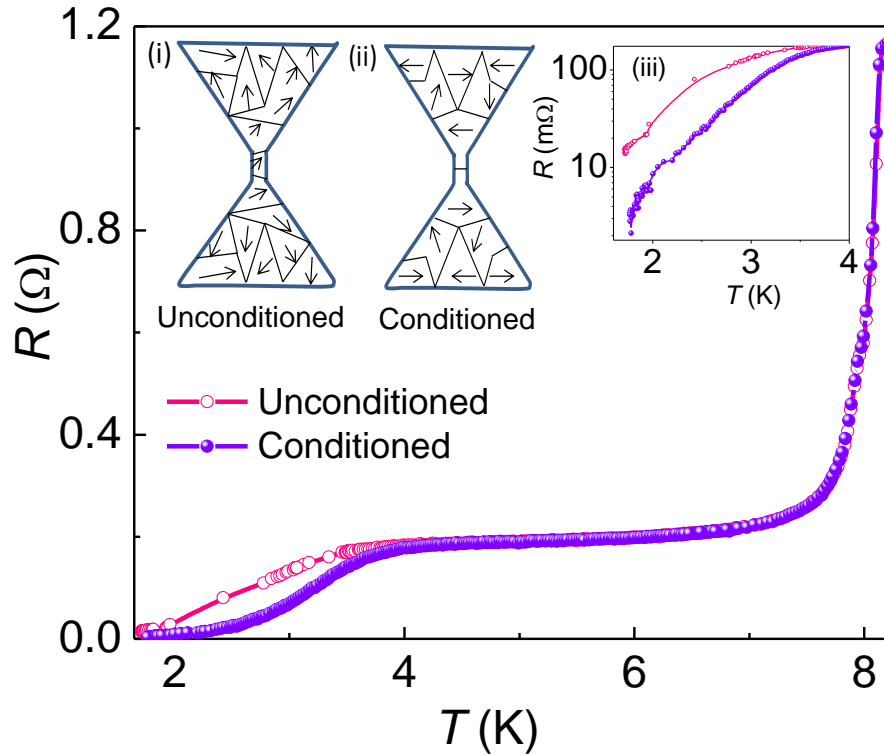


Figure 4.6: $R(T)$ curves at bias current of $10 \mu\text{A}$ for unconditioned and conditioned state. The unconditioned state corresponds to the demagnetized state with random domain structures represented by the black arrows in inset(i). The conditioned state shown in inset (ii) corresponds to remanence, where two oppositely oriented domains are present around the notch and a well defined domain wall is present inside the notch, following the OOMMF simulations of Fig. 4.3(b). Inset (iii) presents the $R(T)$ curve at lower temperature on a logarithmic scale for a clear comparison of the two situations.

conditioned state in out-of-plane field configuration. In the unconditioned state, the sample was cooled in the absence of field and $R(T)$ curve was measured during the heating in zero field. For magnetic conditioning of the sample, the film was subjected to a field of 400 mT at 10 K and brought back to zero field at the same temperature. This state corresponds to remanence and a domain wall is pinned in this state, as shown in Fig. 4.3(b). The sample was then cooled in the zero-field condition down to 2 K. Resistance as a function of temperature was

recorded during the heating. We note that the resistance value at 2K reduced from 17 $m\Omega$ in the unconditioned state to 5 $m\Omega$ in the conditioned state, as shown in Fig. 4.6. The reduction in resistance value at low temperature is an evidence of increased superconductivity in the gap region due to the presence of a pinned domain wall as observed in simulation results shown in Fig. 4.3(b). The singlet pairs may convert to triplet pairs on passing through the inhomogeneous structure of Bloch domain wall, as predicted theoretically [8]. In the unconditioned state, random domain structures are present in the gap region. Therefore, it is expected to observe a higher residual resistance. The reduction in resistance from unconditioned to conditioned state is strong evidence of the singlet-triplet conversion through pinned domain wall in Nb/Ni/Nb junction. In Nb/Ni/Nb planar junctions, the supercurrents are observed over a range of ~ 70 nm which is beyond the known singlet coherence length in Ni of $\xi_{Ni} \sim 4$ nm [42]. The long-range nature of supercurrents indicates that the transport of supercurrents is via triplet pairs due to the inhomogeneous structure of pinned domain wall.

4.3.2 Domain wall junction based DC-SQUID characteristics

Using the concept of intrinsic domain wall based triplet Josephson junctions, we have fabricated Nb/Ni/Nb planar SQUID loop, as shown in the schematic of Fig. 4.7(a), using the same notched geometry. A square loop with dimensions $\sim 1 \times 1 \mu\text{m}^2$ was made in the central Ni/Nb bilayer stripe of width 6 μm . We obtain two Ni/Nb stripes of width 1 μm in parallel with each other, as shown in the schematic of Fig. 4.7(a). We made triangular notches in the two parallel stripes. Two wide gaps, each of ~ 70 nm were created over the triangular notches, as shown in the top view of the sample from the FESEM image of Fig. 4.7(b). Thus, we obtain two planar Josephson junctions with barrier dimensions of $(\sim 70 \times 85) \text{ nm}^2$, which are connected through a superconducting loop of area $\sim 1 \times 1 \mu\text{m}^2$. The large gap ($\sim 70 \text{ nm} \gg \xi_{Ni}$) between superconducting electrodes in each junction ensures

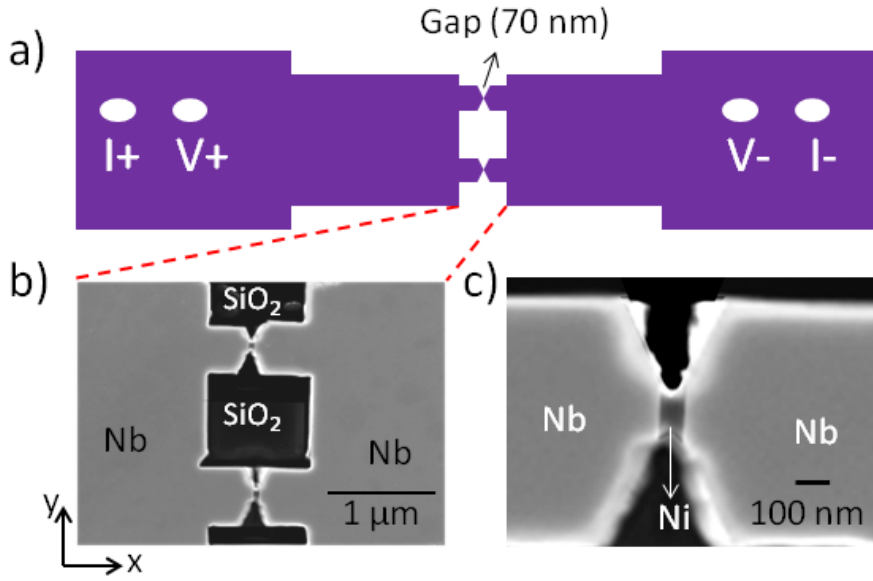


Figure 4.7: (a) Schematic illustration of Josephson junction SQUID showing two triangular notches in the central stripe. (b) FESEM image showing the top view of the DC-SQUID. A gap of dimension $70 \times 85 \text{ nm}^2$ was carved in the Nb layer over the two notches. (c) Zoomed view of a single notch showing the Nb electrodes and Ni present in the gap region.

that the SQUID action of this device is possible only through triplet Cooper pairs. Fig. 4.7(c) shows the zoomed view of a single junction clearly separating the Nb electrodes and the Ni barrier in the gap region.

Similar to the case of a single notch in a Ni stripe, we have performed 3D OOMMF simulations for the two notches in a Ni loop. Fig. 4.8(a) shows the simulation image of Ni loop at remanence state after applying a saturating field (400 mT) in the out-of-plane field configuration. The x, y and z dimensions for the simulation were kept fixed as $3 \mu\text{m}$, $3 \mu\text{m}$, and 90 nm, respectively, with cell size of $(10, 10, 10) \text{ nm}^3$ in (x, y, z) directions. We observed pinned domain walls at both the notches, as shown in Fig. 4.8(a). In Fig. 4.8(b), we show the corresponding I - V measurements at 0 field (remanence state) for out-of-plane field configuration. We observe a supercurrent which is of similar order in magnitude as the single junction described in the previous section.

Figure 4.8(c) shows the flux modulations of voltage at three different bias currents

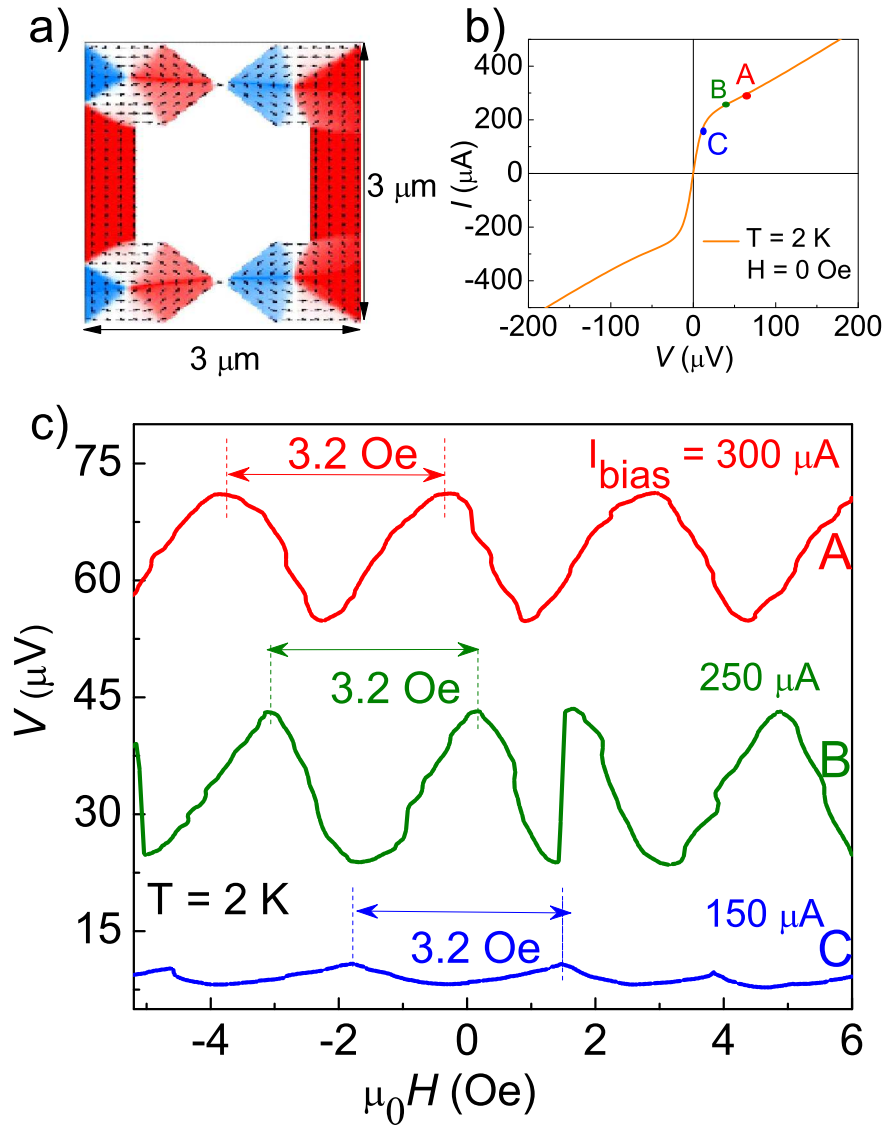


Figure 4.8: (a) micro-magnetic 3D OOMMF simulation image for an out-of-plane magnetic field configuration shows two domain walls at remanence state at the two notches in a Ni loop, remanence state is achieved by saturating the sample first to 400 mT and then reducing the field to zero. Red and blue color represent magnetic moments oriented in opposite directions, white color represents a domain wall which separates two magnetic domains represented by red and blue color. (b) I - V characteristics at $H = 0$ Oe and $T = 2$ K for in plane and out-of-plane field configuration. The $H = 0$ Oe state is achieved by saturating the sample at 400 mT and then sweeping it to zero at 10 K. (c) Flux dependent voltage modulations of Nb/Ni/Nb SQUID for three different bias currents of 300 μA, 250 μA, and 150 μA, marked as A, B and C in (b). The period of oscillation is 3.2 Oe.

of 300 μA , 250 μA , and 150 μA , marked as A, B, and C, respectively, in Fig. 4.8(b). We observe periodic modulations with a period of 3.2 Oe. This is a characteristic feature of a SQUID and confirms the SQUID coupling of this device.

Discussion

The long-range nature of the supercurrent in individual junctions confirms that the SQUID coupling is due to triplet supercurrents. Simple conversion of field period to flux quantum using only the geometrical loop area ($1 \times 1 \mu\text{m}^2$) of the SQUID results in a value of $3.2 \times 10^{-16} \text{ Tm}^2$ for the flux quantum. The difference from the actual flux quantum ($\Phi_0 = 2.07 \times 10^{-15} \text{ Tm}^2$) may be due to two reasons: First, the two Josephson junctions are connected through a Nb loop with a Ni layer underneath. The flux distribution of the underlying Ni layer may affect the calculated value of flux quantum. Secondly, the actual current distribution in the SQUID loop may be slightly different from the geometrical dimensions of $1 \times 1 \mu\text{m}^2$.

4.4 Conclusion

In conclusion, we have shown the first experimental evidence of spin-triplet supercurrent generation by intrinsic domain walls. We were able to direct the supercurrent into the ferromagnetic domain wall by pinning the domain wall at a triangular notch between two superconducting Nb electrodes. Josephson coupling is observed over a length scale of $\sim 70 \text{ nm}$ ($\gg \xi_{\text{Ni}}$) in a strong ferromagnet Ni. Two Josephson junctions made from triangular notches were connected in a superconducting loop to achieve a DC-SQUID device. We observed a SQUID coupling in this device over a length scale of $\sim 70 \text{ nm}$ ($\gg \xi_{\text{Ni}}$). This is the first demonstration of a spin-triplet SQUID through intrinsic domain walls.

Chapter 5

External field tunable superconducting transition temperature in Nb/Co/Py/Nb superconductor/exchange spring/superconductor films

5.1 Introduction

In the previous chapters, we discussed that a spin-singlet Cooper pair gets converted to a spin-triplet pair on sensing magnetic non-collinear regions at superconductor-ferromagnet interface. In this context, magnetic exchange-spring (XS) interfaces are good candidates to control the singlet-to-triplet conversion process with small magnetic fields. Magnetic exchange-spring is a combination of a hard and a soft ferromagnetic material in which the soft layer is exchange-coupled at hard/soft ferromagnet's interface in such a way that magnetization of the soft layer can rotate reversibly within a certain range of external magnetic field. Soft magnetic materials are the ones, which are easily magnetized with small magnetic fields, due to their small coercive field and low anisotropy energy. On the other hand, higher magnetic fields

are needed to magnetize and demagnetize hard magnetic materials. The magnetic field response of an XS can be tailored by varying the exchange interaction between the hard and soft magnetic layers. The combination of soft/hard magnetic layers forms an artificial domain wall structure in a certain range of magnetic field, usually known as the “spring-range”. The reversible artificial domain wall formed in XS acts as a reversible magnetic inhomogeneity to generate and tune triplet correlations in S/XS/S multilayer.

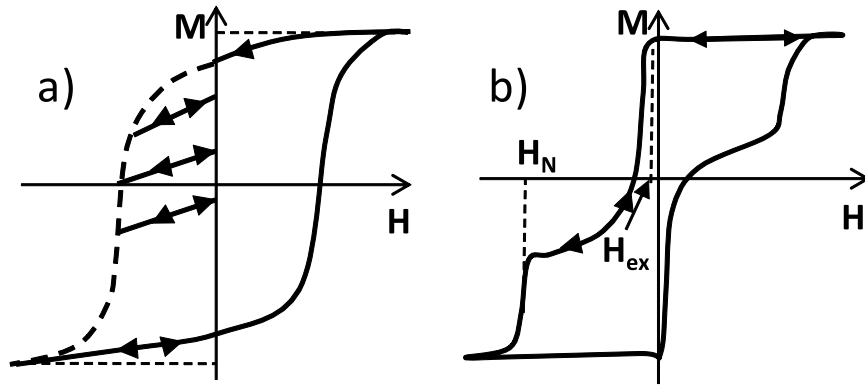


Figure 5.1: Schematic hysteresis loops of (a) Rigid hard/soft bilayer, (b) exchange-spring bilayer, the minor loops are irreversible in case of rigid hard/soft bilayer, while these loops are reversible in case of exchange-spring in a certain field range, known as spring-range. H_N denoted the nucleation field and H_{ex} denotes the exchange-field.

In Fig. 5.1, we show schematic hysteresis curves of an XS bilayer and a rigid hard/soft bilayer. The coercive field and saturation magnetization of XS changes compared to the individual components i.e. hard and soft layers. In Fig. 5.1(a), the hard and soft layers are very strongly exchange-coupled and act as a single ferromagnetic thin film. In Fig. 5.1(b), the interface exchange-coupling is relatively weak and causes the formation of a non-collinear magnetic structure in the soft layer. The twist of the non-collinear magnetic structure is reversible w.r.t. applied magnetic field up to a certain field range, known as spring range, as shown in Fig. 5.1(b). The reversible minor loop is the characteristic feature of an XS, unlike the irreversible minor loops of a rigid hard/soft bilayer shown in Fig. 5.1(a). Here, a minor loop is defined as the $M(H)$ loop, when the magnetic field sweeps from

positive saturation to a field value less than the negative saturation and then, sweeps back to a positive saturation field. The reversible non-collinear magnetic moments of an XS can be utilized to realize reversible singlet-to-triplet conversion at S/XS interface. Using this concept, several experiments have been reported in the literature. In this direction, Gu *et al.* [83] have shown an enhancement in T_c of ~ 30 mK in Nb/Py/SmFe multilayer from transport measurements. They attribute this increase in T_c to the generation of spin-triplet Cooper pairs through the non-collinear magnetic structure formed at Nb/Py interface. Zhu *et al.* [84] demonstrated an enhancement in T_c of ~ 10 mK in Nb/Py/SmCo multilayer where Py/SmCo XS films are in the form of a single crystal. They explain their results as an unanticipated proximity effect. In the same context, few reports establish [61–63] a suppression in T_c due to the generation of triplet pairs in S/F₁/F₂ multilayer.

In this chapter, we have presented a novel way to probe singlet-to-triplet conversion by diamagnetic screening currents. Typically, an in-plane magnetic field causes circulation of diamagnetic screening currents around the thickness of a superconducting film. The diamagnetic screening current, upon sensing a magnetically non-collinear structure at S/F interface may generate a triplet component that can extend into the F layer. Measurement of T_c of the S/XS/S system, defined as the onset of diamagnetic response, can indicate the process. With this motive, we have studied changes in T_c of Nb/Co/Py/Nb multilayer films through temperature-dependent magnetization measurements with an in-plane magnetic field. In the exchange-spring regime of the magnetic field, a relative enhancement in T_c was observed over the stray field-driven suppression of T_c . In this field range, the magnetic moments of Co and Py layers are aligned at an angle w.r.t. each other. We explain this recovery in T_c of ~ 400 mK as a consequence of singlet-triplet pair conversion at S/XS interface. Furthermore, we observe a reversible shift in T_c of ~ 400 mK in the spring range of Co/Py XS.

This chapter begins with the discussion of sample preparation and then discusses

the characterization of the spring system Co/Py. Subsequently, the changes in T_c and tunability of T_c observed in Nb/Co/Py/Nb, S/XS/S multilayer with different applied magnetic fields are discussed. As a control measurement, we compare these results with the case when Co/Py bilayer exhibits a single magnetization switching.

5.2 Experimental details

Nb/Co/Py/Nb multilayers of high purity (99.99%) Nb, Co and Py targets were deposited at room temperature using DC-magnetron sputtering on $5 \times 5 \text{ mm}^2$ Si/SiO₂ substrates (thermally grown). The deposition was performed at an Ar pressure of 1.5 Pa. The base pressure of the deposition system was $\sim 10^{-9}$ mbar. The thickness of Py was varied between (30-90) nm in steps of 15 nm. Nb and Co layer thicknesses were kept fixed at 55 nm and 30 nm, respectively. Magnetization measurements ($M(H)$, $M(T)$) were performed in a Quantum Design SQUID-magnetometer with in-plane applied magnetic fields. $T_c(H)$ were determined via magnetization vs temperature ($M(T)$) measurements at different in-plane applied magnetic fields.

5.3 Results and Discussion

5.3.1 Characterization of Co/Py spring system

In Fig. 5.2, we show the characteristic $M(H)$ loops (major and minor) at 300 K for Nb(55 nm)/Co(30 nm)/Py(30 nm)/Nb(55 nm) multilayer with in-plane magnetic fields. In a major $M(H)$ loop, the magnetic field was swept from +ve saturation to -ve saturation field and then, swept back to +ve saturation field. We observe a reversible minor loop up to -14 Oe but irreversibility appears on reversing from higher -ve fields, as shown in Fig. 5.2. The reversible minor loop of the Co/Py bilayer is a confirmation of its XS nature.

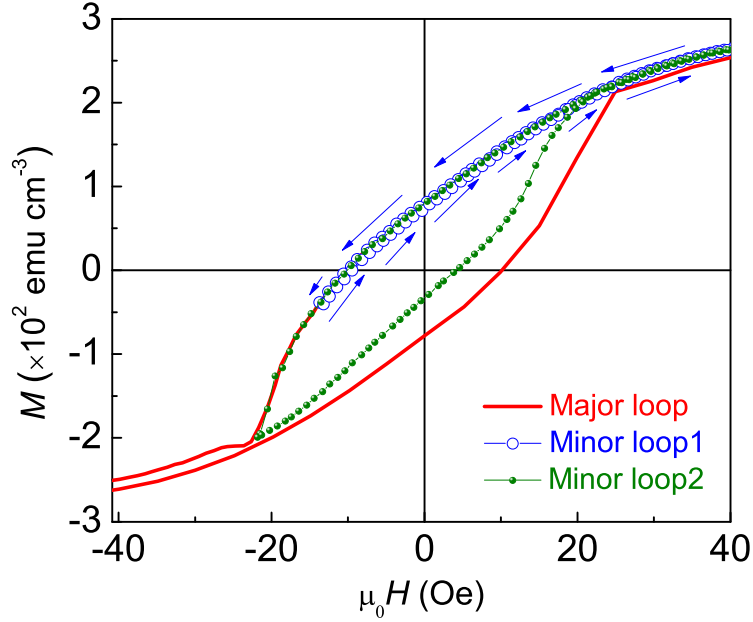


Figure 5.2: $M(H)$ loops (major and minor) at 300 K for Nb(55 nm)/Co(30 nm)/Py(30 nm)/Nb(55 nm) multilayer. Magnetic field is applied in the plane of the films.

Discussion

In Fig. 5.3, we show the schematic Nb/Co/Py/Nb multilayer having non-collinear magnetic structure. We have chosen Co/Py bilayer as a hard/soft ferromagnet combination due to their low coercive fields [109,133]. In a Co/Py bilayer, the exchange-coupling at Co/Py interface pins the permalloy layer moments to align in the same direction as Co layer moments at the interface. However, at the Nb/Py interface, the Py layer moments can rotate freely with an external applied magnetic field. For magnetic field oriented opposite to Co moments, within the spring range, Co and Py moments align at an angle with each other, as shown in Fig. 5.3. This magnetization angle gives a non-collinear magnetic structure, controllable with magnetic fields of few Oe. Furthermore, the magnetization is reversible in the spring range. The reversible nature of magnetization is the key to the tuning of a magnetic twist of non-collinear magnetic structure which offers the possibility of controlling singlet-triplet conversion.

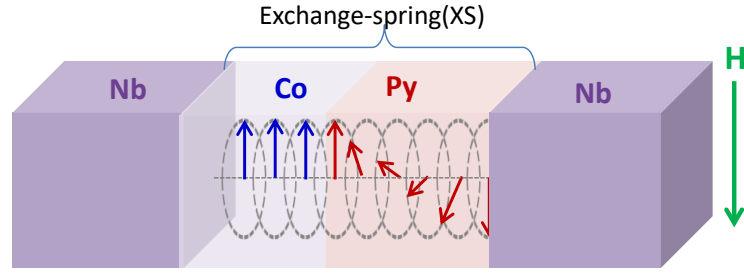


Figure 5.3: Schematic showing Nb/Co/Py/Nb multilayer in which Co/Py is an XS (a non-collinear structure of magnetic moments is expected for a specific field sequence).

5.3.2 Variation of T_c with magnetic configuration of Co/Py

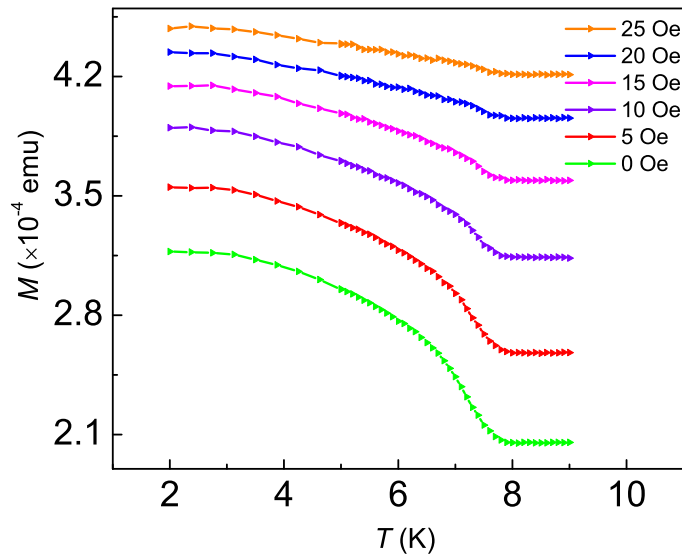


Figure 5.4: Magnetization vs temperature measurements for a Nb(55 nm)/Co(30 nm)/Py(30 nm)/Nb(55 nm) multilayer at different in-plane fields of 25 Oe, 20 Oe, 15 Oe, 10 Oe, 5 Oe and 0 Oe.

In order to study the variation of T_c with the magnetic configuration of Co/Py, we have performed $M(T)$ measurements for a series of S/XS/S multilayers in the presence of magnetic field. Fig. 5.4 shows the $M(T)$ measurements for Nb(55 nm)/Co(30 nm)/Py(30 nm)/Nb(55 nm) multilayer at different in-plane magnetic fields. The $T_c(H)$ curve was extracted from these $M(T)$ measurements. Samples were cooled in zero field for each measurement. Samples were magnetically saturated by applying a field of 200 Oe at 2 K and then, the measurement field was set at the same

temperature, in order to obtain a non-collinear magnetic structure following the $M(H)$ curve.

In Fig. 5.5, we show the $T_c(H)$ curve for Nb(55 nm)/Co(30 nm)/Py(30 nm)/Nb(55 nm) multilayer. For the multilayers, $M(T)$ curves were measured at several fields between +ve and -ve saturation. In $T_c(H)$ curve, as shown in Fig. 5.5, as the field is reduced from saturation, T_c reduces drastically. However, in the XS range, a recovery in T_c was observed. The error bar in the $T_c(H)$ curve is 0.2 K, which has been taken from the step size of $M(T)$ measurement.

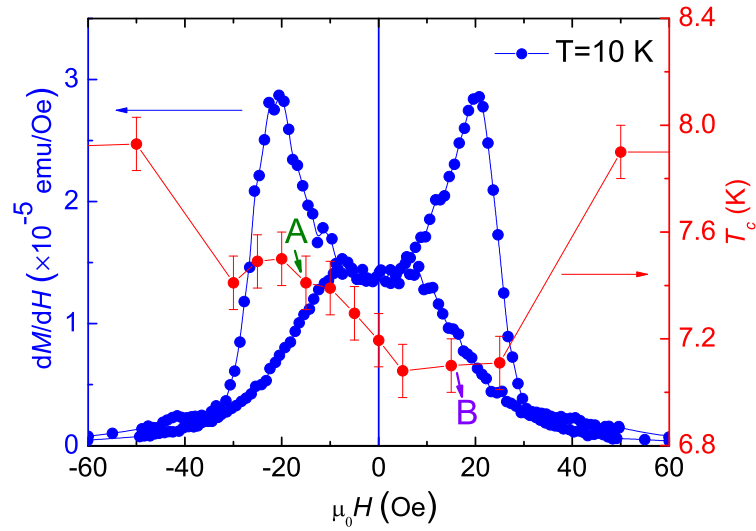


Figure 5.5: T_c as a function of an in-plane field H is represented by red points on the right axis and dM/dH is represented by blue points on the left axis for a Nb(55 nm)/Co(30 nm)/Py(30 nm)/Nb(55 nm) multilayer.

To emphasize the change in T_c in $T_c(H)$ curve, in Fig. 5.6, we have shown $M(T)$ measurements at two fields denoted by points A and B in Fig. 5.5. An increase in moment was observed below T_c in many cases, which is unlike the usually expected diamagnetic response of a superconductor. However, the present situation is possible in cases which involve a magnetic field history during the measurement. Irrespective of the nature of $M(T)$ curves, the T_c remains unchanged under field history conditions. To clarify this point, we performed $M(T)$ measurements for a Nb (60 nm) film under different conditions of magnetic field history, as shown in

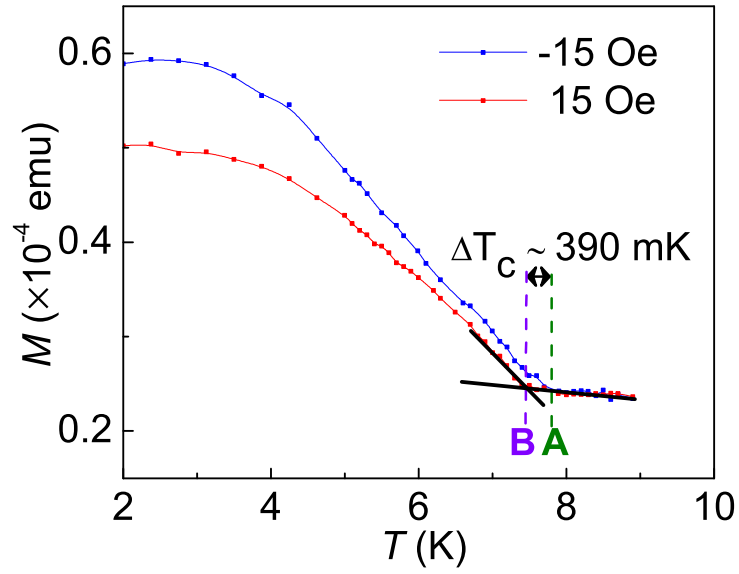


Figure 5.6: Representative $M(T)$ curves corresponding to the points A and B of Fig. 5.5 from which T_c was estimated.

Fig 5.7. We find that T_c remains same (~ 8 K) in all cases, even though the low temperature magnetizations are different in all cases.

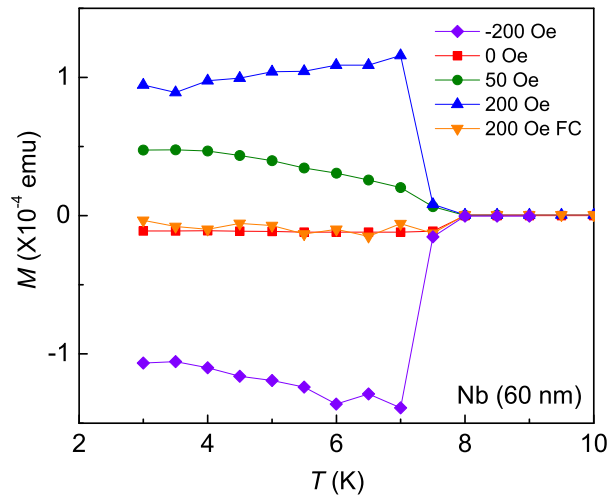


Figure 5.7: Magnetization vs temperature measurements for a Nb (60 nm) thin film under different magnetic history

Fig. 5.8 shows the comparison of $T_c(H)$ curves for different samples of Nb/Co(30 nm)/Py(x)/Nb multilayer series with x values of 30 nm, 45 nm, 75 nm and 90 nm. We observe similar recovery of T_c for all samples in the non-collinear range of magnetic fields.

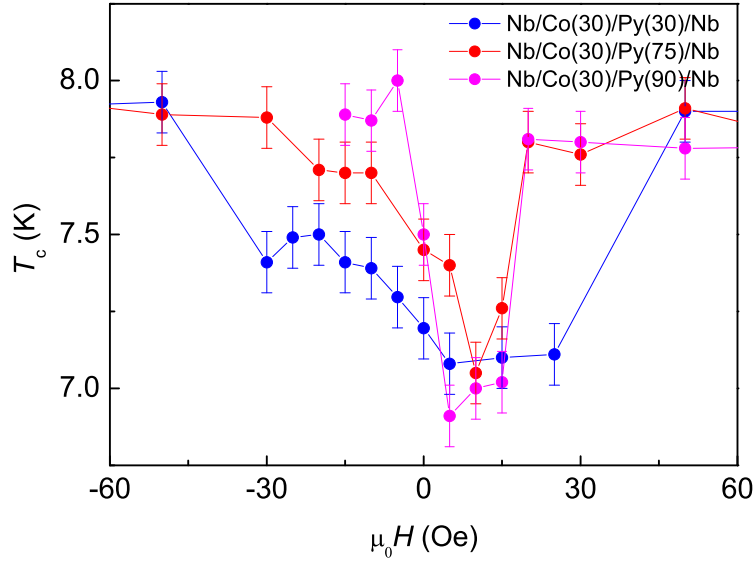


Figure 5.8: Comparison of $T_c(H)$ (extracted from $M(T)$ measurements) curves for Nb/Co(30 nm)/Py(30 nm)/Nb (blue points), Nb/Co(30 nm)/Py(75 nm)/Nb (red points) and Nb/Co(30 nm)/Py(90 nm)/Nb (pink points) multilayers.

Discussion

Figure 5.5 shows that dM/dH starts to rise below 40 Oe as the applied magnetic field is reduced from saturation, indicating the nucleation of domain walls in Py. Once the Py domains start to rotate around a field of 30 Oe, the exchange spring in Py forms with a corresponding change in magnetic moment i.e. dM/dH sharply rises. The exchange spring range is therefore defined from the field where dM/dH sharply rises in Fig. 5.5 (matching with the opening of hysteresis loop and also with the opening of dM/dH loop), indicating the rotation of Py domains. This range spans from +30 Oe to -30 Oe. In this field range we see a consistent recovery of T_c from 7.1 K. The initial drop in T_c from 7.9 K to 7.1 K is thus outside the exchange spring field range. In the spring range, a magnetically non-collinear structure manifests in Co/Py XS. Therefore, the singlet pairs may convert to triplet pairs resulting in an increase in T_c .

We emphasize the fact that in a thin film geometry, the Co and Py layers are multi-domain with a distribution of domain sizes. From magnetization vs in-plane

magnetic field $M(H)$ loops (and from the calculated dM/dH curves) it is clear that neither the Co nor the Py magnetizations sharply switch direction as the magnetic field sweeps from positive to negative saturation. This is essentially due to the multi-domain nature of Co and Py. Therefore, we should expect a degree of magnetic non-collinearity between magnetic moments of Co and Py during the magnetization reversal of Py and Co. During rotation of Py domains (while Co layer has not started rotating), the Nb/Py interface is magnetically inhomogeneous which favours singlet-to-triplet pair conversion due to diffusion of diamagnetic current across the interface. Similarly, during the gradual rotation of Co domains (while Py domains have already reversed) the Nb/Co interface is effective for singlet-to-triplet pair conversion. In our experiment, we are probing the superconductor proximity effects and singlet-to-triplet pair conversion via modifications of diamagnetic current distribution in Nb.

Previous experiments [83,84] investigate pair conversion via critical temperature (T_c) measurements, where shifts in T_c are determined through changes in electronic resistance with magnetic field. Such measurements, however, are not volumetric since only the highest T_c within the S layer is extracted - i.e. currents shunt to regions in Nb with the highest T_c . In our experiment we choose a different approach in which T_c is determined from magnetization measurements which are volumetric and hence T_c is representative of the entire multilayer. We used two Nb layers in order to amplify the diamagnetic signal which decreases the error associated with values of T_c with and without an XS interface.

To further investigate the origin of the recovery of T_c , we performed $M(T)$ measurements for Nb(55 nm)/Co(30 nm)/Py(45 nm)/Nb(55 nm) multilayer where Co(30 nm)/Py(45 nm) bilayer does not act like an XS. Previous literature [125–127] establish that a hard/soft ferromagnetic bilayer can either behave as an XS or a single magnetic film for different thickness combinations of hard and soft layer. Fig. 5.9 shows the $M(H)$ loop along with $T_c(H)$ curve for Nb(55 nm)/Co(30 nm)/Py(45

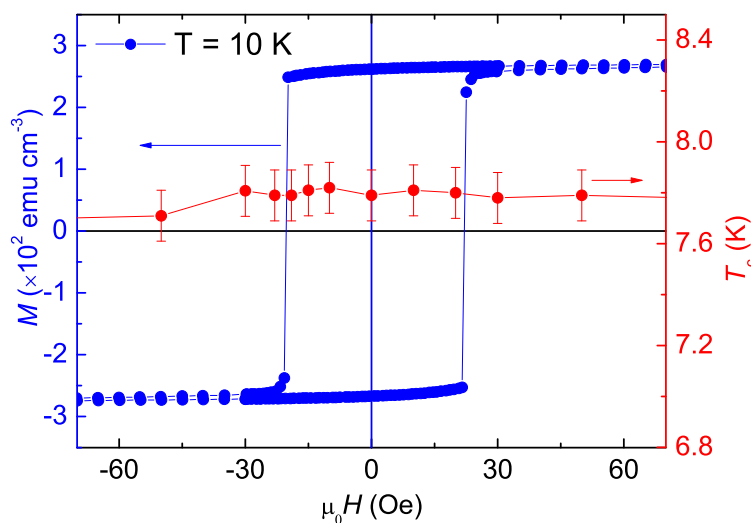


Figure 5.9: $T_c(H)$ curve for Nb(55 nm)/Co(30 nm)/Py(45 nm)/Nb(55 nm) is represented by red points on the right axis and the $M(H)$ loop of the same stack at 10 K is represented by blue points on the left axis). The square $M(H)$ loop indicates that the magnetic configuration is collinear.

nm)/Nb(55 nm) multilayer. We find that the Co(30 nm)/Py(45 nm) combination acts as a single magnetic film with a single magnetization switching. No change in T_c was observed for H varying from +ve saturation to -ve saturation. The comparison of Fig. 5.9 and Fig. 5.8 shows that the recovery of T_c happens only when a non-collinear magnetic structure forms in the magnetic layers. This non-collinear magnetic structure can cause singlet-to-triplet pair conversion and hence, a recovery of T_c in the non-collinear range of magnetic fields.

5.3.3 Reversible tuning of T_c in spring range

In Fig. 5.10, we show a representative measurement of reversible tuning of T_c for fields lying in XS range for Nb(55 nm)/Co(30 nm)/Py(90 nm)/Nb(55 nm) multilayer. Fig. 5.10 shows the $M(T)$ curves for a measurement field (H_{meas}) of 11 Oe and for different returning fields (H_{ret}). For every measurement, sample was first saturated by applying a field of 200 Oe at 2 K and then returning field was set and finally, field was set to the measurement field value of 11 Oe in all cases. We denote the saturation field of 200 Oe as S. The field sweep cycle for points A, B, C, D and

E marked in Fig. 5.10(a) are a: S→A, b: S→B→A, c: S→C→A, d: S→D→A, e: S→E→A, respectively. We observe no change in T_c for returning field values lying in the spring range which is from 20 Oe to 0 Oe. However, a reduction in T_c of ~ 400 mK was observed for returning field values lying outside the spring range as shown in Fig. 5.5(a).

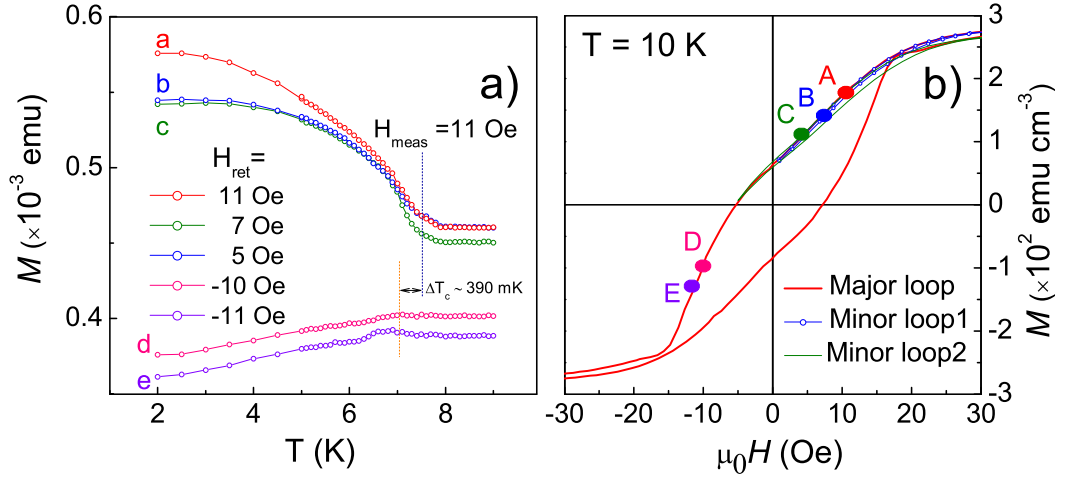


Figure 5.10: (a) $M(T)$ curves for Nb(55 nm)/Co(30 nm)/Py(90 nm)/Nb(55 nm) multilayer, measured at $H_{meas} = 11$ Oe for different returning fields H_{ret} lying inside and outside the spring range. (b) $M(H)$ loop of Nb(55 nm)/Co(30 nm)/Py(90 nm)/Nb(55 nm) multilayer at 10 K, the returning fields for paths a, b, c, d, e shown in (a) are marked as A, B, C, D, and E.

Discussion

The T_c at the saturation field was 7.7 K for the Co(30 nm)/Py(90 nm) sample. For fields lying in non-spring range, $M(H)$ minor loops are irreversible as shown in Fig. 5.10(b). This is because some of the Co domains that have rotated in the negative field direction (for points D and E) cannot switch back to the positive field (measurement field at point A) direction. Therefore, there is a net reduction in magnetic non-collinearity whilst sweeping the field from points D and E to A in Fig. 5.10(b). We observe in Fig. 5.10(a) that the reduced magnetic non-collinearity results in a reduction of T_c from about 7 K to 7.5 K for non-hysteretic returning

fields B and C. In this way, it is possible to tune the T_c of S/XS/S multilayer with very small applied magnetic fields (~ 20 Oe).

5.4 Conclusion

We have investigated changes in T_c in a series of Nb/Co/Py/Nb multilayer using $M(T)$ measurements. XS behavior in Co(30 nm)/Py(30 nm), Co(30 nm)/Py(75 nm) and Co(30 nm)/Py(90 nm) thickness combinations were confirmed by magnetization measurements, whereas we find that Co(30 nm)/Py(45 nm) and Co(30 nm)/Py(60 nm) exhibit a single magnetization switching. $T_c(H)$ curves were studied for all the samples including XS and non XS combination of Co/Py. In XS samples, we find a drop in T_c as we reduce the field from saturation to a field where the $M(H)$ loop starts to open up. This decrease in T_c has been interpreted as the result of stray fields of domain walls of Py. However, we observed a recovery of T_c in XS region. In XS range, the non-collinear structure of magnetic moments is established, as evident from the $M(H)$ loops shown in Fig. 5.2. Therefore, one of the possible reasons for this recovery is the singlet-to-triplet conversion through the magnetically non-collinear structure. One can argue that the stray field cancellation of Co and Py moments may also be one of the reason for this recovery of T_c . However, in that case, the T_c of the sample in the non-collinear range should be higher than that in the saturation which corresponds to highest stray field, unlike the case here. Therefore, the possibility of stray field cancellation was excluded. Such a recovery of T_c was observed in all the XS samples. On the other hand, no change in T_c was observed in the case of non-spring combination of Co/Py. The comparison of $T_c(H)$ of spring samples with non-spring samples shows that the T_c is dependent on the internal magnetic structure of Co/Py bilayer. We have also shown a reversible shift of the T_c in the spring range of magnetic fields. Therefore, it is also possible to realize singlet-to-triplet conversion by studying T_c changes in simple geometry.

Chapter 6

Triplet supercurrents in Josephson junctions with symmetric and asymmetric exchange-spring barrier

6.1 Introduction

Josephson junctions containing multiple ferromagnetic layers forming a magnetic non-collinear structure at the S/F interface can carry spin-triplet supercurrents. Over the past decade, almost all the experiments in this direction have used S/F'/F'/S Josephson junction geometry proposed by Houzet and Buzdin in 2007 [15], where the magnetization vectors of F and F' layers are non-parallel. It has been proposed that the S/F'/F interfaces convert spin-singlet Cooper-pairs to spin-polarized triplet Cooper-pairs and the F'/F/S interfaces convert back the spin-polarized triplet Cooper-pairs to spin-singlet Cooper-pairs. In this way, a Josephson coupling is established between the two S electrodes. Similarly, in a Josephson junction with an asymmetric magnetic barrier as F'/F bilayer, the triplet Josephson coupling is possible from theoretical proposals [128,129]. In the S/F'/F/S Josephson junction, the singlet-to-triplet conversion happens at S/F'/F interfaces. However, the triplet pairs would decay inside

the singlet superconducting layers, over a length scale of the order of coherence length of the superconductor. Therefore, the mechanism for the transport of triplet Cooper-pairs in an asymmetric junction is not very clear. Theoretically, it has been proposed [128,129] that Josephson coupling is established through a double Andreev reflection process and a super-harmonic Josephson current flows in the junction. There are, however, no experimental reports on such asymmetric triplet junctions. For a better understanding of the basic mechanisms underlying triplet physics, we need to investigate the triplet supercurrents in Josephson junctions with symmetric and asymmetric magnetic barriers in the same geometry.

In addition to the fundamental aspects of triplet supercurrents, these synthetic magnetic barriers also allow tuning of junction supercurrent by external magnetic fields, which is a major goal of superconducting spintronics applications. In this direction, Banerjee *et al.* [59] demonstrated reversible triplet supercurrents in Nb/Py/Cu/Co/Cu/Py/Nb junctions while Iovan *et al.* used Nb/CuNi/Cu/CuNi/Nb spin-valve junction to control triplet supercurrents. However, the evidence of triplet supercurrents appeared during the magnetization reversal process in these reports while sweeping an external magnetic field. Other groups [61–65,130] have reported similar control using S/F/F' spin-valves by studying the changes in T_c of multilayer. More recently, Martinez *et al.* [17] demonstrated on/off control of spin-triplet supercurrents in multi-ferromagnet S/F/S Josephson junctions.

To control triplet supercurrents in S/F/S junctions, one needs to be able to tune the degree of magnetic inhomogeneity present at S/F interfaces. Magnetic exchange-spring (XS), which is essentially a synthetic domain wall, is a potential candidate to achieve such a tunable non-collinear magnetic structure. It consists of neighboring magnetically hard and soft ferromagnetic materials in which the soft layer is exchange-coupled at hard/soft ferromagnet's interface in such a way that magnetization of the soft layer can rotate reversibly within a certain range of external magnetic field. The non-collinear magnetic structure formed in magnetically

soft layer is tunable with small (<50 mT) external magnetic fields [131]. There is a recent report on SmFe/Py [83], S/XS bilayer, where the authors have demonstrated an enhancement in T_c as the evidence of triplet proximity effect [83].

In this chapter, we present control of triplet supercurrents with magnetic-field-orientation in Josephson junctions with asymmetric (Co/Py) and symmetric (Py/Co/Py) XS barriers. We observed long-range triplet supercurrents for Py thickness up to 11 nm which is an order of magnitude larger than the singlet pair coherence length in Py ($\xi_{Py} \sim 1.4$ nm) [42]. We also demonstrate that the maximum Josephson current is dependent on the magnetic field orientation.

6.2 Experimental details:

6.2.1 Film Growth.

We have prepared Nb(220 nm)/Co(2 nm)/Py(0-13 nm)/Nb(220 nm) and Nb(220 nm)/Py(1-13)/Co(2 nm)/Py(1-13)/Nb(220 nm) multilayers at an Ar pressure of 1.5 Pa, using DC-magnetron sputtering of high purity (99.99%) Nb, Co and Py ($\text{Ni}_{80}\text{Fe}_{20}$) targets, on thermally grown Si/SiO₂ substrates. Prior to the deposition, the base pressure of the chamber was $\sim 10^{-9}$ mBar. The films were grown while rotating the substrate plate under the sputtering plasma. The thicknesses of the films were controlled using the rotation speed of the substrate plate and calibrated using X-ray reflectivity (XRR).

6.2.2 Device Fabrication.

The Josephson junctions were fabricated in two steps. In the first step, we made 30- μm -long and 4- μm -wide tracks with contact pads using optical lithography and Ar-ion-milling [132], as shown in the FESEM image of Fig. 6.1(a) and (b). Next, we used the side cutting technique of the Ga-ion based Focused Ion Beam (FIB)

milling process to prepare the nano-pillar Josephson junctions, as shown in the FESEM image of Fig. 6.1(c) and FIB image of Fig. 6.1(d). We varied the device dimensions from $(300 \times 300) \text{ nm}^2$ to $(300 \times 500) \text{ nm}^2$ using FIB.

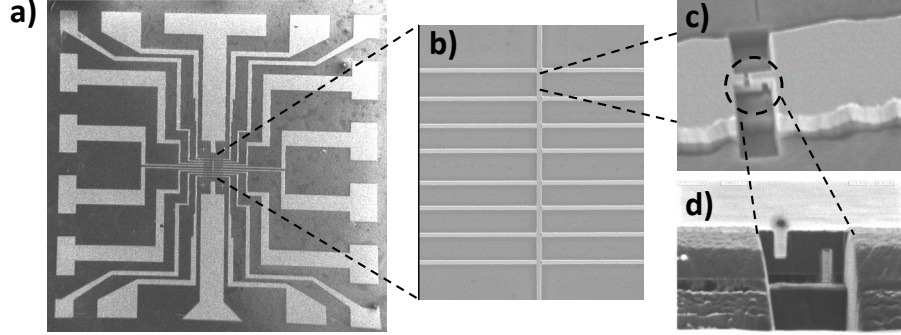


Figure 6.1: (a) FESEM image showing the pattern of the sample defining the contact pads for the Nb/Co/Py/Nb nano-pillar devices. (b) FESEM micrograph showing the zoomed view of track over which the devices were made using Ga-ion based FIB, (c) the FESEM image showing perspective view of a nano-pillar Josephson junction, (d) the FIB image showing the cross sectional view of a nano-pillar Josephson junction.

6.2.3 Transport and magnetization measurements.

We performed electrical transport measurements ($I-V$, $R(T)$, $R(H)$) using a dipstick probe in a liquid He dewar. Standard four-probe current-biased configuration was used to perform current-voltage ($I-V$) measurements. All the field rotation measurements were performed using a commercial cryogen-free cryostat system. The sample holder on the probe was rotated manually for a fixed direction of the magnetic field to perform field rotation measurements. We used a wire bonder to make contacts on the devices in four-probe geometry, for electrical transport measurements. Magnetization ($M(H)$) measurements were performed using a Quantum Design SQUID-magnetometer. In all cases, magnetization measurements were performed with magnetic field applied in the plane of the multilayer films.

6.3 Results and Discussion

6.3.1 Magnetic characterization of Co/Py exchange-spring system

In Fig. 6.2, we show a schematic of a nano-pillar Josephson junction, along with the hysteresis loop of the unpatterned Nb/Co(2 nm)/Py(11 nm)/Nb multilayer at 10 K. In a Co/Py bilayer, Co is magnetically hard and Py is magnetically soft, due to the difference in their coercive fields (H_c) [109,133]. After saturating the magnetic moments of the bilayer, if a magnetic field is applied anti-parallel to the Co magnetization, a non-collinear magnetic structure forms in the Py due to an interfacial exchange coupling of Co/Py bilayer, as shown in Fig. 6.2(c). In Fig. 6.2(a), we show the major and minor hysteresis loops for in-plane applied magnetic fields. In the major loop, the magnetic field was varied from a positive saturation field to a negative saturation field and reversed back to the positive saturation field. In the minor loop, magnetic field was varied from positive saturation field to a field value less than the negative saturation field and reversed back to the positive saturation, as shown by the (Δ) and (\circ) marked curves in Fig. 6.2(a). Fig. 6.2(b) shows the field derivative curve of the same multilayer, where dM/dH is extracted from the $M(H)$ curve shown in Fig. 6.1(a). The plateau observed in dM/dH curve indicates that there is a misalignment between the moments of Co and Py layers, for a certain range of magnetic fields. Also, the minor loops were reversible up to a field value of -2 mT, as shown in Fig. 6.2(a). The irreversible nature begins on reversing from field values higher than -2 mT on the opposite side, as shown in Fig. 6.2(a). The reversible range of magnetic field (± 2 mT in Fig. 6.2(a)) allows for a tunable magnetic non-collinearity in Py.

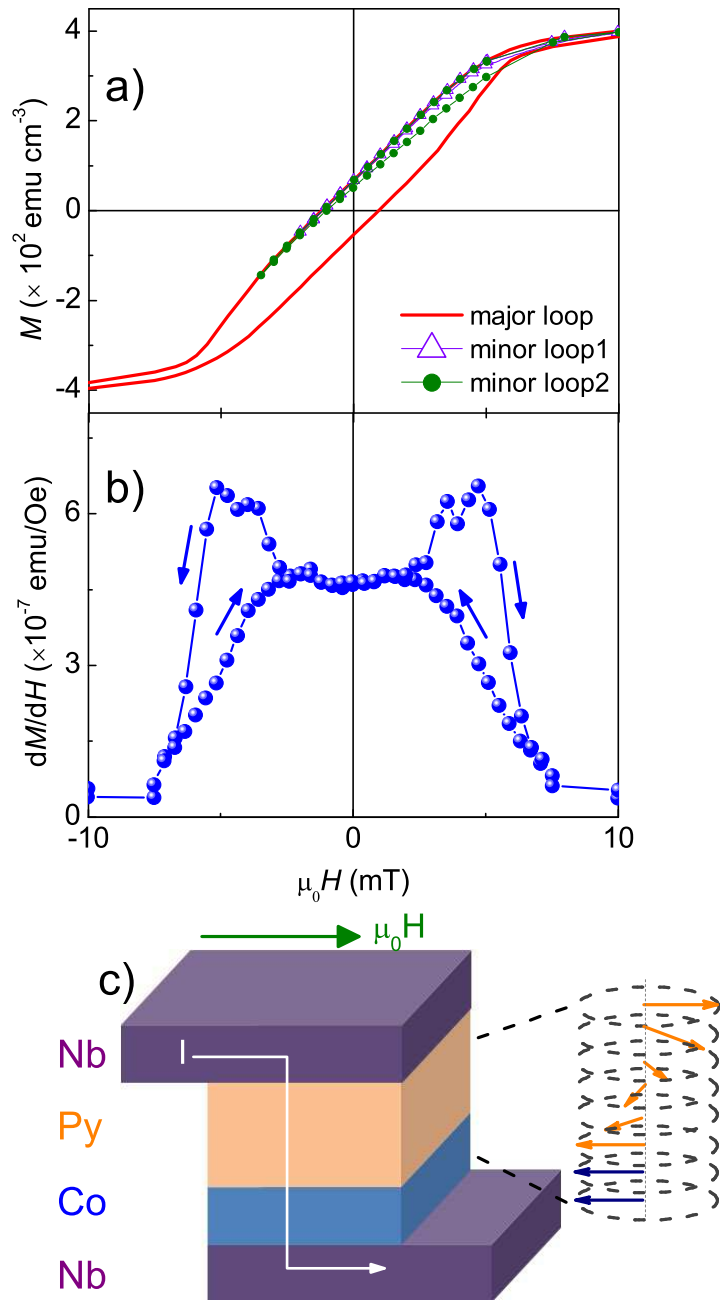


Figure 6.2: (a) Major and minor magnetic hysteresis loops of an unpatterned Nb/Co(2 nm)/Py(11 nm)/Nb multilayer at 10 K in an in-plane magnetic field. For a range of magnetic fields the minor loops are reversible, which is the hallmark of exchange-spring behavior. (b) The field derivative curve of an unpatterned Nb/Co(2 nm)/Py(11 nm)/Nb multilayer at 10 K. (c) Schematic illustration of a nano-pillar Josephson junction with an XS barrier, the non-collinear magnetic structure is created following a specific field sequence.

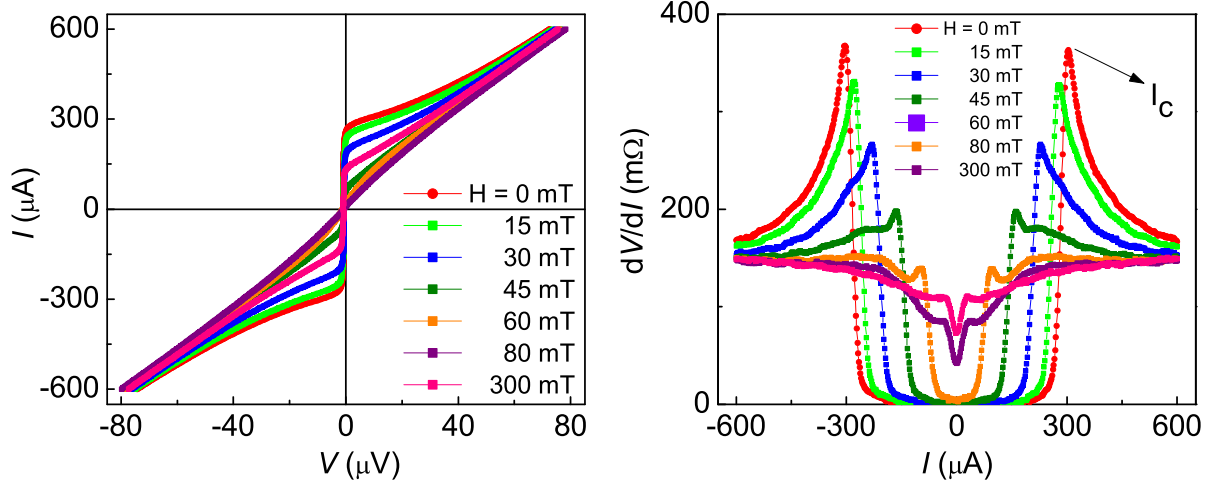


Figure 6.3: (a) I - V curves for different in-plane magnetic fields of 0 mT, 15 mT, 30 mT, 45 mT, 60 mT, 80 mT and 300 mT for a Nb/Co(2 nm)/Py(7 nm)/Nb device with dimensions of $(300 \times 350) \text{ nm}^2$ at 4.2 K. (b) dV/dI versus I curves for different in-plane magnetic fields of 0 mT, 15 mT, 30 mT, 45 mT, 60 mT, 80 mT and 300 mT for the same device.

6.3.2 Asymmetric exchange-spring junction characteristics

In Fig. 6.3, we show the current-voltage (I - V) characteristics and dV/dI versus I curves for a Nb/Co(2 nm)/Py(7 nm)/Nb Josephson junction at 4.2 K for different in-plane applied magnetic fields. In the (I - V) curves, critical current (I_c) is defined as the bias current, where dV/dI becomes maximum, as shown by the black arrow in Fig. 6.3(b). We observe a change in I_c with an in-plane magnetic field.

In Fig. 6.4, we plot the in-plane $I_c(H)$ curve for a Nb/Co(2 nm)/Py(7 nm)/Nb Josephson junction device at 4.2 K. The Fraunhofer modulations of critical current observed in $I_c(H)$ curve in Fig. 6.4(a) confirms a Josephson coupling in this device. There is an offset ($H_{offset} = \pm 2.6 \text{ mT}$) in the I_c maxima from zero magnetic field, which occurs due to an intrinsic barrier flux arising from the magnetization of ferromagnetic barrier. In Fig. 6.4(b), we show the zoomed view of the low field region of the $I_c(H)$ curve of Fig. 6.4(a) along with the $M(H)$ curve of an unpatterned multilayer measured at 10 K. From this comparison, we observe that the offset field corresponds nearly the coercive field ($\pm 2.5 \text{ mT}$) of unpatterned multilayer

at 10 K. We find that there is a small difference between the H_c and H_{offset} in

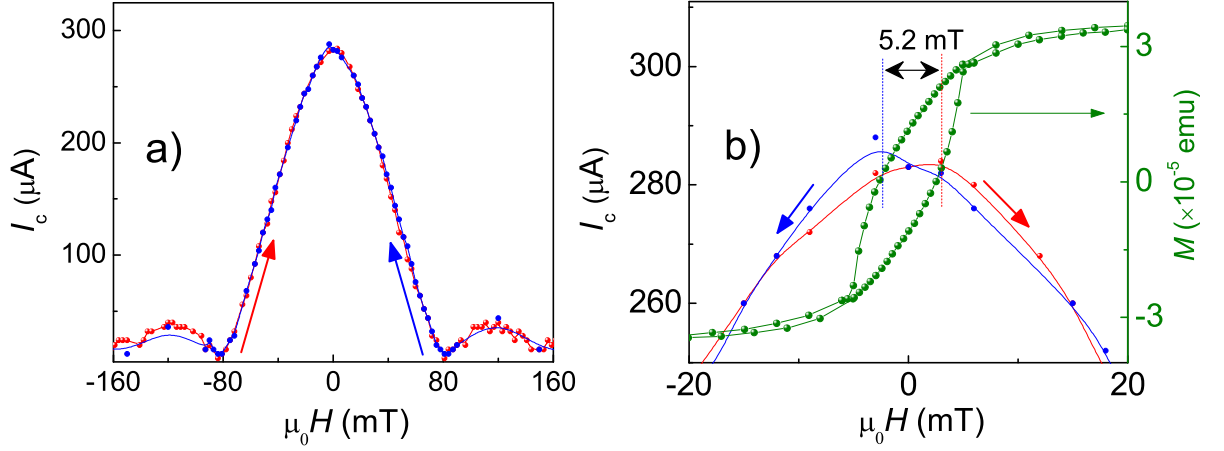


Figure 6.4: (a) The Fraunhofer modulation of I_c with an in-plane applied magnetic field for a Nb/Co(2 nm)/Py(7 nm)/Nb XS Josephson junction at 4.2 K for a device dimension of $300 \times 350 \text{ nm}^2$. (b) Low field regime of Fraunhofer modulation showing hysteresis.

the Fraunhofer pattern. This difference can arise due to two reasons: (i) The H_c is taken from a $M(H)$ curve of a thin film whereas H_{offset} is taken for the devices and, (ii) Devices were fabricated using the Ga-ion beam, therefore, it is likely to have some Ga ion implantation, which may change the coercive field. Robinson *et al.* [42] have shown that the singlet pair coherence length of Py is very low, $\xi_{Py} \sim 1.4 \text{ nm}$. We have observed Josephson coupling for Py thickness (7 nm) much higher than $\xi_{Py} \sim 1.4 \text{ nm}$. The long-range nature of supercurrents observed in these junctions confirms its triplet nature.

6.3.2.1 Magnetization configuration dependent critical current

In Fig. 6.5, we plot resistance as a function of θ for Nb/Co(2 nm)/Py(11 nm)/Nb junction at 1.6 K and for field values of 0 mT, 20 mT, and 400 mT. R is defined as the junction resistance at a current bias near I_c . Here, we define θ as the in-plane angle of applied magnetic field ($\mu_0 H$) with reference to the length of the track (x-axis), as shown in the schematic illustration of the measurement geometry in Fig. 6.5(a).

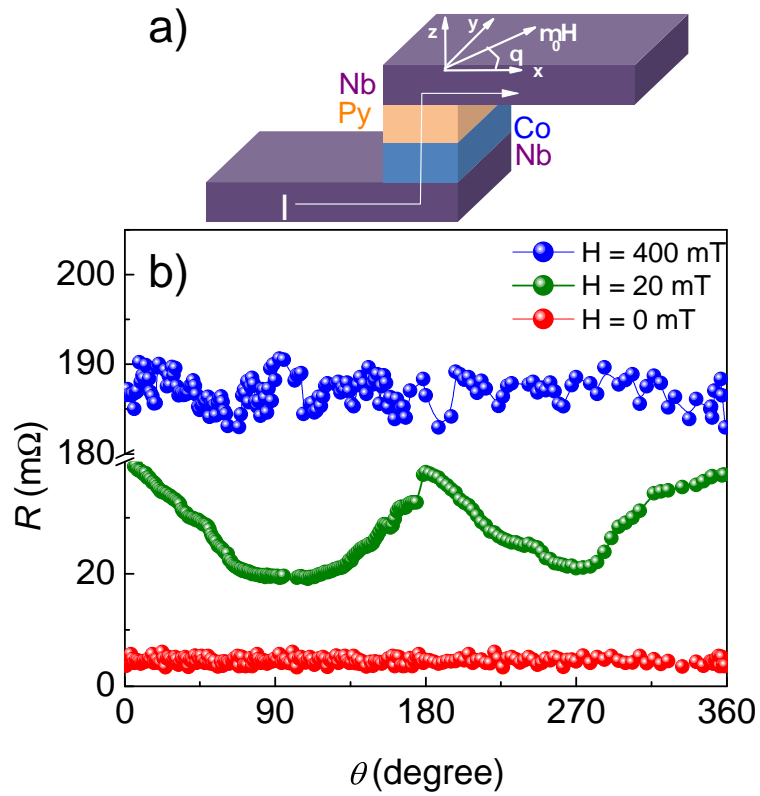


Figure 6.5: (a) Schematic illustration of direction of bias current I and applied magnetic field $\mu_0 H$ (b) Resistance vs direction of applied magnetic field showing manipulation of triplet supercurrents for Nb/Co(2 nm)/Py(11 nm)/Nb Josephson junction with dimensions of ($\sim(300 \times 300)$ nm 2) at 1.6 K and for field values of 0 mT, 20 mT and 400 mT. Here, theta denotes the angle of the direction of applied magnetic field with respect to the length of the track (x-axis).

In the $R(\theta)$ curves, 400 mT refers to the saturation state. For the $R(\theta)$ measurement at 20 mT, an in-plane magnetic field of 400 mT was applied to saturate both the Co and Py layers and then, the magnetic field was reduced to 20 mT along the x-axis. Thereafter, the sample was rotated in the x-y plane, as shown in Fig. 6.5(a), at a fixed magnetic field of 20 mT. An in-plane rotation of the sample is equivalent in-plane rotation of magnetic field for a stationary sample. Henceforth, the rotation of sample will be regarded as the rotation of magnetic field, throughout the text. In a Josephson junction, the resistance versus angle is a reflection of critical current versus angle for bias currents near the critical current [16]. To illustrate this, we have shown the $I_c(H)$ and $R(H)$ for Nb/Co(2 nm)/Py(7 nm)/Nb junction at 4.2 K in Fig. 6.6.

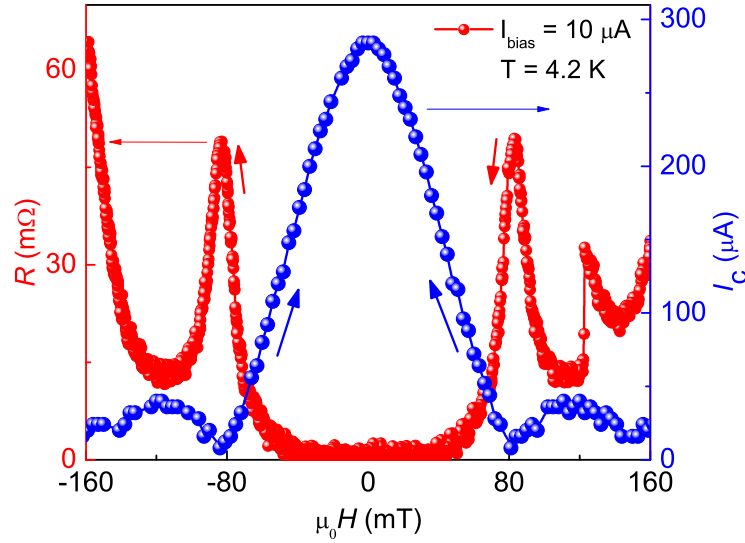


Figure 6.6: Comparison of $I_c(H)$ and $R(H)$ curves for Nb/Co(2 nm)/Py(7 nm)/Nb Josephson junction. Red points on left hand axis represent the $R(H)$ curve while blue points on right axis represent the $I_c(H)$. The minima in $I_c(H)$ and the maxima in $R(H)$ lie at same magnetic field, signifying the equivalence of both measurements.

The minima in I_c correspond to the maxima in resistance and vice-versa. With a change in θ , the twist of the magnetic structure formed within the Py layer changes, and hence the amount of triplet supercurrent varies. The different angles of rotation correspond to different non-collinear magnetic structures formed in the Py layer. Recent reports [83,84] show a non-monotonic variation of resistance as

a function of an applied magnetic field in S/XS hybrids. These reports [83,84] suggest that different angles of rotation correspond to different equilibrium magnetic configurations of the XS, leading to a change in the amplitude of long-range triplet correlations. We observe that the maximum resistance, and hence, the minimum I_c , corresponds to the 0° and 180° of applied magnetic field whereas the minimum resistance (maximum I_c) corresponds to 90° and 270° of applied magnetic field as shown in Fig. 6.5(b). Thus, we can manipulate the triplet supercurrents as a function of the direction of applied magnetic field.

6.3.3 Double (symmetric) exchange-spring junction characteristics.

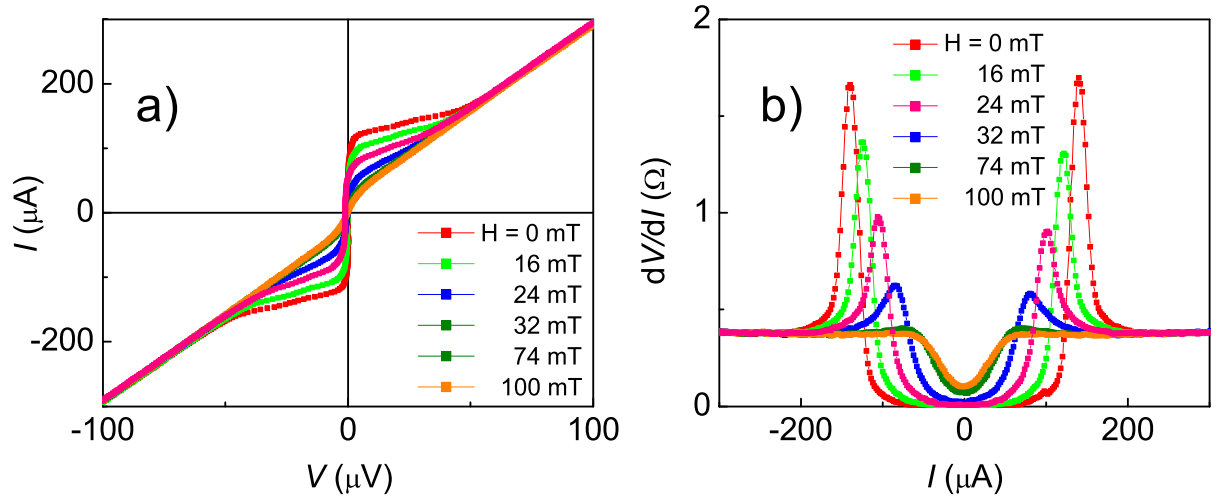


Figure 6.7: (a) I - V curves for different in-plane magnetic fields for a double exchange-spring Nb/Py(7 nm)/Co(2 nm)/Py(7 nm)/Nb Josephson junction with dimensions of $(300 \times 300) \text{ nm}^2$ at 1.6 K. (b) dV/dI versus I curves for different in-plane magnetic fields for the same device.

Fig. 6.7 shows the current-voltage (I - V) characteristics and dV/dI versus I curves for a Nb/Py(7 nm)/Co(2 nm)/Py(7 nm)/Nb Josephson junction at 1.6 K. In the (I - V) curves, critical current (I_c) is defined as the bias current where dV/dI becomes maximum. We observe a change in I_c with in-plane magnetic fields, as shown in Fig. 6.7(a) and (b). In Fig. 6.8(a), we show the $I_c(H)$ curve for a Nb/Py(7 nm)/Co(2 nm)/Py(7 nm)/Nb Josephson junction at 1.6 K. We observe modulations in

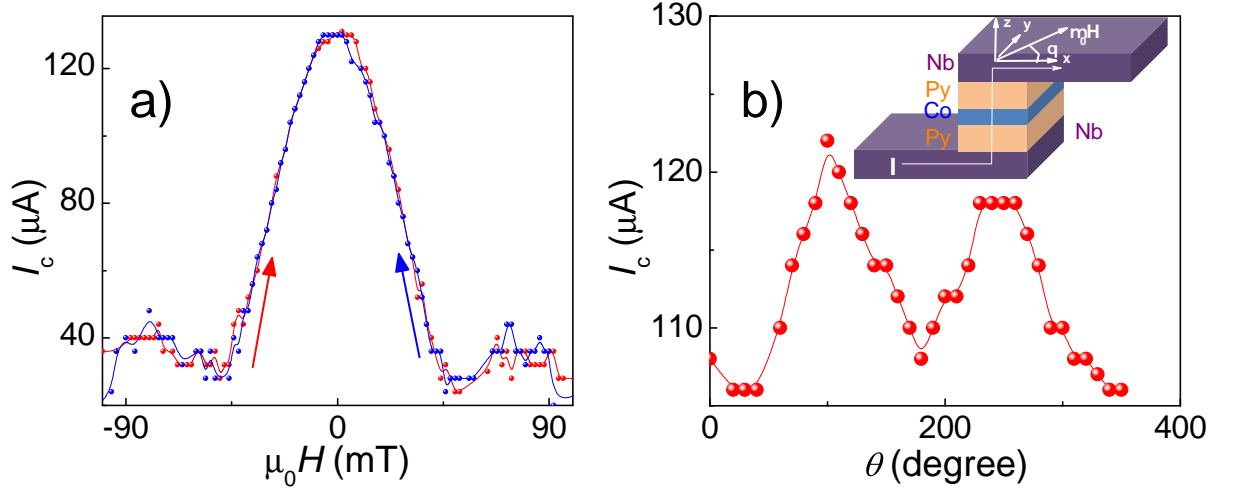


Figure 6.8: (a) Fraunhofer modulations of $I_c(H)$ for a double exchange-spring Nb/Py(7 nm)/Co(2 nm)/Py(7 nm)/Nb Josephson junction with dimensions ($\sim 300 \times 300$ nm²) at 1.6 K. (b) Critical current vs direction of applied magnetic field showing manipulation of triplet supercurrents at 1.6 K and a field value of 20 mT; Here, theta denotes the angle of applied magnetic field with respect to the length of the track.

I_c with in-plane applied magnetic fields, which confirms the Josephson coupling in this device.

These devices follow the behavior of S/F'/F/F'/S device proposed by Houzet and Buzdin [15]. We examined Josephson coupling through the $I_c(H)$ modulations for a series of devices, where the thickness of Co layer was fixed (2 nm) and the thickness of Py layer was varied from 1 nm to 9 nm. We observed supercurrents up to a total ferromagnet thickness of 16 nm (Py(7 nm)/Co(2 nm)/Py(7 nm)), which greatly exceeds the singlet pair coherence length of strong ferromagnets like Co ($\xi_{Co} \sim 3$ nm) and Py ($\xi_{Py} \sim 1.4$ nm) [42]. The long-range nature of the supercurrent shows that the Josephson coupling is due to triplet supercurrents in these devices.

In Fig. 6.8(b), we show the $I_c(\theta)$ curve for Nb/Py(7 nm)/Co(2 nm)/Py(7 nm)/Nb device at 20 mT and 1.6 K. We find that the maxima in I_c appears at angles of 90° and 270° while minima appears at 0° and 180° of applied magnetic field. This result is similar to the results obtained in XS junctions, in Fig. 6.6(a).

Discussion

To further confirm the long-range triplet nature of the supercurrent, we performed

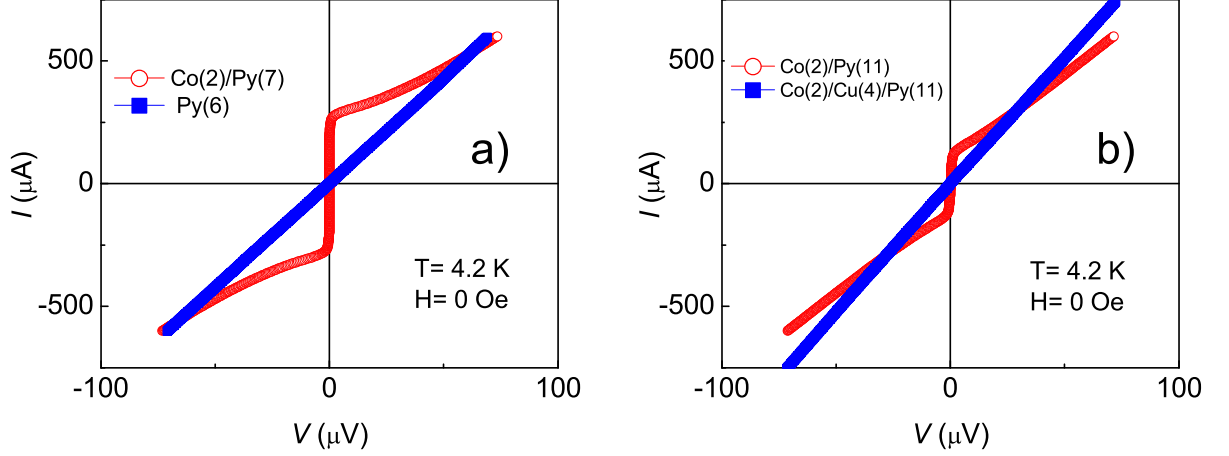


Figure 6.9: (a) Comparison of I - V curves of a Nb/Co(2 nm)/Py(7 nm)/Nb junction with a Nb/Py(6 nm)/Nb junction at a temperature of 4.2 K and zero field. (b) Comparison of I - V curves of a Nb/Co(2 nm)/Py(11 nm)/Nb junction with a Nb/Co(2 nm)/Cu(4 nm)/Py(11 nm)/Nb junction at a temperature of 4.2 K and zero field.

some control measurements as shown in Fig. 6.9. In the first case, we measured a junction with no Co layer in Nb/Py(6 nm)/Nb configuration. In Fig. 6.9(a), we show the comparison of (I - V) curves of Nb/Co(2 nm)/Py(7 nm)/Nb device with the control device Nb/Py(6 nm)/Nb at 4.2 K. We notice that the junction with only Py layer (6 nm), and no Co layer has a linear (I - V) curve, with a device resistance (R_N) value of ~ 118 m Ω . This suggests that the supercurrent carried by Nb/Co(2 nm)/Py(7 nm)/Nb device is not the standard singlet supercurrent, it is rather the long-range triplet supercurrent.

In the second control experiment, we decoupled Co and Py layers by depositing a layer of Cu in-between. In Fig. 6.9(b), we show a comparison of (I - V) curves of the Josephson junctions with magnetic barriers as Co(2 nm)/Py(11 nm) and Co(2 nm)/Cu(4 nm)/Py(11 nm). No signatures of any supercurrent were observed upon insertion of a Cu layer at the interface of Co and Py. Therefore, we conclude that the interfacial coupling of Co/Py bilayer is playing an important role in determining

the supercurrent through these junctions. This gives further confirmation of the fact that the magnetically non-collinear structure at Nb/Py interface is responsible for the generation of triplet supercurrents in S/XS/S Josephson junctions.

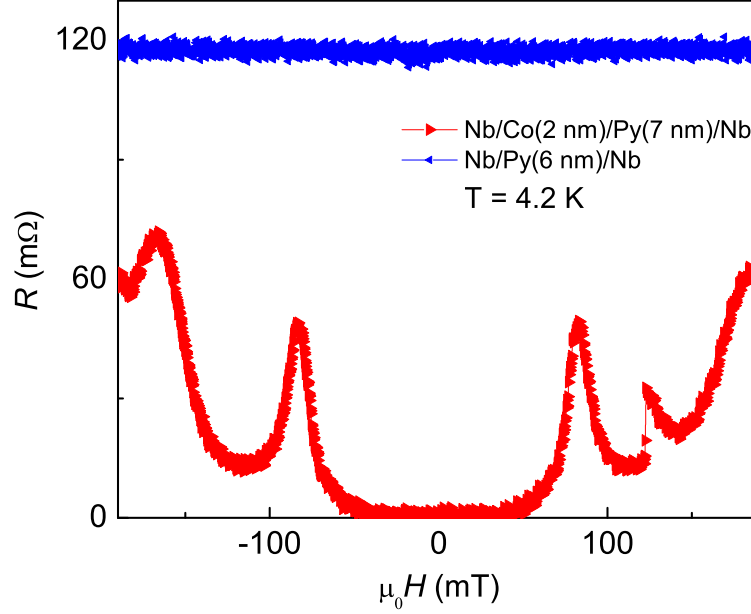


Figure 6.10: Comparison of $R(H)$ curves for Nb/Co(2 nm)/Py(7 nm)/Nb and Nb/Py(6 nm)/Nb Josephson junctions at 4.2 K. Fraunhofer type modulations were observed in junction resistance as a function of magnetic field for the Nb/Co(2 nm)/Py(7 nm)/Nb while no field dependence was observed for Nb/Py(6 nm)/Nb junction.

In addition to the above measurements, we performed resistance versus magnetic field measurements for Nb/Co(2 nm)/Py(7 nm)/Nb and Nb/Py(6 nm)/Nb devices at 4.2 K, as shown in Fig. 6.10. We note that no critical current was observed in Nb/Py(6 nm)/Nb junctions (with no Co layer). The Nb/Co(2 nm)/Py(7 nm)/Nb junction, on the other hand, showed modulations in R as a function of H .

In Fig. 6.11, we show the $I_c R_N$ product vs the thickness of Py layer, for a series of devices having different magnetic barriers such as Co/Py; Py/Co/Py; Py; Co/Cu/Py. Here, R_N is measured at bias currents higher than I_c , where $I(V)$ curve has a constant slope. The $I_c R_N$ data for a Py junction (without a Co layer) shown in gray color in Fig. 6.11 has been taken from Robinson *et al.* [42]. At first, we discuss the case of junctions with magnetic barrier as Co/Py XS,

where a tunable magnetic non-collinear structure of moments can be formed as a function of small magnetic fields (\sim mT). We observe that $I_c R_N$ product of the Co/Py junctions decay very slowly compared to the Py-only junctions. This shows that there should be an extra component of supercurrent in the XS junctions. From theoretical proposals [8,52,66], singlet Cooper pairs convert into triplet Cooper pairs, when they experience regions of non-collinear magnetization within their coherence length, ξ_S .

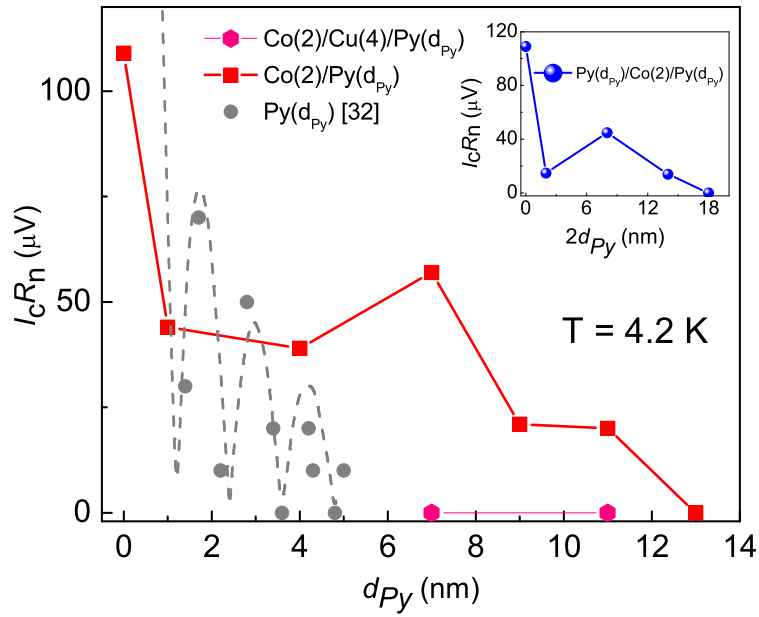


Figure 6.11: Variation of $I_c R_N$ product with Py thickness for all devices; the green curve presents the $I_c R_N$ for Py-only junction (taken from Ref. [42]). As d_{Py} increases above 5 nm, $I_c R_N$ is almost zero in these junctions, whereas on introducing an additional Co layer, the $I_c R_N$ product is enhanced and decays very slowly. Inset shows the $I_c R_N$ product for double spring Nb/Py/Co/Py/Nb junction with total thickness of the Py layer.

The source of magnetic non-collinearity in XS devices is the inhomogeneous structure of magnetic moments formed in the Py layer, due to the magnetic exchange coupling at the Co/Py interface, as seen from Fig. 6.1. Upon inserting a Cu layer between Co and Py, which magnetically isolates the Py and Co layers, we observe that the I_c of the Co/Cu/Py junction becomes zero, as shown in Fig. 6.11. This is a strong evidence in support of the fact that exchange-coupled Co/Py bilayer is

the key to the triplet supercurrent generation.

In the case of Co/Py junctions, the $I_c R_N$ product becomes zero for Py thickness higher than 11 nm, as shown in Fig. 6.11. In dirty limit, the decay length ξ_F of singlet Cooper pairs in F is given by, $\xi_F = \sqrt{\hbar D_F / E_{ex}}$ [39], where \hbar is the Planck's constant, D_F is the diffusion coefficient and E_{ex} is the exchange energy of the ferromagnet. According to previous reports [10,11], the triplet Cooper-pairs decay over a length scale given by the spin diffusion length, $L_F = \sqrt{D_F \tau_{sf}}$ which is $\sim 5 - 10$ nm in Py [13] and ~ 60 nm in Co [134]. This may explain the destruction of supercurrents beyond Py thickness of 11 nm.

Now, we compare the $I_c R_N$ product of Josephson junctions with asymmetric and symmetric Co/Py XS interfaces. In Py/Co/Py junctions, we have used the conventional S/F'/F/F'/S geometry proposed by Houzet and Buzdin [15]. We observe that the $I_c R_N$ product for symmetric and asymmetric Co/Py XS junctions decay very slowly compared to the Py junctions with no Co layer. We observed a finite supercurrent for total ferromagnetic thickness (Py(7 nm)/Co(2 nm)/Py(7 nm)) of 16 nm in symmetric Co/Py XS junctions as shown in the inset of Fig. 6.11.

Currently, it is well known that triplet supercurrents can be generated [9–11] in magnetic Josephson junctions, but its control in a single device is a subject of ongoing research [16,17,59]. In our devices, we have demonstrated manipulation of triplet supercurrents with the direction of a constant magnetic field with strong ferromagnets such as Co and Py.

6.4 Conclusion

We have investigated triplet supercurrents in nano-pillar Josephson junctions with symmetric and asymmetric Co/Py XS barriers. We observed supercurrents for Py layer thickness up to ~ 11 nm, which is very high compared to the singlet pair coherence length of Py ($\xi_{Py} \sim 1.4$ nm) [42] and comparable to the spin-diffusion

length in Py of $\sim 5-10$ nm [13,134]. We observed triplet supercurrents in asymmetric junctions, which was unexpected before. The decay length (~ 16 nm) of supercurrents was almost similar in both symmetric and asymmetric junctions. We performed control experiments to confirm the presence of triplet supercurrents. From control experiments, we conclude that the interfacial coupling of Co/Py bilayer is playing a vital role in the generation of triplet supercurrents. We have demonstrated a continuous control of triplet supercurrents with magnetic field orientation in both symmetric and asymmetric Josephson junctions.

Chapter 7

Summary and Future Scope

7.1 Summary

A summary of the important results of this thesis is presented in this concluding chapter. Generation and control of triplet correlations in superconductor(S)/ferromagnet(F) multilayers and S/F/S Josephson junctions using natural and synthetic domain walls (exchange-spring) have been the focus of this thesis. Generation of triplet correlations in Nb/Ni/Nb planar structures and triplet supercurrents in Nb/Ni/Nb Josephson junctions and SQUIDs have been demonstrated using natural domain walls. Tuning of Nb T_c in Nb/Co/Py/Nb multilayer and tuning of triplet supercurrents in Nb/Co/Py/Nb and Nb/Py/Co/Py/Nb nanopillar Josephson junctions have been demonstrated using exchange-spring (synthetic domain walls). Following a brief summary of the results, we conclude this chapter by identifying a few potential frontiers of further research on triplet supercurrents in S/F/S Josephson junctions.

7.1.1 Triplet correlations using natural domain walls

We have utilized the natural magnetic non-collinearity found in ferromagnets in the form of domain wall, for singlet-triplet conversion in Nb/Ni/Nb planar structures and Josephson junctions. Prior to these studies, we characterized the domain wall

configuration of Ni stripes using Kerr microscopy and studied the effect of these domain walls on an overlying Nb layer by plotting the $T_c(H)$ phase diagrams (in chapter 2). We found a suppression in T_c near coercive fields, where the effect of domain walls becomes maximum. In chapter 3, we utilized this stripe geometry to study singlet-triplet conversion through natural domain walls of Ni. For this purpose, a microscopic gap was carved in the Nb layer in a patterned Ni/Nb bilayer stripe. It is well known [85,106] that when a current passes through a ferromagnetic domain wall, it causes spin accumulation at the domain walls giving rise to domain wall magneto-resistance (DWMR). DWMR appears as an additional component in the MR curves, usually visible in constricted geometry. By carving a gap in the Nb layer, we were able to inject singlet Cooper pairs of Nb into the domain walls of Ni present underneath. We utilized DWMR as a tool to study the effect of this Cooper pair injection into domain walls. We compared DWMR at temperatures above and below the T_c of Nb in a Nb/Ni/Nb planar structure. Conventional DWMR peaks were observed at the coercive field for temperatures above T_c . Due to the presence of a gap in the Nb layer, we were able to measure the DWMR at temperatures below T_c . We observed an unconventional drop in DWMR near H_c for temperatures below T_c . We interpreted this unconventional drop in DWMR in terms of singlet-triplet conversion through the intrinsic domain walls of Ni. This observation was, however, an indirect evidence of singlet-triplet conversion via domain walls. We have extended this study further in chapter 4, looking for a direct signature.

In chapter 4, we used a constricted geometry to pin a single domain wall of Ni at the barrier of a focused ion beam (FIB) based Nb/Ni/Nb planar Josephson junction. A gap of width ~ 70 nm was carved using FIB in the Nb layer over the constriction in a Ni/Nb bilayer stripe. Micromagnetic 3D OOMMF simulations showed that a domain wall remains pinned at the notch for most part of the hysteresis loop. From the transport measurements, we found a supercurrent in these planar junctions. The long-range nature of the supercurrent was apparent from the

fact that supercurrent existed over a magnetic (Ni) barrier width of ~ 70 nm, which is much greater than the singlet pair coherence length (~ 4 nm) of Ni. We have also demonstrated a triplet SQUID using the same technique by putting two planar junctions in a superconductor loop. Characteristic voltage modulations were observed as a function of the magnetic flux, confirming a functional SQUID device. Therefore, we are able to fabricate a triplet Josephson junction SQUID through intrinsic domain walls for the first time.

7.1.2 Triplet correlations using synthetic domain walls

Control and tuning of triplet supercurrents is a major goal of superconducting-spintronics. In this context, an exchange-spring (XS) bilayer (a hard/soft ferromagnets combination), a reversible synthetic domain wall, can offer tuning of triplet supercurrents with small magnetic fields (few mT). We have explored this possibility by studying the $T_c(H)$ curves in S/XS/S multilayers and magnetic field angle dependent triplet supercurrents in S/XS/S magnetic Josephson junctions.

In chapter 5, we studied singlet-triplet conversion effects in S/XS/S multilayers by using diamagnetic screening currents as a probing tool. Nb/Co/Py/Nb multilayers were subjected to a static magnetic field in the plane of the multilayers to induce screening currents. In the $T_c(H)$ curve, we observed a relative enhancement in T_c in the spring range of the magnetic field, following an initial decrease due to the stray field effects. In the XS range, a magnetically non-collinear structure gets established in the Co/Py XS. Therefore, the recovery of T_c in spring samples was interpreted in terms of singlet-triplet conversion through the magnetic non-collinear structure of XS. We excluded the possibility of stray field cancellation as the possible reason for the observed recovery of T_c in these samples. We also demonstrated a tunable T_c with a reversible shift of ~ 400 mK in the spring range of magnetic fields. This reflects a reversible singlet-triplet conversion process due to the reversible nature of XS.

In Chapter 6, we used an XS (a reversible synthetic domain-wall) barrier to fabricate nano-pillar Josephson junctions to control triplet supercurrents. We fabricated FIB based Josephson junctions using Co/Py (XS) and Py/Co/Py (double XS) magnetic barriers. We observed Josephson coupling for Py layer thickness (11 nm) far exceeding the singlet-pair coherence length (~ 1.5 nm) of Py, confirming the existence of triplet supercurrents in these junctions. Magnetic-field-orientation-dependent control of spin-triplet supercurrents in a junction is demonstrated for the first time in this work. Triplet supercurrents were observed in Josephson junctions with both asymmetric (Co/Py) and symmetric (Py/Co/Py) XS interfaces, which was previously believed to be possible only with symmetric barriers. The complete summary of thesis is shown in Fig. 7.1.

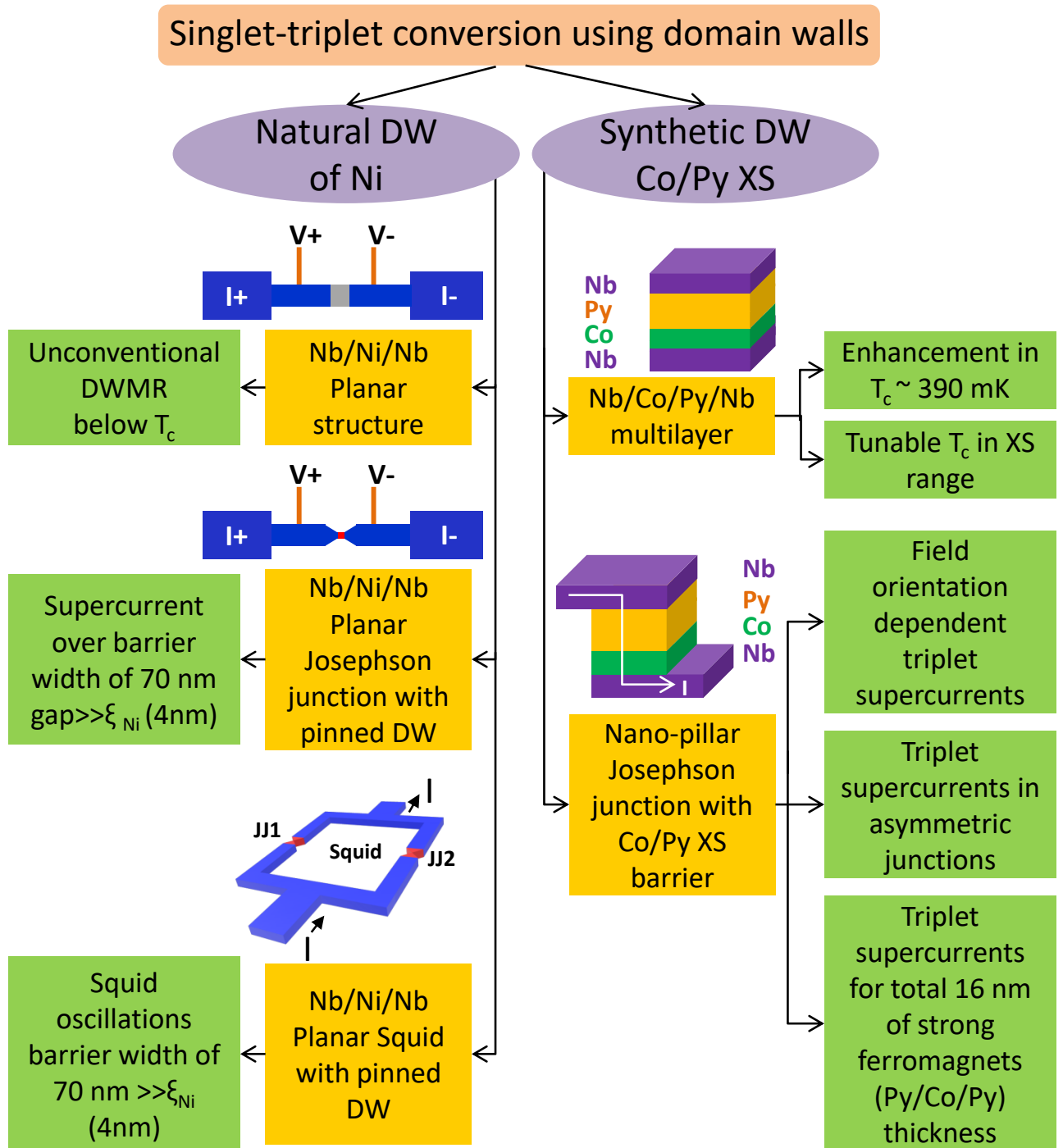


Figure 7.1: Pictorial summary of thesis.

7.2 Future Scope

In this thesis, we have been able to explore only a few aspects of the triplet supercurrents in S/F multilayers and S/F/S Josephson junctions. The work presented in this thesis is a small advance towards the generation and control of spin-triplet correlations in S/F multilayers and S/F/S Josephson junctions and may motivate many new experiments in the field of superconducting-spintronics.

There are certain aspects that can be looked at, in order to achieve more control over the generation and tuning of triplet supercurrents, following the work presented in this thesis:

- In chapter 4 of this thesis, we utilized a pinned Bloch domain wall to generate triplet supercurrents in Nb/Ni/Nb planar Josephson junctions. The natural extension of this work is to utilize Néel and Cross-tie domain walls to generate triplet supercurrents in S/F/S planar junctions. In this way, the influence of the structure of magnetic non-collinearity can be studied, which may be useful in superconducting spintronics.
- S/F/S planar junctions can be made with ferromagnets different from Ni, for example, Co and Py with spin diffusion length higher (~ 60 nm for Co) and lower (~ 5 nm for Py) than Ni (~ 20 nm). By doing so, one can investigate whether the decay length of triplet Cooper-pairs is limited by the spin-diffusion length of F or not, which is still an open question in front of researchers.
- In a planar S/F/S Josephson junction, spin-waves can be excited in the ferromagnet and the non-collinear spin structure of spin-wave can be exploited to couple the two superconducting electrodes by triplet supercurrents.
- Following chapter 3, a systematic study of DWMR for temperatures below T_c can be performed to investigate the singlet-triplet conversion process, in S/F/S planar structures.

- It has been predicted theoretically that a spin-triplet Josephson coupling can be established in S/F'/F/S Josephson junctions through a double Andreev reflection process, in which the current-phase relationship is dominated by a second harmonic term. In the Nb/Co/Py/Nb Josephson junction showed in chapter 6, one can study the Shapiro steps in I - V curves by irradiating the junction with microwave frequency to test this hypothesis.
- Other spring combinations with higher spin-diffusion length of soft and hard ferromagnetic materials can be used to make S/XS/S Josephson junction to obtain even higher range of triplet supercurrents.
- The range of triplet supercurrents in normal metals is unknown till date. This can be investigated by fabricating and characterizing Nb/Py/Co/Cu/Co/Py/Nb Josephson junctions. The range of triplet supercurrents in Cu can be obtained by varying the thickness of Cu to the point when supercurrent becomes zero.

List of Publications arising from the thesis

Journal

1. “Magnetic field tunable superconducting transition in Nb/Co/Py/Nb exchange-spring multilayers”, Ekta Bhatia, J. M. Devine Stoneman, Zoe H. Barber, Jason W.A. Robinson, and Kartik Senapati, *Appl. Phys. Lett.* (accepted).
2. “Domain wall induced modulation of low field H-T phase diagram in patterned superconductor-ferromagnet stripes”, Ekta Bhatia, Zoe H. Barber, Ilari J. Maasilta, and Kartik Senapati, *AIP Advances*, **2019**, 9, 045107.
3. “Shape critical domain reversal in patterned nickel and permalloy stripes in Neel and Bloch regime”, Ekta Bhatia, Zaine Hussain, V. Raghavendra Reddy, and Kartik Senapati, *arXiv:1903.08106* (Under review).
4. “Unconventional domain wall magnetoresistance of Nb-Ni-Nb planar structures below superconducting transition temperature of Nb”, Ekta Bhatia, Zaine Hussain, V. Raghavendra Reddy, Zoe H. Barber and Kartik Senapati, *arXiv:1904.09867* (Under review).
5. “Magnetic-field-orientation-dependent triplet supercurrents in Josephson junctions with symmetric and asymmetric exchange-spring interfaces”, Ekta Bhatia, J. M. Devine-Stoneman, Sachio Komori, Anand Srivastava, Zoe Barber, Kartik Senapati, and J. W. A. Robinson, *arXiv:1907.08406* (Under review).
6. “Intrinsic domain wall induced long range spin-triplet supercurrents in Nb-Ni-Nb planar Josephson junction and nano-SQUID”, Ekta Bhatia, Anand Srivastava, J. M. Devine-Stoneman, Zoe Barber, J. W. A. Robinson, Kartik Senapati, (Under review).

Thesis Highlight

Name of the Student: Ekta Bhatia

Name of the CI/OCC: NISER, Bhubaneswar

Enrolment No.: PHYS11201404003

Thesis Title: Natural and synthetic domain wall induced spin triplet correlations in superconducting multilayers and Josephson junctions

Discipline: Physical Sciences Sub-Area of Discipline: Experimental condensed matter physics

Date of viva voce: 11 March, 2020

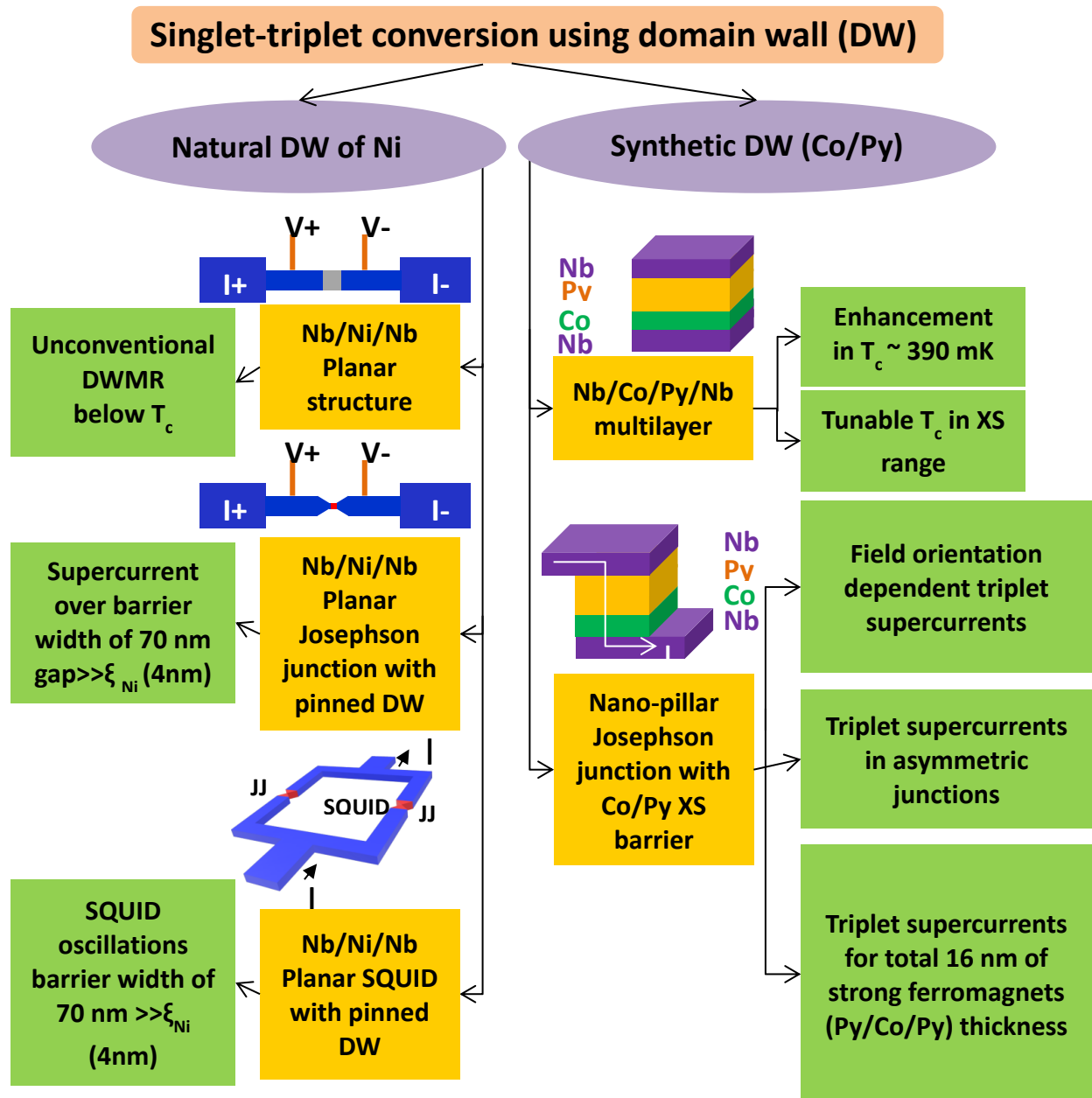


Figure 1: Pictorial summary of thesis

In this thesis, Generation and control of triplet correlations in superconductor(S)/ferromagnet(F) multilayers and S/F/S Josephson junctions using natural and synthetic domain walls (exchange-spring) have been demonstrated.